Centriole Remodeling Evolved into Centriole Degradation in Mouse Sperm

Sushil Khanal[1], Nahshon Puente[1], Rajanikanth Chandanayaka[2], Kebron Yeshitela Assefa[1], Mohamad Nawras[1], Katerina Turner[1], Ezekiel David Back[1], Abigail Royfman[1], James Burkett[3], Soon Hon Cheong[4], Heidi S. Fisher[5], Puneet Sindhwani[6], John Gray[1], Ramachandra Nallur Basappa[2], Tomer Avidor-Reiss[1,6,*]

[1] Department of Biological Sciences, University of Toledo, Toledo, OH, USA

[2] Department of Studies in Genetics and Genomics, University of Mysore, Manasagangotri, Mysuru, India

[3] Department of Neurosciences, College of Medicine and Life Sciences, University of Toledo, Toledo, OH, USA

[4] Department of Clinical Sciences, College of Veterinary Medicine, Cornell University, Ithaca, NY, USA

[5] Department of Biology, University of Maryland College Park, MD, USA

[6] Department of Urology, College of Medicine and Life Sciences, University of Toledo, Toledo, OH, USA

* Correspondence: Tomer.avidorreiss@utoledo.edu

Abstract

Centrioles are subcellular organelles with an evolutionarily conserved structure and a shock absorber-like function. In sperm, centrioles are found at the flagellum base and are essential for embryo development in basal animals. Yet, sperm centrioles have evolved diverse forms, sometimes acting like a transmission system, as in cattle, and sometimes becoming dispensable, as in house mice. How the essential sperm centriole evolved to become dispensable in some organisms is unclear. Here, we test the hypothesis that this transition occurred through a cascade of evolutionary changes to the proteins, structure, and function of sperm centrioles and was possibly driven by sperm competition. We found that the last steps in this cascade are associated with a change in the primary structure of the centriolar luminal protein FAM161A in rodents. This information provides the first insight into the molecular mechanisms and adaptive evolution underlying a major evolutionary transition within the internal structure of the mammalian sperm neck.

Running Title

Centriole remodeling evolved into centriole degradation

Keywords

Sperm, centriole, evolution, reproduction, fertility, miscarriage, FAM161A, dynamic basal complex, centrosome reduction, spermatogenesis, head-tail coupling apparatus (HTCA).

Graphical abstract

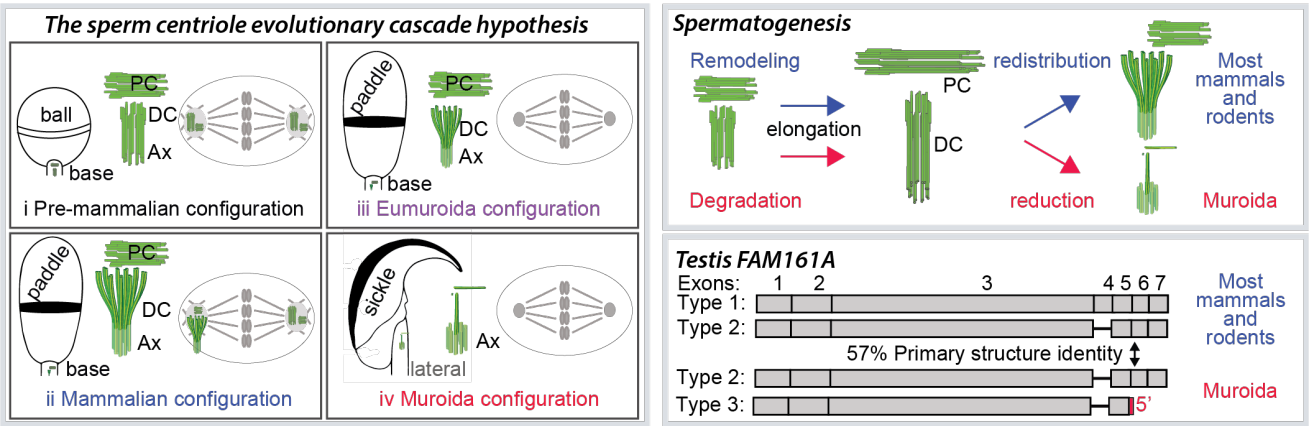

Highlights

- Barrel-shaped centrioles are present in all rodents except members of the Muridae taxonomical family.
- The FAM161A sequence evolved selectively in rodents and specifically in a murid subgroup.
- The evolution of centriole degradation is associated with the expression of a novel FAM161A isoform.
- The ancestral centriole remodeling program involves elongation followed by redistribution.
- The mouse centriole degradation program involves elongation followed by elimination.

Introduction

Centrioles are subcellular organelles with an evolutionarily conserved, barrel-shaped structure that are found at the base of cilia and flagella (reviewed in Azimzadeh, 2021; Winey and O'Toole, 2014). There, the centriole, also known as the basal body, acts as a shock absorber that resists the movement of axonemal microtubules relative to one other, although they may flex in response to ciliary forces (Junker et al., 2022). Yet, centrioles have evolved diverse structures in the sperm cells of many invertebrate and vertebrate animals, presumably due to divergent selective pressure produced by varying levels of sperm competition (reviewed in Avidor-Reiss and Fishman, 2019), an evolutionary process that drives sperm change due to post-ejaculatory competition between males (reviewed in Birkhead and Hunter, 1990; Humphries et al., 2008; Parker, 1970).

Most non-mammalian vertebrates, such as fish and Tetrapods (e.g., turtles, snakes, lizards, and birds) have two canonical, barrel-like centrioles in their spermatozoa that are essential post-fertilization (Ferreira and Dolder, 2003; Hao and Zhang, 2018; Hess et al., 1991; Jamieson, 2007; Yabe et al., 2007). Also, humans, cattle, and most other studied mammals have two spermatozoan centrioles, though only one of the centrioles (the proximal centriole) possesses a canonical structure. In these species, the other centriole–the distal centriole–has an atypical, fan-like structure and is part of a “transmission system” that connects the sperm tail to the head (Khanal et al., 2021). Both spermatozoan centrioles function post-fertilization to form the embryo’s first two centrosomes, which organize the zygotic microtubule cytoskeleton (Amargant et al., 2021; Kai et al., 2021; Sutovsky and Schatten, 2000; Uzbekov et al., 2023). In contrast, in the house mouse (*Mus musculus)*, spermatozoa lack any recognizable centrioles, centrioles are absent in the early embryo, and viable offspring can be produced by injecting a sperm head that lacks centrioles into an oocyte (Courtois et al., 2012; David et al., 2014; Gueth-Hallonet et al., 1993; Howe and FitzHarris, 2013; Kuretake et al., 1996; Manandhar et al., 1999; Manandhar et al., 1998; Pomp et al., 2022; Yamauchi et al., 2002; Yan et al., 2008). How the centriole, an essential spermatozoan structure in most animals, became modified and, ultimately, dispensable in house mouse evolution is an enigma.

One possible explanation is provided by the evolutionary sex cascade theory, which claims that sexual selection modifies gametes as logical consequences whenever certain successive conditions are met, forming a causality-connected events sequence (Parker, 2014). This cascade is driven largely by post-ejaculatory selection, which includes sperm competition and cryptic female choice, to produce spermatozoa with varying centriole numbers, morphologies, and behaviors (Humphries et al., 2008; Lüpold et al., 2020). The evolutionary sex cascade theory has, up to now, applied mainly to mechanisms causing change in general gamete and gonad properties, such as anisogamy (gametes of different sizes) (Mokos et al., 2021), sex ratio (Schill et al., 2010), and testis size (Rowley et al., 2019). Though there have been some attempts to connect sexual selection to the size of spermatozoa or the spermatozoan tail (Fisher et al., 2016; Gomendio and Roldan, 1991; Joly et al., 2004; Kahrl et al., 2021), how sexual selection applies in terms of major evolutionary transitions to an internal gamete structure, such as the centriole, remains less explored.

Synthesis of the literature on gametes and embryonic centrioles suggests a hypothetical, big stroke, four-stage, centriolar evolutionary cascade that has impacted the spermatozoa and embryo in mammals (**Figure 1A**).

Stage 1 – *The pre-mammalian centriolar configuration*: spermatozoa include a canonical proximal centriole and a canonical distal centriole, representing the ancestral animal configuration. At this stage, the two centrioles are required for early embryogenesis (zygote to blastocyst), exhibiting centriole-dependent embryonic development (Yabe et al., 2007).

Stage 2 – *The mammalian centriolar configuration*: sperm competition within the female reproductive tract of internal fertilizers selected for sperm with atypical centrioles, suggesting that atypical centrioles are an innovation associated with changes in the mode of fertilization (Fishman et al., 2017; Khire et al., 2016; Turner et al., 2022), as internal fertilization provides unique challenges to the sperm. For example, in mammals, sperm swim in a multi-compartmentalized female reproductive tract with varying viscoelastic mucus and complex landscapes, including microgrooves (reviewed inTung and Suarez, 2021). Therefore, in mammals, atypical centrioles produced spermatozoa with a dynamic basal complex (DBC), an advantage that help sperm to navigate the complex female reproductive tract (Fishman et al., 2018; Khanal et al., 2021). At this evolutionary stage, centriole-dependent embryonic development is maintained. However, the atypical distal centriole comes with the costs of increased miscarriage rates and reduced fecundity (Cavazza et al., 2021).

Stage 3 – *The Eumuroida* (a murid subgroup that includes Muridae and Cricetidae) *centriolar configuration*: the miscarriage cost, which resulted in reduced offspring production, acted as a selective pressure in the ancestor of house mice, an r-strategy species that maximizes reproductive capacity (Shin et al., 1998). Consequently, centriole-independent embryonic development evolved in the mouse ancestor (Bangs et al., 2015; Calarco, 2000; Clift and Schuh, 2015; Coelho et al., 2013; Fawcett, 1975; Gueth-Hallonet et al., 1993; Manandhar et al., 1999; Schatten et al., 1985; Schatten et al., 1986; Simerly et al., 1993; Woolley and Fawcett, 1973). Centriole-independent embryonic development is mediated by an egg-derived mechanism involving maternal cytoplasmic centrosomes and post-cytokinetic microtubule bridges (Coelho et al., 2013; Jin et al., 2012; Zenker et al., 2017) (reviewed in Fishman et al., 2021; Palacios Martinez et al., 2022).

Stage 4 – *The Muridae centriolar configuration*: Because embryonic development became centriole-independent, spermatozoan centrioles were freed from the functional constraints imposed by their role in the embryo. This freedom allowed the proximal and distal centriolar structures to be further modified, leaving only their remnants in spermatozoa (i.e., “degraded” or “degenerated” (Leung et al., 2021; Manandhar et al., 1998)) and enhancing spermatozoan competitiveness. In mice, this led to the evolution of a new type of sperm neck attachment at the side of the nucleus, rather than at the base, as in most other animals.

General aspects of this sperm centriole evolutionary cascade hypothesis are supported by morphological and ultrastructural studies in the sperm, egg, and zygote; however, it is unclear how these changes occurred at the molecular level (Bangs et al., 2015; Calarco, 2000; Clift and Schuh, 2015; Coelho et al., 2013; Fawcett, 1975; Gueth-Hallonet et al., 1993; Manandhar et al., 1999; Schatten et al., 1985; Schatten et al., 1986; Simerly et al., 1993; Woolley and Fawcett, 1973).

The canonical structure and function of centrioles are essential throughout mammalian development and physiology to form the cells’ cilia (Reviewed in Breslow and Holland, 2019). Centrioles serve as both the seed and template for cilia, and therefore, their precise structure is critical for their function (Breslow and Holland, 2019; Greenan et al., 2018). Considering this major constraint on centriolar structure, it is surprising that spermatozoan centrioles are so structurally diverse. Conservation on one hand and diversity on the other produces genetic conflict and requires genomic plasticity, which should have a molecular signature of positive selection. Such plasticity should accrue in some centriolar proteins and should be accompanied by gene duplication (Finseth et al., 2015; Henikoff et al., 2001; Henikoff et al., 2017; Ross et al., 2013), though how a remodeled sperm centriole is produced through centriolar plasticity is unclear.

One sub-cellular mechanism that contributes to sperm centriolar plasticity is the timing of their remodeling. Sperm centrioles are remodeled only after they form flagella (i.e., the sperm tail) in a process referred to as centrosome reduction (Manandhar et al., 1998). In most mammals, centrosome reduction produces atypical centrioles and is therefore referred to as centriole remodeling in these species (Fishman et al., 2018); in mice, centrosome reduction eliminates the two sperm centrioles and is referred to as centriole degeneration or degradation (Manandhar et al., 1999). Because centriole remodeling occurs in many mammalian orders, it is presumed to be the ancestral mammalian process, though how centriole remodeling evolved into centriole degradation is unknown.

The rigid, barrel-shaped structure of canonical centrioles is maintained by a luminal scaffold comprised of the proteins CETN1, POC5, POC1B, and FAM161A (Le Guennec et al., 2020; Steib et al., 2020). Interestingly, the sperm of many mammalian species–including humans, rabbits, and bovines–have evolved

a fan-shaped distal centriole, in which the luminal scaffold proteins are redistributed into two rod-like structures (Fishman et al., 2018). These rods, along with other surrounding structures (i.e., segmented columns and the proximal centriole), move relative to each other during tail beating, forming a dynamic basal complex, which mechanically couples the sperm head and tail (Khanal et al., 2021). The fate of luminal scaffold proteins in murid spermatozoa is unknown.

Here, we studied rodent sperm centrioles and found that only after centriole-independent embryonic development evolved in the ancestor of families Cricetidae and Muridae did sperm centrioles degenerate in association with the novel, lateral, head-neck attachment in the spermatozoa of Muridae species. We found that the primary structure and isoform expression of the luminal scaffold protein FAM161A gradually evolved in the lineage leading to mice. The first changes to FAM161A were associated with sperm centrioles becoming dispensable post-fertilization in the ancestor of families Cricetidae and Muridae, although the centrioles maintained their ancestral mammalian structure. Later, further changes to FAM161A were associated with the appearance of novel head-neck morphology and sperm centriole degeneration. Structural changes to FAM161A resulted in distinct functions *in vitro* and unique localization *in vivo*. Finally, although Muridae spermatozoa have no recognizable centrioles, centriolar proteins are present in their sperm neck, suggesting that highly modified remnant centrioles are present. Altogether, our study provides the first molecular insight into the evolutionary process that changed the centriole remodeling program occurring in most mammals into the centriole degeneration program that occurs in some rodents.

Results

1. Proximal centriole loss and lateral head-neck attachment associatively evolved in the Muridae ancestor

The fan-shaped, atypical distal centriole was discovered in 2018 using advanced electron microscopy (Fishman et al., 2018); therefore, studies of spermatozoa prior to this year mainly addressed the presence or lack of barrel-shaped centrioles. Two barrel-shaped proximal and distal centrioles are found in the spermatozoa of most basal vertebrate external fertilizers (Turner et al., 2022). In contrast, classic transmission electron microscopy (TEM) studies in mammalian spermatozoa found only one barrel-shaped centriole, the proximal centriole, with a few exceptions in marsupial and some rodent species that appear to lack it (**Sfig 1**). Because rodent spermatozoan ultrastructure has undergone extensive phylogenetic study, and because the stereotypical proximal centriolar structure enables detection of evolutionary changes, we used rodent proximal centriolar ultrastructure to track the evolutionary changes leading to their disappearance. To this end, we systematically surveyed past TEM studies of rodent spermatozoan centrioles (**Fig 1B**).

The precise phylogeny of proximal centriole loss is unknown. In general, the literature on rodent sperm centrioles is confusing and at many times appears to claim that rodent spermatozoa lack a proximal centriole. For example, Mandahar and colleagues wrote that “rodent spermatozoa totally lack centrioles” (p. 256, Manandhar et al., 2000). Similarly, Xu and colleagues, wrote that “spermatozoa of several species (e.g., rodents) lack centrioles due to complete centriolar degeneration” (p. 201, Xu et al., 2008). However, when we surveyed the original literature on rodent spermatozoan ultrastructure, we found that a proximal centriole was reported to be present in most rodents and in all three of the main rodent suborders. A proximal centriole is present in all studied rodent species of **suborder Hystricomorpha**, which includes the guinea pig (*Cavia porcellus*) (Woolley et al., 2008), chinchilla (*Chinchilla lanigera*) (Healey and Weir, 1970), cane rat (*Thryonomys swinderianus*) (Adebayo et al., 2019), agouti (*Dasyprocta aguti*) (Arroyo et al., 2017), Spix’s yellow-toothed cavy (*Galea spixii*), and naked mole rat (*Heterocephalus glaber*) (Van Der Horst et al., 2011). A proximal centriole is also reported in the rodent species of **suborder Sciuromorpha**, which includes the Korean squirrel (*Tamias sibiricus*) (Lee and Park, 2011) and the flying squirrel (*Glaucomys volans*) (Hruban et al., 1971). Finally, a proximal centriole is reported in three studied species of family Cricetidae of **suborder Myomorpha**: the golden hamster (*Mesocricetus auratus*) (Franklin et al., 1970), Chinese hamster (*Cricetulus griseus*) (Yanagimachi et al., 1983), and Winkelmann's mouse (*Peromyscus winkelmamzi*) (Garcia Lorenzana et al., 1998). The presence of a proximal centriole in the three main rodent suborders suggests that a canonical proximal centriole was present in the last common rodent ancestor and is present in many existing rodent species.

186 In contrast, a proximal centriole is reported to be absent in the five studied members of family Muridae of
187 **suborder Myomorpha**, which includes the house mouse (*Mus musculus*), rat (*Rattus norvegicus*),
188 Mongolian gerbil (*Meriones unguiculatus*), and two *Apodemus* species (*Apodemus agrarius coreae* and
189 *Apodemus speciosus peninsulae*) (Chakraborty, 1979; Lee and Mori, 2006; Manandhar et al., 1998; Woolley
190 and Fawcett, 1973). The location of the missing proximal centriole in the spermatozoan neck of these
191 species is marked by an empty, vault-like space, suggesting that a proximal centriole remnant may be
192 present. Indeed, a recent study using state-of-the-art cryo-electron microscopy in house mouse
193 spermatozoa confirmed that there were some microtubule remnants where the proximal centriole should be
194 located (Leung et al., 2021). The absence of a proximal centriole in multiple genera of family Muridae
195 contrasted with its presence in multiple genera of the family Cricetidae suggests that proximal centriole
196 degeneration occurred after the divergence of Muridae from Cricetidae, which happened about 20 million
197 years ago (Steppan and Schenk, 2017).

198 *Proximal centriole loss correlates with lateral tail attachment to the head in the Muridae ancestor*

199 The observation that a barrel-shaped proximal centriole is present in Cricetidae despite its dispensability
200 post-fertilization suggests that the proximal centriole has a function in the cricetid spermatozoon. Similarly,
201 the observed absence of a barrel-shaped proximal centriole in Muridae, despite its presence in Cricetidae,
202 suggests that the proximal centriole became dispensable in the murid spermatozoon. Since the sperm
203 centriole connects the tail to the head as part of the head-tail connecting apparatus (HTCA) (Li et al., 2022)
204 and can coordinate sperm tail and head movement (Khanal et al., 2021), we considered the structure of the
205 proximal centriole in the context of its function in sperm neck and head morphology. Mammalian
206 spermatozoa possess the same basic structural components (head, neck, and tail) but can vary in their
207 morphology, size, and, particularly, in their head shape and the location of the head-neck junction.

208 Most Eutherian mammals and, specifically, rodents of suborders Hystricomorpha and Sciuromora have a
209 short, oval- or paddle-shaped sperm head with a sperm neck that is attached at or near the center of the
210 head (referred to as a centrally inserted neck) (Temple-Smith et al., 2018) (**Fig 1**). As a result, it is thought
211 that the last common rodent ancestor had a paddle-shaped head with a centrally inserted neck (Breed et
212 al., 2014; Hamasaki et al., 1994). Rodent species of suborders Hystricomorpha and also have a proximal
213 centriole, suggesting these three characteristics are associated with each other (**Fig 1C**).

214 While several groups of Myomorpha have the ancestral, paddle-shaped head and centrally inserted neck
215 (the tail attached to the center of the head base and is situated below the head base), some have evolved
216 a unique sperm head shape and head-neck attachment point (Breed et al., 2014; Varea Sanchez et al.,
217 2013). For example, the last ancestor of Cricetidae and Muridae is thought to have evolved a novel,
218 elongated, sickle-shaped head (Breed et al., 2014) (**Fig 1D**). Many species of family Cricetidae have a
219 centrally inserted or off-center head-neck attachment (the tail attached asymmetrically to the head base and
220 is situated below the head base) (Breed et al., 2014; Hamasaki et al., 1994) and a proximal centriole,
221 suggesting that their proximal centriole was maintained after the appearance of a sickle-shaped head
222 (Franklin et al., 1970; Garcia Lorenzana et al., 1998; Yanagimachi et al., 1983). Therefore, in these cricetids,
223 the two characteristics that are associated with each other are the presence of a proximal centriole and a
224 centrally inserted neck.

225 As discussed above, the proximal centriole is absent in family Muridae, the species of which exhibit, in
226 addition to a sickle-shaped head, a unique, lateral head-neck attachment (the tail attached to the head side
227 and situated in parallel to the head base) (**Fig 1D–E**). The difference between the head-neck attachment in
228 Cricetidae and Muridae species suggests that, in rodents, a proximal centriole is present when the neck is
229 centrally inserted (the ancestral form) or off-center and that a proximal centriole is absent when the neck is
230 laterally attached to the head (the derived form), as in Muridae. Therefore, we hypothesize that centrioles
231 are structurally degenerated as part of the evolution of the lateral head-neck attachment in Muridae.

232 **2. The primary structure of FAM161A evolved in Muridae and Cricetidae**

233 The spermatozoa of some rodent clades have evolved to successfully fertilize without centrioles. The
234 molecular basis underlying this evolutionary change is unknown, but we hypothesized that it is associated
235 with a change in centrosomal protein structure and function. To identify candidate proteins, we searched for
236 sperm centrosomal proteins that diverge specifically in house mice in contrast to other mammals. We
237 identified sperm centrosomal proteins by comparing the spermatozoon proteome (Amaral et al., 2013; Baker

et al., 2013; Baker et al., 2007; Wang et al., 2013) to the centrosomal protein database (Alves-Cruzeiro et al., 2014). We performed a rapid and simple protein sequence (i.e., primary structure) comparison between human and bovine, which have two spermatozoan centrioles, and house mice, which lack spermatozoan centrioles; we refer to this calculation as the Identity Ratio (**Fig 2A**). A ratio of 1.00 indicates that the human and house mouse orthologs have a percent amino acid identity equal to the ratio between human and bovine, a ratio of more than 1.00 indicates that the human and house mouse orthologs have a greater percent primary structure identity than the ratio between human and bovine, and a ratio of less than 1.00 indicates that the human and house mouse orthologs have a lower percent primary structure identity than the ratio between human and bovine. According to simple phylogenetic considerations (**Fig 2B**), we would expect humans to be more identical to house mice than to bovine and, consequently, that their proteins should have an Identity Ratio greater than 1.00.

We found that 450 putative sperm centrosomal proteins have an Identity Ratio range between 0.63 and 1.90, with most centrosomal proteins having an Identity Ratio below 1.00 (**STable 2-1**). Most significantly, FAM161A, a known component of the sperm atypical centriole that exhibits species-specific labeling differences (Khanal et al., 2021), had the third lowest Identity Ratio (0.74) in this list, suggesting that FAM161A has extensively evolved in house mice. To be more stringent in quantifying the level of specific change in house mouse protein sequences, we calculated an Extended Identity Ratio (EIR), which compares the three sequence identity values between house mice and either of three species (humans, bovines, or rabbits) that have two spermatozoan centrioles to the three sequence identity values between the same species (humans, bovines, and rabbits) (**Fig 2A**). Using this quantification, we found an EIR of 0.77 for FAM161A, further supporting its potential role in sperm centriole evolution.

Reproductive genes evolve faster than other genes due to adaptive diversification associated with sperm competition, cryptic female choice, and sexual conflict (Clark et al., 2006; reviewed in Swanson and Vacquier, 2002). In contrast, genes integral to sperm function evolve faster in monogamous species than in promiscuous species, possibly because of reduced selective constraint (Gozashti et al., 2021). Because house mice exhibit a high level of gene sequence diversification (Thybert et al., 2018), the above evolutionary factors may result in a shift in the EIR of FAM161A to below 1.00. Therefore, we tested whether other contributory evolutionary trends drive the low EIR of FAM161A. In mammals, FAM161A has a paralog, FAM161B, which has a higher EIR (EIR = 1.04). Proteins whose genes flank the *Fam161a* gene in house mouse chromosome 11 have higher EIR (EIR = 0.84–1.02) (**Fig 2D**). These values suggest that the *Fam161a* gene evolved without haplotype selection and is an evolutionary hotspot. Finally, sperm proteins known to have divergent sequences had higher EIR (EIR = 0.88–1.00) (**Fig 2E**) (Luke et al., 2016). Altogether, these comparatively higher EIR values suggest that the FAM161A sequence selectively evolved in house mice.

FAM161A belongs to a small set of centriolar luminal proteins that form a unique rod structure in the atypical distal centriole. Yet, the set's other proteins, such as POC1B and POC5, have higher EIR (EIR = 0.91–1.01) than FAM161A (**Fig 2C**). Similar results were observed by calculating dN/dS ratio (ω). In this analysis, $\omega > 1$ indicates positive (adaptive, diversifying, increasing amino-acid diversity) selection, $\omega = 1$ indicates neutral evolution, and $\omega < 1$ indicates negative (purifying, the selective removal of deleterious mutations) selection. The median of mammalian protein ω values falls between 0.08 and 0.10, depending on the species being compared (Toll-Riera et al., 2011). We expected that most centriolar rod proteins would be under purifying selection because centrioles are essential in animal development and physiology (Bazzi and Anderson, 2014; David et al., 2014). Indeed, we found that ω of rodent POC1B and POC5 are close to the mammalian median (ω = 0.19–0.27) (**STable 2-2**). In contrast, FAM161A has a much higher ω of 0.58, suggesting that the FAM161A sequence is evolving more quickly than other distal centriolar proteins. Consistent with our previous EIR analysis, the ω value of FAM161A is higher in Muridae than in Cricetidae and other Myomorpha species (0.63 > 0.57 > 0.49, respectively), supporting our conclusion that it is rapidly evolving.

To understand the evolution of FAM161A in mammals, we analyzed the FAM161A primary structure identity of humans to other species that have a predicted proteome in the National Center for Biotechnology Information (NCBI) protein database (**Fig 2F–G**). Human FAM161A has a 70–77% primary structure identity to bovines and rabbits. A similar primary structure identity to human FAM161A is found in species from suborder Sciuromorpha (76±0.6), suborder Hystricomorpha (71±3), and the non-Muridae-Cricetidae clades of suborder Myomorpha (69±4). This primary structure identity suggests that basal rodents with centriole-dependent embryonic development, a proximal centriole, and centrally inserted neck have similar FAM161A

292 rates of evolution. In contrast, in the Muridae-Cricetidae clades, FAM161A shows a lower primary structure
293 identity to human FAM161A, at 60±0.2 in Cricetidae species and 57±2 in Muridae species. This statistically
294 significant difference suggests that the FAM161A primary structure started evolving in the Muridae and
295 Cricetidae ancestor (which had lateral head-neck attachment) and accelerated in the Muridae lineage
296 (species of which have centriole-independent embryonic development in common). Considering the other
297 sperm changes (**Fig 1**), these findings are consistent with the hypothesis that house mouse FAM161A
298 underwent a distinctive primary structural change that correlates with the emergence of centriole-
299 independent embryo development, lateral head-neck attachment, and proximal centriole loss.

300 Next, we generated a FAM161A phylogenetic tree of 115 mammals using MrBayes and IQtree (maximum-
301 likelihood and Bayesian phylogenetic trees) (**Fig 2H**) and found that the tree has eight main branches. Three
302 large, related branches of non-rodent mammals included primates, carnivora, and ungulates, and exhibited
303 relatively high FAM161A primary structural similarity (branches 1–3 in **Fig 2H**). The remaining five branches
304 were comprised of rodent species (branches 4–8 in **Fig 2H**). One basal rodent branch included Muridae and
305 Cricetidae species and was the most diverse group, as expected from accelerated adaptive evolution
306 (branch 8 in **Fig 2H**). The remaining four rodent branches were intermediate between non-rodent mammals
307 and Muridae and Cricetidae species (branches 4–7 in **Fig 2H**). Four different methods (Mixed Effects Model
308 of Evolution, MEME; Fixed Effects Likelihood, FEL; Phylogenetic Analysis by Maximum Likelihood, PMAL;
309 and Fast Unconstrained Bayesian AppRoximation, FUBAR) identified many more sites that have undergone
310 adaptive evolution in rodents than in primates, carnivora, and ungulates (**STable 2-3**). For example, PMAL
311 and FUBAR identified greater than three-fold more positively and negatively selected sites in rodents than
312 in primates, carnivora, and ungulates.

313 Furthermore, we searched for the rodent subgroup that drives accelerated adaptive evolution in rodents.
314 We generated a FAM161A molecular tree in rodents using FEL (**Fig 2I**) and found that the tree has three
315 main branches, which corresponded to Muridae, Cricetidae, and other Myomorpha species. FEL found a
316 similar number of positively selected sites in the three groups (14, 14, and 15 sites, respectively, $P<0.05$)
317 but a much smaller number of negatively selected sites in Muridae than in Cricetidae and other Myomorpha
318 species (4, 87, and 48, respectively) (**STable 2-4**). This finding is consistent with a weaker selective constraint
319 on FAM161A primary structure in Muridae.

320 ### 3. Muridae testes express a novel FAM161A protein and mRNA isoform

321 Mammalian FAM161A has multiple predicted isoforms in the NCBI protein database. Isoforms of two
322 different lengths were studied in humans and house mice (Bandah-Rozenfeld et al., 2010; Langmann et al.,
323 2010; Zach and Stohr, 2014) (**Fig 3A**). Here, we refer to the long isoform, comprised of exons 1–7 and
324 expressed in photoreceptors, as type 1 (house mouse 80 KDa, 700 aa, XP_006514891; human 83 KDa,
325 716 aa, NP_001188472). We refer to the shorter isoform, comprised of exons 1–3 and 5–7 and expressed
326 ubiquitously, as type 2 (house mouse 74 KDa, 644 aa, XP_006514893; human 76 KDa, 660 aa,
327 NP_001188472).

328 We studied FAM161A in tissue samples by western blot analysis. As expected, house mouse and rat eyes
329 express a ~80 KDa protein, corresponding to the FAM161A type 1 isoform (**Fig 3B**). Also, expectedly, we
330 observed a single FAM161A isoform of molecular size just above ~72 KDa, probably corresponding to
331 FAM161A type 2, in human and house mouse cells (i.e., U2OS and 3T3) (**Fig 3C**). Similarly, in bovine and
332 human testes, we found a single isoform just above ~72 KDa, expected to be FAM161A type 2 (**Fig 3D**).
333 These observations confirm expectations based on published literature (Downs and Mellersh, 2014).

334 Interestingly, in murids (e.g., house mice and rats), two FAM161A isoforms are expressed in their testes:
335 one at ~72 KDa, which may correspond to house mouse type 2, and one shorter isoform below the 72 KDa
336 marker, at ~60 KDa, which we refer to as the type 3 isoform (**Fig 3E**). Analysis of house mouse spermatid
337 mRNA shotgun sequencing data predicted that house mouse testes express four transcripts: a most
338 common transcript, NP_001350211, coding for a 555-aa isoform, and an additional three minor transcripts,
339 including XP_006514893, the type 2, 644-aa isoform (**SFig 3-1A**) (Green et al., 2018). The new 555-aa
340 isoform has a predicted molecular weight of 64 KDa and is expected to be the type 3 isoform. It contains
341 exons 1, 2, 3, 5, and the beginning of intron 5, which codes for five new amino acids, VVFIGX, followed by
342 a unique, 3' untranslated sequence (**Fig 3A**). We refer to this unique exon 5 as exon 5'. Using 5´ RACE,
343 PCR amplification, and sequencing, we confirmed that the type 3 and type 2 isoforms are expressed in
344 house mouse testes (**SFig 3-1B–C**). The type 3 isoform was further confirmed by a search of the NCBI

house mouse EST database, which found seven FAM161A transcripts with the unique type 3 C-terminus sequence in house mouse testes (**SFig 3-1D**).

4. The FAM161A type 3 isoform exhibits a relatively high level of positively selected sites

The differential expression of FAM161A isoforms may have resulted in a distinctive rate of evolutionary change. The longest isoform of FAM161A (type 1) has seven exons (700 aa in house mice): Exons 1,2, 3, and 5 (575 aa, or 82.1% of the protein) are found in all isoforms, whereas exons 4, 6, and 7 (125 aa, or 17.9% of the protein) are found only in non-type 3 isoforms. To identify which of these exons are under selection, we employed MEME to identify the sites that are under episodic diversifying selection across the four major mammalian groups (**Fig 2J**).

We found that exons 4, 6, and 7 have 17 negatively selected sites out of 125 aa, a rate of 13.6.%. Similarly, exons 1, 2, 3, and 5 have 84 negative sites out of 575 aa, a rate of 14.6 %. These similar rates suggest a similar level of purifying selection in the type 1, 2, and 3 isoforms. In contrast, exons 4, 6, and 7 have only 1 positively selected site out of 125, a rate of 0.8%, whereas exons 1, 2, 3, and 5 have 38 positively selected sites out of 575 aa, a rate of 6.6%. This difference in rates is statistically significant, based on the Z Score Calculator for 2 Population Proportions (P = 0.01). The observation that relatively more positive selection occurs in the exons shared between types 1, 2, and 3 than in the exons not expressed in type 3 suggests that the type 3 isoform evolved faster than the other isoforms.

We predicted the house mouse FAM161A structure using AlphaFold and found that the positively selected sites are mostly concentrated in one section of the protein, which we refer to as the core domain (**Fig 3H**). *Mus* and *Rattus* species have few positively (17 and 18, respectively) and negatively (1 and 0, respectively) selected sites as identified by FEL, suggesting that FAM161A changes are fixed and stable in these genera.

5. FAM161A has distinct functions in house mouse and human sperm

Human FAM161A type 1 interacts with human POC5 and POC1B (Le Guennec et al., 2020), which also interact with each other (Le Guennec et al., 2020). Human POC5 also interacts with human CETN protein family members (Azimzadeh et al., 2009). Of these four proteins, only FAM161A interacts directly with microtubules (via amino acids 230–543 of type 2, domain UPF0564) (**SFig 4-1A**) (Zach et al., 2012). Using the FAM161A-microtubule interaction, we mapped binding between human FAM161A type 2 and the other three human rod proteins through their recruitment to the cellular microtubule network when co-expressed with FAM161A (**SFig 4-1B–F).** We supplemented our protein interaction with yeast two hybrid assays and found that amino acids 1–141 of human FAM161A type 2 interact with POC1B (**SFig 4-1D**), amino acids 141–230 of human FAM161A type 2 interact with human POC5 (**SFig 4-1C & 1D**), and amino acids 1–222 of the human POC5 N-terminus interact with POC1B C-terminus amino acids 365–478 (**SFig 4-1E**). *These findings suggest a web of interactions between centriolar luminal scaffold/rod proteins* (**SFig 4-1F**).

Interestingly, the interacting domains of FAM161A include most of the positively selected sites in rodents (**Fig 3J**). To test for potential functional differences due to divergent primary structure, we expressed house mouse and human FAM161A type 2 in U2OS cells (**Fig 4**). As expected, we found that both proteins localize to the microtubules (**Fig 4A**), though they exhibited differences in their localization patterns and the extent of microtubule co-localization. We have distinguished four types of localization pattern: “cytoplasmic,” with linear FAM161A throughout the cytoplasm; “intranuclear,” with FAM161A foci in the nucleus; “perinuclear” (circular), with FAM161A around the nucleus; and “mix-nuclear”, characterized by both intranuclear and perinuclear patterns (**Fig 4A**). Human FAM161A type 2 mostly localized to the cytoplasmic microtubules. In contrast, house mouse FAM161A type 2 showed a mostly intranuclear or mix-nuclear pattern (**Fig 4A–B**). These distinct localization patterns suggest that the amino acid differences between house mouse and human FAM161A type 2 produce functional differences.

FAM161A type 3 is a protein 555 amino acids in length, composed of the homologous sequences that mediate binding to microtubules (type 3 amino acids 226–532, domain UPF0564), POC1B (type 3 amino acids 1–139), and POC5 (type 3 amino acids 140–226); however, it is missing the 95 amino acids encoded by type 2 exons 5 and 6, which have unknown function (**SFig 4-2**). In contrast to type 2, type 3 mostly formed foci in the nucleus (**Fig 4A–B**). This localization pattern indicates that the protein domain differences between house mouse FAM161A types 2 and 3 produce functional differences.

Human FAM161A type 2 forms homodimers via amino acids 230–386 (Zach et al., 2012). This amino acid sequence corresponds to amino acids 226–380 of house mouse types 2 and 3, suggesting that they can also dimerize. To gain insight into the effect of house mouse type 2 and type 3 on each other, we co-expressed them. We found that type 3 prevents type 2 from colocalizing with the circular microtubules (perinuclear pattern) and, instead, targets type 2 to foci in the nucleus (intranuclear pattern) (**Fig 4A–C**). This observation suggests that FAM161A type 3 can act as a dominant negative isoform that prevents FAM161A type 2 from localizing to the cytoplasmic microtubules.

Human FAM161A type 2 interacts with POC1B and recruits it to cytoplasmic microtubules (Roosing et al., 2014). Therefore, we next examined the interaction of house mouse FAM161A with mCherry-POC1B. POC1B aggregates are commonly observed when rod proteins (i.e., POC1B, POC5, and Centrin) are expressed in U2OS cells (without expressing FAM161A) because the proteins interact with each other (**SFig 4-1A**). As expected, we found that house mouse FAM161A type 2 recruits POC1B to the microtubules (**Sfig 4-3A and D**). However, FAM161A type 3 did not recruit POC1B to the microtubules but instead colocalized with POC1B aggregates (**SFig 4-3E**). This suggests that both isoforms maintained the ability to interact with POC1B, which is expected, since the FAM161A N-terminal domain that mediates the interaction with POC1B is found in both isoforms (**SFig 4-1F**). Finally, co-expressing type 2 with type 3 inhibited type 2 from recruiting POC1B to the microtubules (**SFig 4-3C and D**). These observations suggest that FAM161A type 3 can interact with both FAM161A type 2 and POC1B but specifically lost the ability to interact with microtubules and may act as a dominant negative in vivo. Altogether, the above in vitro observations indicate that house mouse testes express FAM161A protein that is functionally distinct from human FAM161A.

6. Cricetidae and Muridae spermatozoan FAM161A is present only in the distal centriole

FAM161A is a component of the distal and proximal centrioles in basal mammals, such as human, bovine, rabbit, and dog (Khanal et al., 2021) (**SFig 5-1A**). To gain insight into the localization of FAM161A in rodents, we stained mature spermatozoa isolated from the caudal epididymis of house mice, *Peromyscus maniculatus* (deer mouse; family Cricetidae, subgroup Neotominae), and *Microtus ochrogaster* (prairie vole; family Cricetidae, subgroup Arvicolinae) using FAM161A Ab1, POC1B Ab2, and tubulin antibodies (see antibody table for details, **STable 8-1**) (**Fig 5A–C**).

In the house mouse spermatozoan neck, FAM161A labeled a single focus near the axoneme tip, which most likely represents a distal centriolar remnant (**Fig 5A**). The FAM161A focus was uniquely short and wide, unlike in humans, bovines, and rabbits, where it is longer, indicating a distinct localized distribution. FAM161A and tubulin labeling was undetected in the proximal centriole. POC1B labeled a single focus proximal to the nucleus that most likely corresponds to the proximal centriolar remnant. This data suggests that despite centriolar ultrastructural loss in house mice, some centriolar lumen proteins are still present, though in a novel pattern.

Like in house mice, in deer mice, FAM161A labeled a single, short, and wide focus on the distal centriole, indicating that house mice and deer mice have similar FAM161A localization patterns (**Fig 05B**). Also like in house mice, tubulin was not detected in the neck of deer mouse sperm. However, in contrast to house mice, POC1B in deer mice distinctly labeled two foci, as observed in most mammals, which we believe represent the proximal and distal centrioles. Overall, FAM161A and POC1B localization in deer mice show characteristics that are intermediate between most mammals and house mice.

Finally, in prairie voles, which belong to a different Cricetidae subgroup, tubulin was detected in the two spermatozoan centrioles, and FAM161A labeling was similar to that of deer mice and house mice (i.e., showing a wide focus on the distal centriole) (**Fig 05C**). Overall, FAM161A shows a novel, single-focus labeling pattern in Muridae and Cricetidae, indicating that a change in FAM161A localization took place in the common ancestor of these families. Also, these findings support the hypothesis that sperm centrioles gradually evolved in superfamily Muroidea and that proximal centriole degeneration is most extreme in family Muridae.

7. Humans, rabbits, and bovines share a conserved centriole remodeling program

Mammalian spermatozoan centrioles are remodeled from canonical proximal and distal centrioles during spermiogenesis in the seminiferous tubule of the testes (Fishman et al., 2018; Manandhar et al., 1998). To study FAM161A changes during mammalian evolution, we first studied its localization relative to three other

typical centriolar lumen and atypical distal centriolar rod proteins (CETN1, POC5, and POC1B) in basal mammals (with two spermatozoan centrioles), namely humans, rabbits, and bovines. To do this, we performed immunofluorescence (**Fig 6A–C**) and quantified their relative labeling intensities (**Fig 6D–F**). We looked at three sperm cell stages: pre-haploid sperm (spermatogonia and spermatocytes), round spermatids, and elongated spermatids. These stages were identified based on the location of cells relative to basal lamina in the seminiferous tubules, staining with lectin PNA, and the shape of the nucleus (**Fig 6Ai, Bi, & Ci**).

In pre-haploid sperm cells, CETN1, POC5, POC1B, and FAM161A co-localize in the two centrioles (**Sg in Fig 6A–C**). POC1B was detected only with POC1B antibody 2 (Ab2) in pre-haploid sperm of bovine and rabbits (**Sg in Fig 6Aiii–iv & Fig 6Biii–iv**), though this was likely due to a lower reactivity of POC1B antibody 1 (Ab1) in these species and the generally lower immunoreactivity of POC1B at this cell stage (**Sg in Fig 6D–E**). Like POC1B, CETN1, POC5, and FAM161A also showed the lowest immunolabeling intensity at this sperm cell stage in all species, suggesting that later stages are characterized by enrichment of all four proteins (**Sg in Fig 6D–F**). Additionally, the length of CETN1 labeling across all three species was similar (~310 nm), suggesting that before centriole remodeling, the centriolar luminal scaffold has an evolutionarily conserved size (**SFig 6-1A**).

In round spermatids, CETN1, POC5, POC1B, and FAM161A labeling increased in length in the two centrioles (**RS in Fig 6A–C**). Accordingly, the labeling intensity of all four proteins was higher at this stage than at the earlier, pre-haploid stage in all three species (**RS in Fig 6D–F**). In rabbits, FAM161A labeling was undetectable, which was likely due to a weaker immunoreactivity of the FAM161A antibody in this organism. In all three species, CETN1 labeling in the round spermatid proximal and distal centrioles was longer than in pre-haploid sperm centrioles, and distal centriole labeling was longer than that of the proximal centriole (**SFig 6-2**). The length of CETN1 in the round spermatid proximal and distal centrioles was species-specific, being longest in bovine (451±62 and 660±72 nm, respectively), intermediate in rabbit (409±40 and 477±72 nm), and shortest in humans (356±59 and 378±46 nm, respectively) (**SFig 06-1**). Together, these findings in round spermatids suggest that the first stage of remodeling and enrichment of the four rod proteins in the proximal and distal centrioles is conserved, but the size extension is species-specific.

In elongated spermatids, CETN1 and POC5 immunostaining intensity levels in the two centrioles were maintained or declined relative to their levels in round spermatids in all three species (**ES in Fig 6D–F**). In contrast, POC1B and FAM161A showed more intense labeling in elongated spermatids than in round spermatids of all three species (**ES in Fig 6D–F**), while CETN1 showed an inconsistent staining pattern (**ES in Fig 6A–C**). The proximal centriole labeling by the four proteins (which was extended in round spermatids) shortened in elongated spermatids. In the elongated spermatid distal centriole, POC5 reorganized into a "V"-shape in bovine and a wide focus in rabbits and humans. POC1B labeling took on a filled "V"-shape in the distal centriole of bovine elongated spermatids and a wide focus in the distal centriole of rabbit and human elongated spermatids (**ES in Fig 6A–C**). FAM161A labeling reorganized into a "V"- shape in the distal centriole of bovines and rabbits and into a wide focus in humans (**ES in Fig 6A–C**). Together, these findings suggest that the second stage of remodeling is also conserved and includes shortening toward their original length of the four rod proteins in the proximal centriole and the formation of a wider distribution and appearance of two rods in the distal centriole.

Overall, the spermatogenesis findings demonstrate that rod proteins share two conserved remodeling steps with some species-specific length differences. This conservation in distantly related mammalian groups suggests that this program is ancestral in mammals. As part of this program, FAM161A is gradually recruited to the proximal and distal centrioles during spermiogenesis.

The bovine distal centriole begins splaying in round spermatids and is asymmetric in elongated spermatids

This remodeling program may have additional characteristics that are difficult to appreciate with confocal microscopy alone. Therefore, we next performed STORM microscopy in bovine to better understand the organization of centriole remodeling.

Among the species that we studied, bovines had the longest round spermatid centrioles. Therefore, we used high resolution N-STORM microscopy to collect more detailed information about their proximal and distal centrioles (**SFig 6-2A**). We confirmed that the round spermatid proximal centriole is longer than the pre-haploid proximal centriole and that the round spermatid distal centriole is longer than the round spermatid

proximal centriole (**SFig 6-2B**). We noticed that the rostral end of the round spermatid distal centriole was 20–23% wider than its caudal tip, as labeled by CETN1, POC5, and POC1B (**SFig 6-2C**), suggesting that the distal centriole begins splaying in parallel to rod protein extension in round spermatids. Note that at the round spermatid stage, the proximal centriole elongates to form the centriolar adjunct (Garanina et al., 2019; Zamboni and Stefanini, 1971); this indicates that the rod proteins may extend into the centriolar adjunct. When elongated spermatids are oriented such that the proximal centriole is on the right side, we observed using STORM, that the left rod of the bovine distal centriole is longer and wider than the right rod, indicating that distal centriole asymmetry arises as part of centriole remodeling during spermiogenesis (**SFig 6-2D**). Altogether, these findings suggest that the distal centriole begins splaying in round spermatids and that rod asymmetry is apparent in elongated spermatids.

8. Deer mice followed the ancestral centriole remodeling program, but the house mouse pivoted to a centriole degradation program

The primary structure and spermatozoan localization of FAM161A indicated that family Cricetidae has intermediately modified sperm centrioles. Therefore, we next analyzed centriolar luminal protein localization during spermatogenesis in deer mice, a Cricetidae species with a recognizable proximal centriole and modified FAM161A. We found that CETN1, POC5, POC1B, and FAM161A labeling in deer mouse spermatids are consistent with the ancestral remodeling program observed in the basal mammals (i.e., bovines, rabbits, and humans) (**Fig 7A–B**). This finding supports the hypothesis that Cricetidae species undergo a remodeling program that is similar to that of most other mammals.

Next, we analyzed centriolar luminal protein localization during spermatogenesis in house mice (**Fig 7C–E SFig 07-1**). House mouse spermatozoa contain two highly modified centrioles (remnant centrioles) that are characterized by the lack of CETN (Manandhar et al., 1999; Manandhar et al., 1998), a proximal centriole comprised of a few doublet or triplet microtubules, and a distal centriole comprised of the central pair (Leung et al., 2021).

In house mouse pre-haploid sperm cells, like in bovines, rabbits, humans, and deer mice, CETN1 and POC5 co-localize in the two centrioles (**Sg in Fig 7Cii**). POC1B and FAM161A were undetected in house mouse pre-haploid sperm cells (**Sg in Fig 7Ciii–iv)**, which was likely due to the antibodies having a weaker immunoreactivity in house mice than in other species and to the levels of these proteins being lower at this sperm cell stage than at other stages (**Sg in Fig 7Cii–iv** and **Fig 7D**).

In house mouse round spermatids, like in bovines, rabbits, and humans, CETN1, POC5, and POC1B label the proximal and distal centrioles (**RS in Fig 7Cii–iii**), and the length of the labeling is longer in the distal centriole than in the proximal centriole and pre-haploid centrioles (**Fig 7E**). Also, like in bovines, rabbits, and humans, the labeling intensity of the three proteins is higher in round spermatid centrioles than in earlier, pre-haploid sperm cells (**Fig 7D**). Unlike in bovines, rabbits, humans, and deer mice, house mouse FAM161A is present as one or two dot-like structures near the proximal centriole-distal centriole junction (**RS in Fig 7Civ**), and a similar labeling pattern was observed using a second FAM161A antibody (**SFig 7-1**). Together, these round spermatid findings suggest that most aspects of the first stage of centriole remodeling in house mice (centriolar elongation and enrichment of CETN1, POC5, and POC1B in the distal and proximal centrioles) are similar to those observed in other mammals.

In house mouse elongated spermatids, rod protein localization is different between early and late elongated spermatids; this difference is not observed in bovines, rabbits, and humans. Like in bovines, rabbits, and humans, CETN1 and POC5 are present in house mouse early elongated spermatids (**eES in Fig 07Cii–iii**); however, unlike in bovines, rabbits, and humans, CETN1 and POC5 are undetectable in the centrioles of house mouse late elongated spermatids. (**lES in Fig 7Cii–iii**). Also, distinct from bovines, rabbits, humans, and deer mice, POC1B and FAM161A are not enriched in elongated spermatids relative to round spermatids. Rather, FAM161A is observed as a pair of dots between the POC1B-labeled proximal and distal centrioles in late elongated spermatids (**eES & lES in Fig 7Civ**). Together, these findings in house mouse elongated spermatids suggest that the second centriole remodeling stage (centriolar enrichment of POC1B and FAM161A) is dramatically modified in house mice and consistent with a reduction in rod proteins.

Overall, our findings during spermatogenesis demonstrate that, in general, centriolar luminal proteins in house mouse spermatids begin the remodeling process like in other mammalian species but then pivot to becoming reduced in elongated spermatids. This pivot suggests that the house mouse undergoes a derived

551 remodeling program called centrosome reduction (i.e., degradation) (Manandhar et al., 2005), which
552 appears to lead to the absence of sperm centrioles in this organism. In this centrosome reduction (i.e.,
553 degradation) program, FAM161A labels only one structure found at the proximal centriole-distal centriole
554 junction.

555 Discussion

556 Sperm morphology is continuously and rapidly evolving, particularly in internally fertilizing species, as part
557 of a large-scale evolutionary sex cascade (Humphries et al., 2008; Kahrl et al., 2021; Lüpold et al., 2020;
558 Roldan, 2019). This morphological evolution includes the sperm head, tail, and neck, a strategic location
559 connecting the most significant functional units of the spermatozoon (Avidor-Reiss et al., 2017; Tapia
560 Contreras and Hoyer-Fender, 2021; Wu et al., 2020). The simple organization of sperm neck structures is
561 conserved in the spermatozoa of external fertilizers (Jamieson, 1991) but has evolved diverse forms in
562 internally fertilizing species, presumably as part of a reproductive centriole evolutionary cascade (Avidor-
563 Reiss, 2018; Avidor-Reiss et al., 2017). In mammals, the sperm neck contains specialized and unique
564 centriolar structures, such as the atypical distal centriole and striated columns in basal mammals that include
565 humans, and remnant centrioles in murids (Amargant et al., 2021; Fishman et al., 2018; Leung et al., 2021).
566 Here, we show that in murids, centriolar structure and the centriolar protein FAM161A evolve rapidly in
567 association with centriole dispensability for early embryogenesis and acceleratingly with the change in neck
568 attachment to the side of the sperm head. While it was known that atypical centrioles evolve through the
569 remodeling of canonical spermatid centrioles during spermatogenesis after they form the sperm flagella,
570 here, we show that degenerated centrioles in these rodents evolved through modification of the centriole
571 remodeling program.

572 We found that a two-step centriole remodeling program that forms the atypical centriole in humans, rabbits,
573 and bovines is modified, leading to centriole degeneration in murids. We also found that the evolutionary
574 transition from centriole remodeling to centriole degeneration was a gradual process of rodent sperm
575 evolution, during which centriolar composition changed before distal centriolar structure became
576 unrecognizable in murids. We found that some, non-murid rodents, such as deer mice and voles, have
577 centrioles that are intermediate between those of humans and house mice, suggesting that they are a
578 signature of an evolutionary transition. Additionally, we found that the alteration in the centriole remodeling
579 program that leads to centriole degeneration in house mice evolved in association with a change in the
580 sequence and function of FAM161A. We propose that centriole remodeling began to evolve in the rodent
581 suborder Myomorpha, in the ancestor of Muridae and Cricetidae, at or near the time of Eumuroida (note that
582 Eumuroida is a new classification that includes additional families about which we have no information
583 regarding their sperm centrioles (Steppan et al., 2004)). Later, though prior to Muridae, centriole remodeling
584 gradually transitioned to centriole degeneration through modification to the ancestral mammalian centriole
585 remodeling program.

586 Successful reproduction depends on the competitiveness and efficiency of the sperm cell and the fecundity
587 of the female. Rapid evolution of sperm morphology and ultrastructure is often driven by sperm competition
588 (Roldan, 2019). However, adaptations that yield competitive fertilization success may come at a cost to the
589 female or the resultant embryo (Lemaitre et al., 2020; Lüpold and Pitnick, 2018). A recent study showed that
590 in humans and bovines, the centrioles are associated with aneuploidy in the developing embryo and early
591 miscarriages, suggesting that centriole remodeling may reduce fecundity (Cavazza et al., 2021) and that
592 atypical centrioles are associated with reduced reproductive success (Avidor-Reiss et al., 2022). We
593 propose that the evolutionary transition of centrioles with a canonical structure in basal vertebrates and
594 Tetrapods, to an atypical structure in the spermatozoa of most mammals, to a remnant ultrastructure in
595 house mice may have been driven by sperm competition in the rodent lineage. These changes describe a
596 sperm centriole evolutionary cascade that transformed the sperm centriole from an essential structure to
597 one that is dispensable. We predict that other r-strategy mammals would have evolved mechanisms to
598 overcome the costs associated with the atypical centriole. Considering that Cricetidae and Muridae species
599 have centriole-independent embryo development, it is tempting to speculate that the dispensability of the
600 sperm proximal centriole for post-fertilization function relieved it from some evolutionary constraints, allowing
601 it and the head-neck attachment to change.

We also propose that the degradation of the centrioles in house mice is partly attributable to the position of attachment between the head and tail. This change in position may have coevolved with the female reproductive tract (Birkhead et al., 1993; Hook et al., 2021; Roldan et al., 1992; Tung and Suarez, 2021). Species with paddle-shaped sperm heads and tail attachment to the base of the head (most mammals, including humans, rabbits, and bovines) have atypical centrioles. Most of the rodent species with hooked sperm heads and an off-center tail attachment to the base of the head have centrioles with intermediate composition conservation. In contrast, murids, which have sharp, hook-shaped sperm heads and tail attachment on one side of the head, have remnant centrioles. This innovation in murid sperm head and neck morphology may have been fueled by the dispensability of the centrioles.

Collectively, our findings provide the first molecular insight into the rapid diversification and adaptive evolution of centrioles and the neck region in mammalian sperm. In the future, it will be important to identify the specific selective pressures that brought about mammalian centriole remodeling and centriole dispensability in some rodents.

Figures and Figure Legends

Fig 1 – Sperm proximal centriole degradation evolved after the separation of families Cricetidae and Muridae

A) The sperm centriole evolutionary cascade hypothesis. Each panel depicts the spermatozoan head and neck morphology (left), the spermatozoan centrioles (middle, in green), and the zygotic centriolar configuration (right). **i**) Stage 1: the *pre-mammalian centriolar configuration*. Spermatozoon with a ball-shaped head and centrally inserted neck (the tail attached to the center of the head base and is situated below the head base) with canonical proximal (PC) and distal centrioles (DC). Centriole-dependent zygote with two centrosomes emanating asters. **ii**) Stage 2: the *mammalian centriolar configuration*. Sperm competition improved sperm behavior in this stage. Spermatozoon with a paddle-shaped head and centrally inserted neck with canonical proximal and distal centrioles. Centriole-dependent zygote with two centrosomes emanating asters. **iii**) Stage 3: the Eumuroida (subgroup of murids) centriolar configuration. The cost of increased miscarriage rates eliminated the need for zygotic centrioles in this stage. Spermatozoon with a a sickle-shaped head and neck atched to the base ether centrally or off-center (the tail attached asymmetrically to the head base and is situated below the head base) with canonical proximal and distal centrioles. Centriole-independent embryonic development. **iv**) Stage 4: the *murid (house mouse) centriolar configuration*. Spermatozoan centrioles were freed from the functional constraints imposed by the centriole's role in the embryo, allowing for innovation in sperm morphology. Spermatozoon with a sickle-shaped head and lateral head-neck attachment (the tail attached to the head side and situated in parallel to the head base) with remanent centrioles. Centriole-independent embryonic development. **B–E**) A summary of rodent evolution, depicting their phylogenetic tree (**B**), proximal centriolar structure (**C**), head shape (**D**), and neck attachment (**E**). No PC, proximal centriolar structure not observed; uk, unknown; canon, presence of a proximal centriole with canonical structure; sickle, sickle-shaped head; paddle, paddle-shaped head; lateral, neck attachment on one side of the head; O-C base, off-center neck attachment to the base of the head; base, neck attachment near the center of the base of the head.

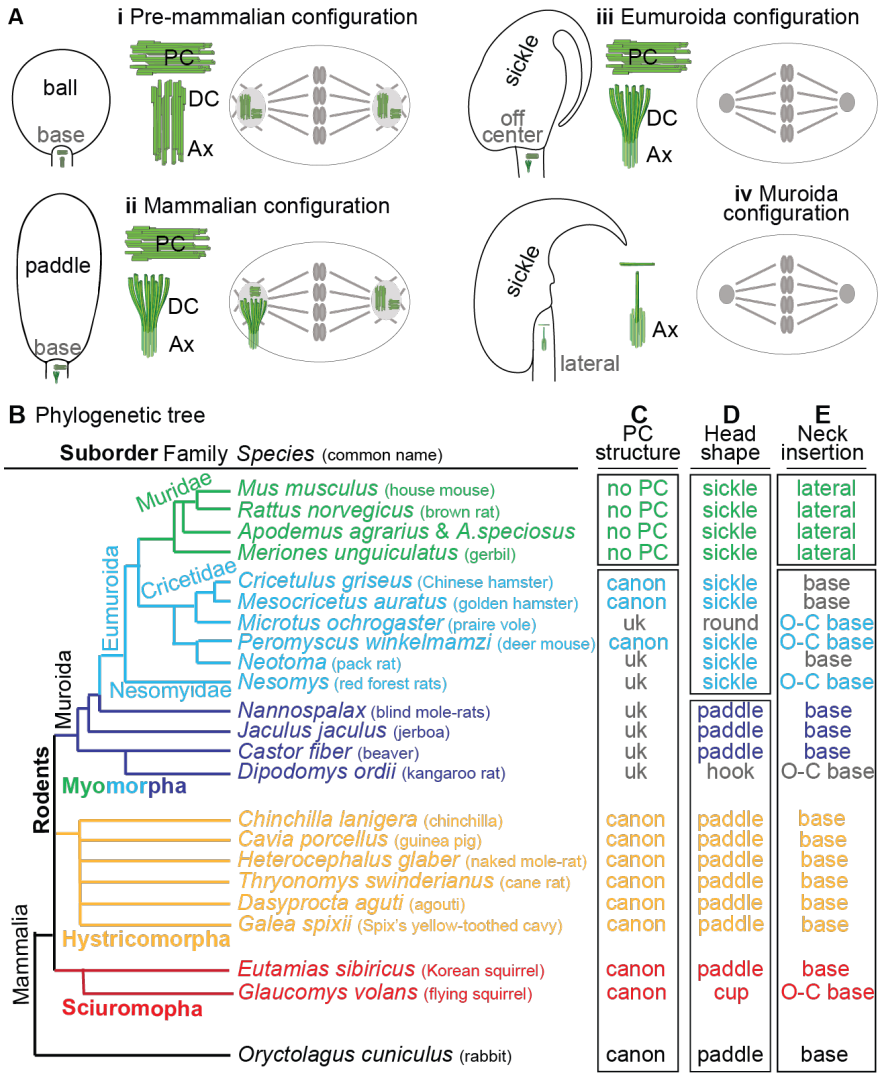

Fig 2 – The primary structure of FAM161A is under selective pressure in rodents

A) Calculated extended identity ratios. **B**) Phylogenetic tree showing the evolutionary position of the four mammals used in the extended identity ratio calculations and their proximal and distal centriolar structures (Steppan and Schenk, 2017). **C–E**) Extended identity ratios calculated for proteins in the FAM161A genomic location (**C**), proteins influenced by sperm competition (**D**), and sperm distal centriolar proteins (**E**). **F–G**) Rodent phylogenetic tree (**F**) with FAM161A sequence identity relative to human FAM161A (**G**). Percent identity is also shown as average ± SD for individual clades. *P<0.05, **P<0.01; ns, not significant. **H**) Bayesian phylogeny of FAM161A inferred using nucleotide sequences of mammalian species. **I**) Bayesian phylogeny of FAM161A inferred using nucleotide sequences of Myomorpha species. The scale bars in H and I represent the number of nucleotide substitutions per site.

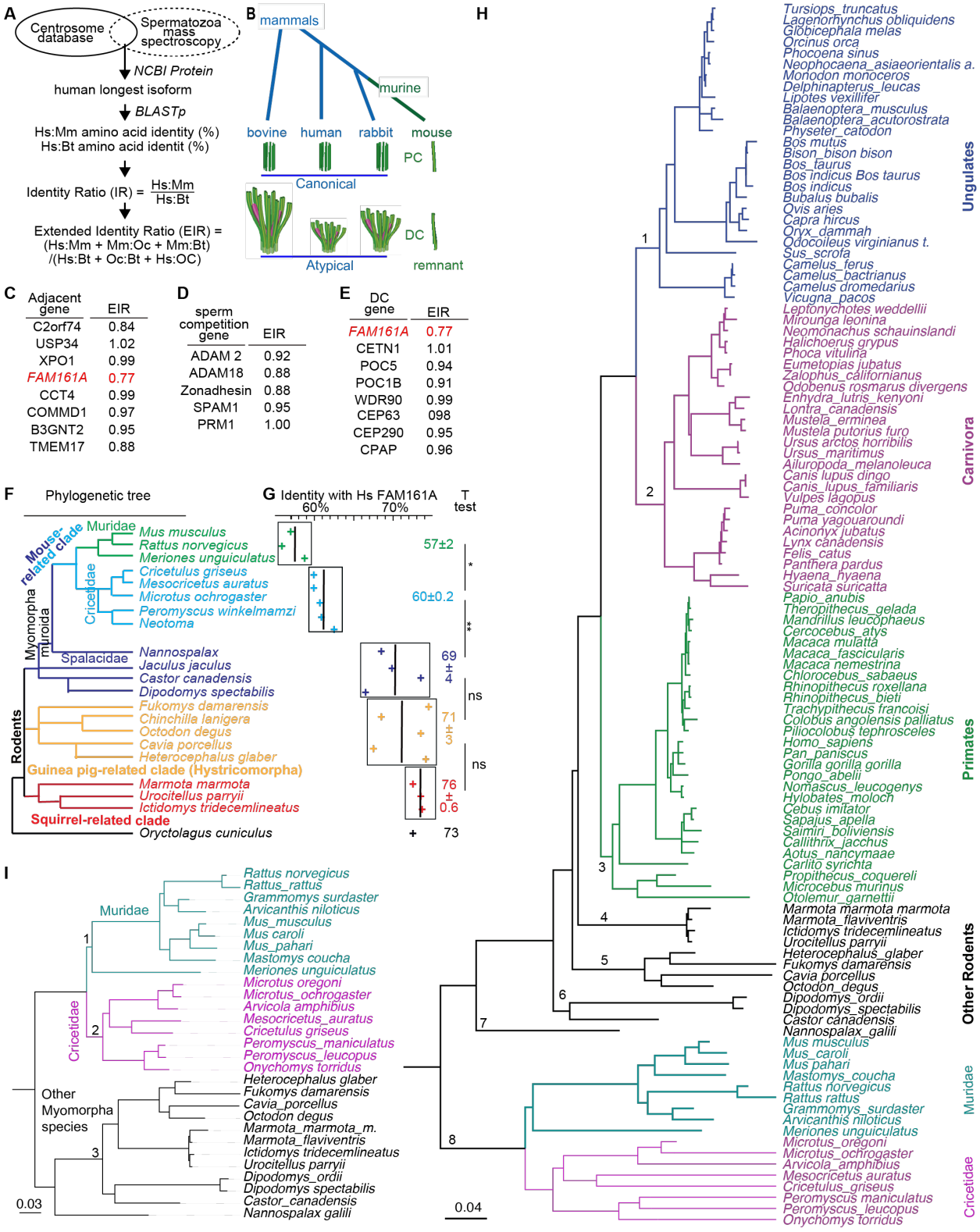

Fig 3 – Murids express a novel FAM161A isoform in the testes

A) Exon organization of FAM161A types 1, 2, 3, and 4 isoforms. ID of predicted FAM161A isoforms and corresponding numbers of amino acids in human and house mice. **B–F**) Western blot analysis of FAM161A in house mouse and rat eyes (**B**), U2OS and 3T3 cells (**C**), bovine and human testes (**D**), and house mouse and rat testes (**E**). **F**) Diagrammatic representation of *Mus musculus* FAM161A with protein domains, positively (+) selected sites identified by CodeML M8 modeling, and negatively (-) selected sites identified by FEL. **G**) AlphaFold-predicted structure of *Mus musculus* FAM161A showing positively selected sites (red) and two apparent primary domains: core and outer.

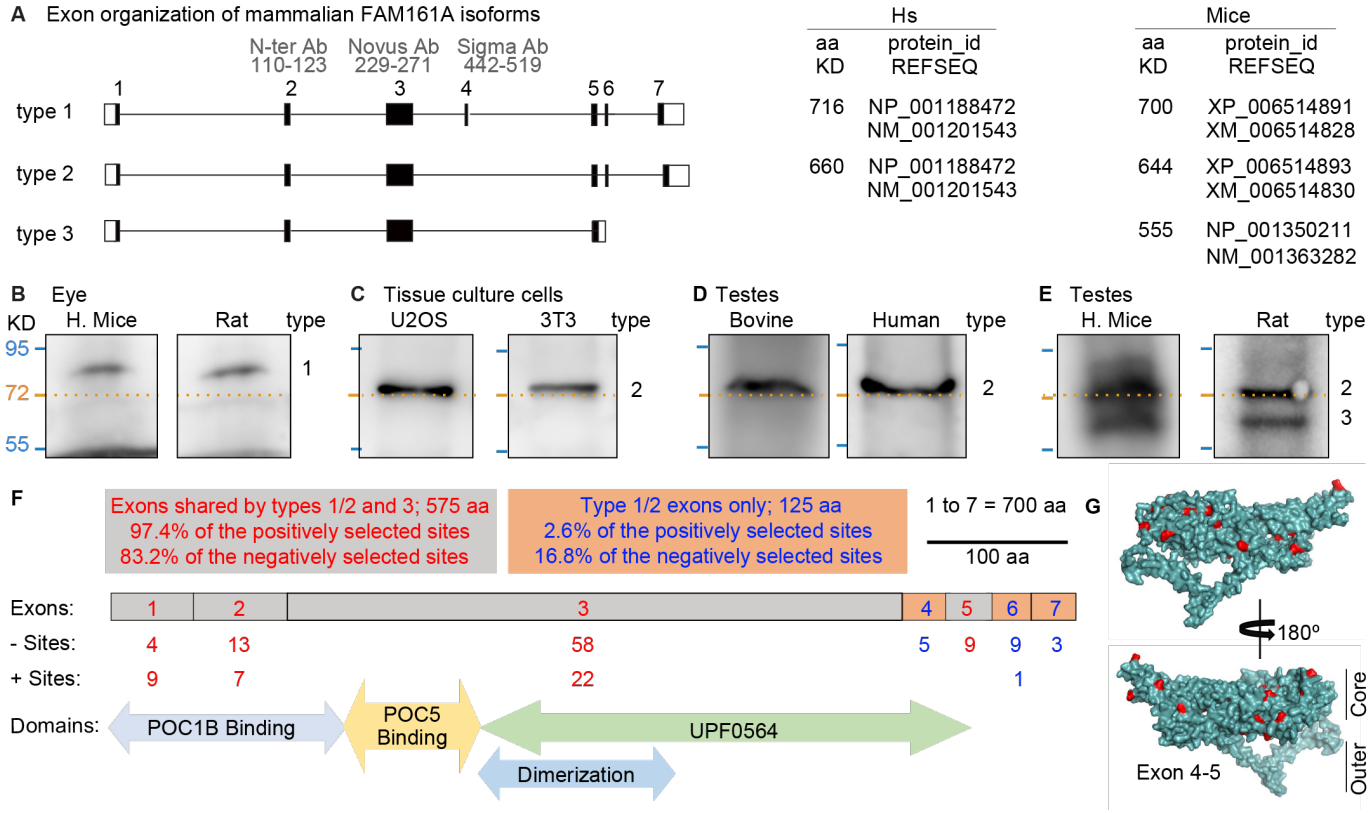

Fig 4 – House mouse FAM161A has a distinct function

A) Expression analysis of human FAM161A (hFAM161A) type 2 (second panel from left), house mouse FAM161A (mFAM161A) type 2 (middle three panels), mFAM161A type 3 (second panel from right), and the combination of mFAM161A types 2 and 3 (right panel) in U2OS cells. **B**) Quantification showing the percentage of cells exhibiting each of the various expression patterns observed during expression analysis of hFAM161A type 2, mFAM161A type 2, mFAM161A type 3, and the combination of mFAM161A types 2 and 3. C, "Cytoplasmic"; I, "Intranuclear"; M, "Mix-nuclear"; P, "Perinuclear". **C**) Quantification of FAM161A colocalization with tubulin. ****p<0.0001, ***p<0.001, **p<0.01, *p<0.05; ns, not significant. Scale bars are 8 µm.

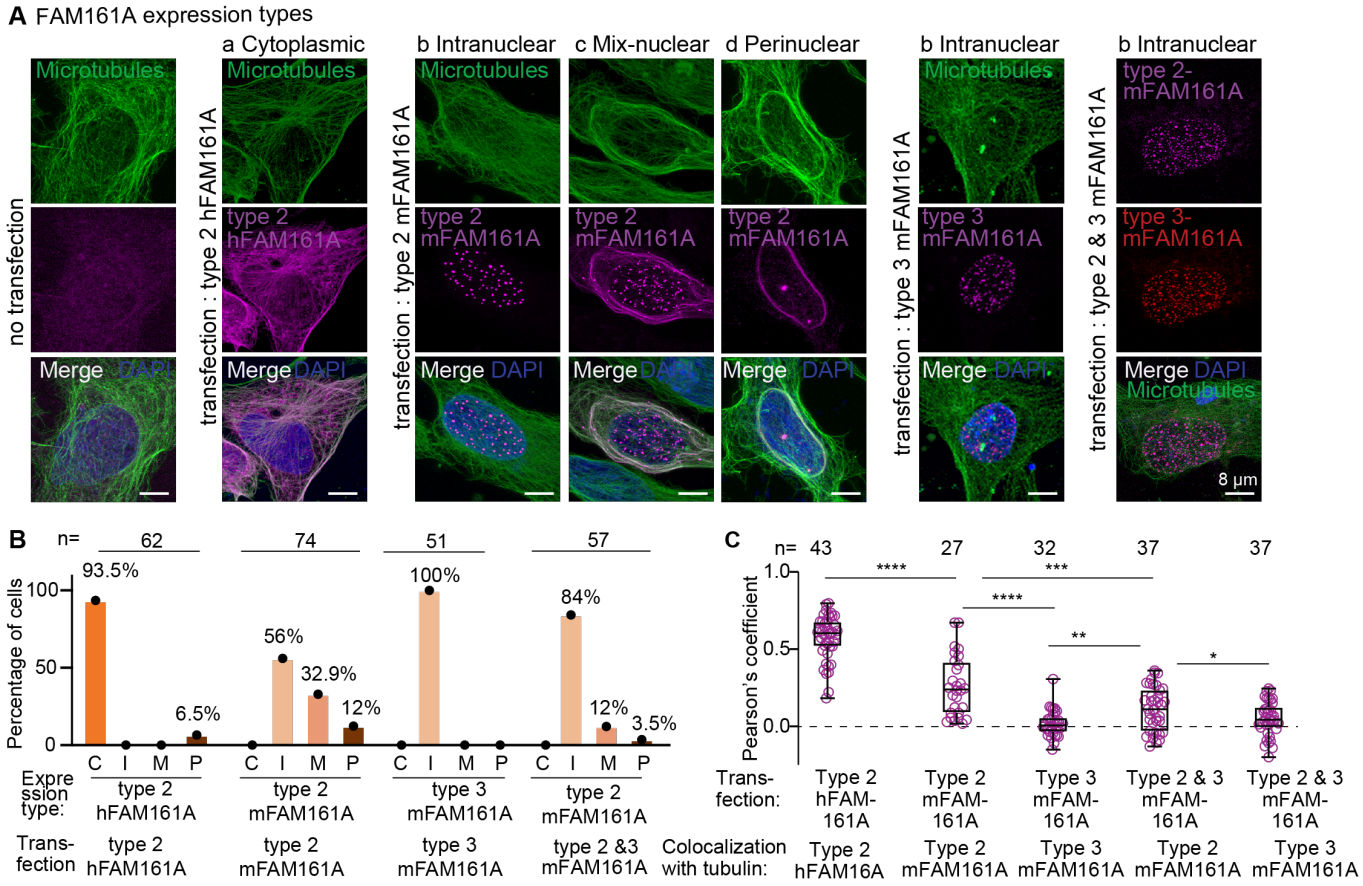

670 **Fig 5 – Cricetidae and Muridae species share a novel FAM161A localization in their spermatozoa**

671 **A–C**) Rod protein localization in mature spermatozoan necks of house mice (**A**), deer mice (**B**), and prairie voles (**C**).
672 Tubulin is used as a marker for the centriole and axoneme. PC, proximal centriole; DC, distal centriole; Ax,
673 axoneme.Scale bars are 1 μm.
674

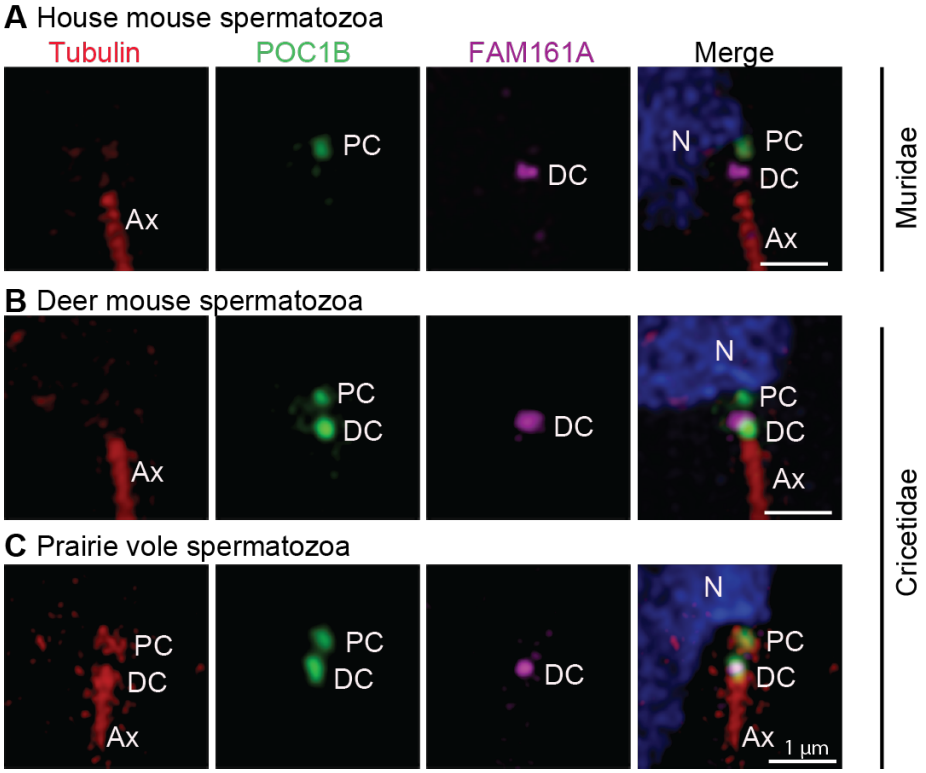

675
676

Fig 6 – Bovines, rabbits, and humans share a conserved centriole remodeling program

A–C) A single seminiferous tubule section showing various stages of spermatogenesis in bovines (**Ai**), rabbits (**Bi**), and humans (**Ci**). The white dotted line indicates the basal lamina boundary. ***Throughout the paper***: BL, basal lamina; Sg, spermatogonia; Sc, spermatocyte; RS, round spermatid; Es, elongated spermatid; Lu, lumen. Scale bars are 8 μm. Representative images of various rod proteins at various stages of spermatogenesis in bovines (**Aii–Aiv**), rabbits (**Bii–Biv**), and humans (**Cii–Civ**). Scale bars are 2 μm. **D–F**) Quantification of centriolar localization of various proteins at various stages of sperm development in bovines (**D**), rabbits (**E**), and humans (**F**). The data was generated from three independent experiments. C1/2, centrioles 1 and 2; PC, proximal centriole; DC, distal centriole; Bt, *Bos Taurus* (bovine); Oc, *Oryctolagus cuniculus* (rabbit); Hs, *Homo sapiens* (human); n, sample size. The two centrioles in Sg are labeled as C1 and C2 since the proximal and distal centrioles are not phenotypically distinguishable at this stage. The graphs are shown as box and whisker plots with interquartile range. ****p<0.0001, ***p<0.001, **p<0.01, *p<0.05; ns, not significant.

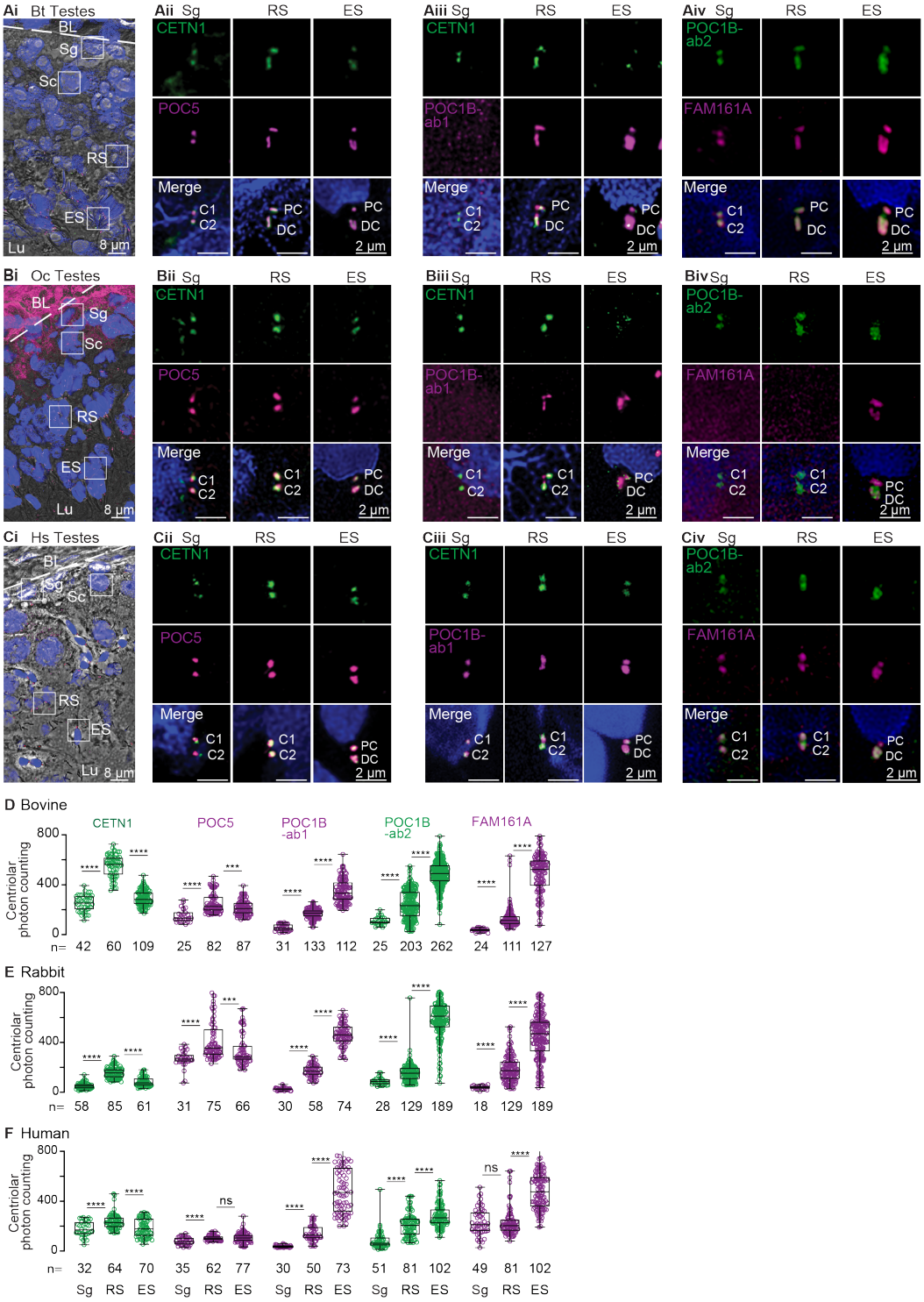

Fig 7 – Unlike the deer mouse remodeling program, the house mouse centriole degradation program begins in elongated spermatids

A & C) A single seminiferous tubule section showing various stages of spermatogenesis in deer mice (**Ai**) and house mice (**Ci**). The white dotted line indicates the basal lamina boundary. BL, basal lamina; Sg, spermatogonia; Sc, spermatocyte; RS, round spermatid; Es, elongated spermatid; Lu, lumen. Scale bars are 8 μm. Representative images of various rod proteins at various stages of spermatogenesis in deer mice (**Aii–Aiv**) and house mice (**Cii–Civ**). **B & D**) Quantification of centriolar localization of various proteins at various stages of sperm development in deer mice (**B**) and house mice (**D**). The data was generated from three independent experiments. **E**) STORM imaging of house mouse testes with POC5 staining in spermatogonia/spermatocytes (Sg) and round spermatids (RS) (left panel). Measurements of centriolar length as determined using STORM imaging (right panel).

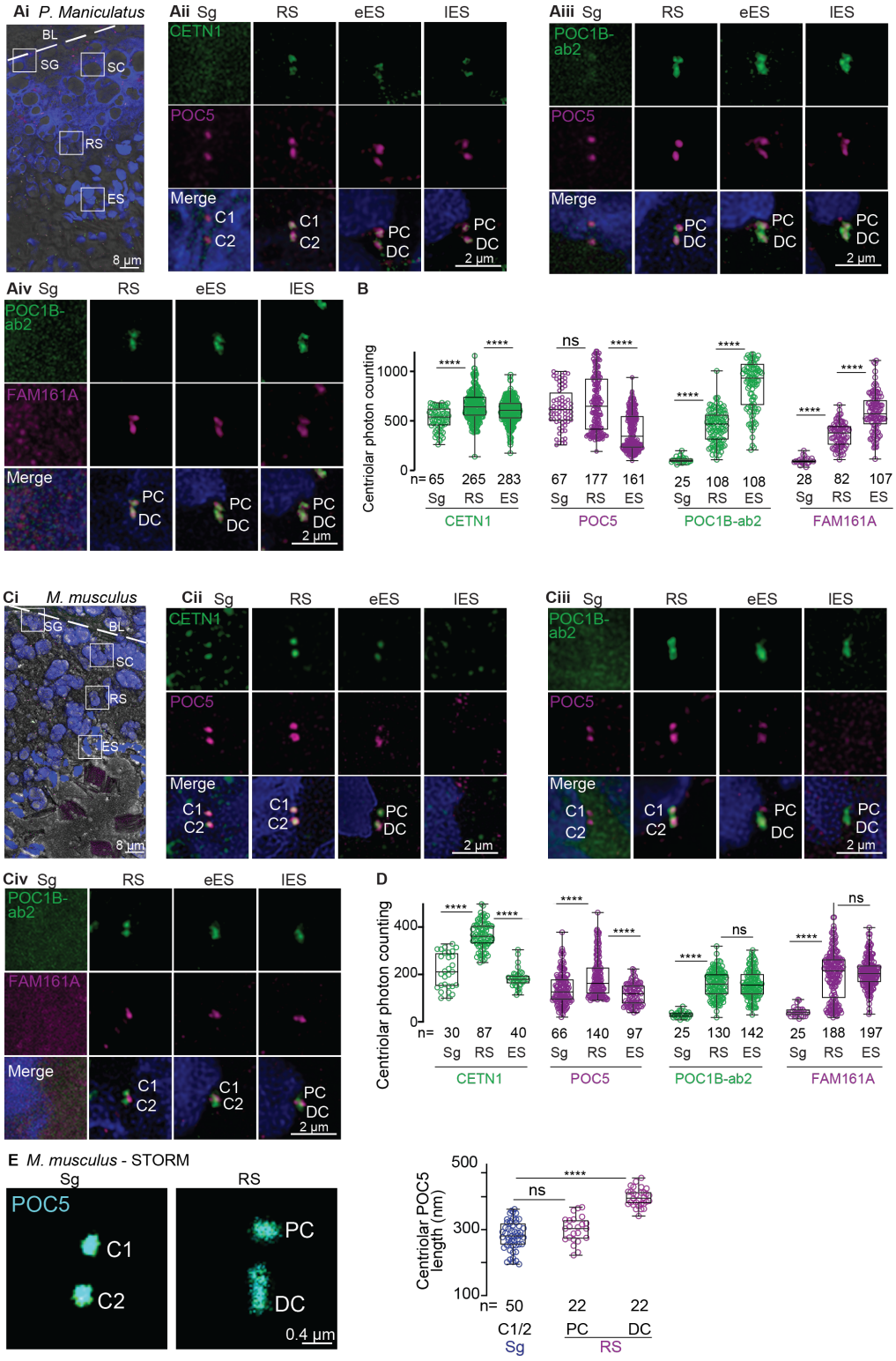

Methods

U2OS cells

U2OS cells were purchased from American Type Culture Collection (cat # CRL-3455). Cells were maintained in Dulbecco's Modified Eagle's Medium (DMEM; Mediatech) supplemented with 10% fetal calf serum (FCS; Atlanta Biologicals) and kept at 37 °C in a humidified atmosphere supplemented with 5% CO_2.

Caudal sperm isolation

Caudal sperm were isolated from sexually mature captive-bred house mice (*Mus musculus* used in a research lab setting), deer mice (*Peromyscus maniculatus bairdii*, BW stock, obtained from the Peromyscus Genetic Stock Center at the University of South Carolina), prairie voles (*Microtus ochrogaster*, obtained from the laboratory of James Burkett at the University of Toledo). Briefly, euthanized rodents were dissected to isolate the testes, from which the caudal epididymis was further isolated. The cauda was moved to a Petri dish containing phosphate-buffered saline (PBS), where it was dissected into small pieces using surgical scissors. The plate was then incubated in a CO_2 incubator at 37 °C for 1 hour to allow sperm to swim out of the caudal tissue. PBS containing swimming sperm was collected in a 15 mL Falcon tube and centrifuged at 1000 × *g* for 8 minutes. The supernatant was discarded, and the pellet was resuspended in an appropriate volume (100–200 µL) of PBS for slide preparation.

Canine semen was obtained from donated ejaculated samples collected manually and cryopreserved with approval from the Cornell University Institutional Animal Care and Use Committee (IACUC). Briefly, following manually collection, samples were diluted 1:1 (v:v) in Irvine Scientific Refrigeration media before being centrifuged at 900 × *g* for 10 minutes. The supernatant was discarded, and the sperm pellet was resuspended with refrigeration media to a concentration of 400 million sperm/mL, then diluted with Irvine Scientific Semen Freezing media to a final concentration of 200 million sperm/mL before being loaded into 0.5 mL straws. Samples were cooled to 5 °C for 1 hour, then placed in liquid nitrogen vapor for 10 minutes before being plunging into liquid nitrogen.

Testes and eye samples

Human testis samples were collected by the University of Toledo Department of Urology with approval from the University of Toledo Institutional Review Board (IRB). Rabbit testis samples were provided by Dr. Jie Xu at the University of Michigan. Bovine testes were purchased from Scholl's slaughterhouse in Blissfield Michigan. House mouse, rat, and prairie vole testes were collected from discarded euthanized research animals at the University of Toledo Department of Laboratory Animal Resources and the laboratory of Dr. James Burkett. Deer mouse testes were collected from discarded research animals at the University of Maryland.

Preparation of slides for immunofluorescence studies

Sperm samples isolated according to the protocol described in the "Caudal sperm isolation" section were further processed for immunofluorescence studies. Briefly, approximately 20 µL of sperm suspension in PBS buffer were placed on glass slides (Azer Scientific EMS200A+), cover slips (VWR, Cat. 48366-205) were applied, and the slides were dropped into liquid nitrogen. Slides were stored in liquid nitrogen until needed for immunostaining.

Preparation of testes for confocal and STORM imaging

Pieces of testis samples were embedded in OCT (EMS Diasum 62550-01), and the OCT-embedded testes were then frozen on dry ice and cryo-sectioned. For confocal microscopy, 8-µm sections were made and placed on glass slides. For STORM imaging, 2-µm sections were made and placed on 18-mm round cover slips. Sections were stored in a -80 °C freezer until needed for immunostaining.

Antibodies

Primary and secondary antibodies were purchased from various suppliers (**STable 8-1**). Concentrations of various antibodies used for confocal and STORM microscopy are listed in the table below.

Immunostaining for confocal and STORM imaging

Immunostaining of sperm and testes for confocal imaging: slides containing sperm samples were removed from liquid nitrogen, coverslips were removed using forceps, and the slides were placed in a Coplin jar containing pre-chilled methanol for 3 minutes. Similarly, slides containing testis sections were removed from the -80 °C freezer and immediately placed in pre-chilled methanol for fixation. Next, the slides were placed in PBS for 1 minute, then incubated for 60 minutes at room temperature in fresh PBS with 0.3% Triton X-1000 (PBST) for permeabilization. Blocking was then performed by placing the slides in 1% PBST-B (1% bovine serum albumin (BSA) in PBST solution) for 1 hour. Slides were then removed from PBST-B, and primary antibodies diluted in PBST-B were added. The slides were then covered with parafilm tape, placed in a humidity chamber, and incubated overnight at 4 °C. On the following day, the slides were washed three times in PBST for 5 minutes per wash. Next, the secondary antibody mixture was prepared by adding secondary antibodies and Hoechst (Cat. #H3569, Thermo-fisher Scientific, 1:200) to a PBST-B solution. The secondary antibody mixture was then added to the slides, which were covered with parafilm and incubated for 3 hours at room temperature. Slides were then washed three times with PBST for 5 minutes per wash, followed by three washes with PBS for 5 minutes per wash. The slides were then covered with cover glass (18 × 18 mm), sealed using clear nail polish, and stored at 4 °C until needed for imaging.

Immunostaining of testis samples for STORM imaging: immunostaining was performed as described above with slight modifications. Incubation in primary antibody was done for 24 hours at 4 °C, and incubation in secondary antibody was done for 4 h at room temperature. PBST and PBS washes after primary and secondary antibody incubations, respectively, were performed five times for 5 minutes per wash. After washing, the cover glasses were stored in PBS at 4 °C. Imaging was performed within 24 to 48 hours.

Confocal imaging

Immunostained slides were imaged using a Leica SP8 confocal microscope. Images were processed using the Leica HyVolution 2 System. Images were captured at a magnification of 63X and a zoom of 1.5X, with a pixel density of 2048 × 2048. Using Adobe Photoshop, confocal images were cropped to 200 × 200 pixels or 65 × 65 pixels. The overall intensities of the images were modified to allow easy visualization, and panels were resized to 1 × 1 inch at 300 DPI for publication.

3D STORM Imaging

3D STORM imaging was performed using a Nikon N-STORM 4.0 system on an Eclipse Ti inverted microscope, an Apo TIRF 100X SA NA 1.49 Plan Apo oil objective, 405-, 561-, 488-, and 647-nm excitation laser lines (Agilent), and a back-illuminated EMCCD camera (Andor, DU897). The 647-nm laser line was used to promote fluorophore blinking. A 405-nm laser was used to reactivate fluorophores. Approximately 30,000 time points were acquired at a 20 Hz frame rate, each measuring 16–20 ms in duration. NIS-Elements (Nikon) was used to analyze and present the data.

Cover glasses were mounted on a depression slide in imaging buffer (10% dextrose in 100 mM Tris at pH 8.0, 25 mM β-Mercapto-ethylamine, 0.5 mg/mL glucose oxidase, and 67 µg/mL catalase). Each cover glass was sealed with Body Double SLK (SO56440A and SO5644B) and allowed to air dry for 3 minutes, after which the sample was processed for imaging. For imaging various cells in the testes, cells were identified using the phase contrast objective based on their location relative to basal lamina. Once each cell type was identified, the objective was switched to the TIRF (total internal reflection fluorescence) objective, and each cell was imaged. All STORM imaging for each figure was replicated at least three independent times. Data shown in all figures are cumulative of all replicates.

Z-Calibration was performed using fluorescent beads and stored as a file for each objective and buffer condition according to the manufacturer's instructions. For our STORM analysis, all images were taken using the 100X objective and the same buffer (see above). The raw acquisition data obtained for all STORM images were analyzed using NIS-Elements. Analyzed images were exported as TIFF files. Publication-ready STORM images were prepared in Adobe Photoshop by cropping to 300 × 300, 100 × 100, or 65 × 65 pixels and resizing cropped images to 1 × 1 inch at 300 DPI. The background intensity of the entire image was enhanced for clear visualization of the sperm head.

796 **Western blot**

797 Testis protein extraction was performed in RIPA buffer with a cocktail of protease inhibitors (Roche cat.
798 11836170001), which was freshly added before beginning protein extraction. Testes were collected and
799 stored in liquid nitrogen until protein extraction, at which time, the testis sample was placed in ice for 10
800 minutes, then minced into small pieces. Approximately 300–500 µL of RIPA buffer was added, and the whole
801 tissue sample was homogenized. The sample was incubated on ice for 1 hour, with brief vortexing every 10
802 minutes. The sample was then centrifuged at 15,000 × *g* for 20 minutes at 4 °C. The supernatant was then
803 collected, loading dye was added, and the mixture was boiled for 10 minutes. After boiling, the sample was
804 centrifuged again at 15,000 × *g* for 10 minutes to sediment any precipitate and to clear any particles from
805 the lysate. The lysate was aliquoted and stored in a -80 °C freezer until needed for western blotting. Each
806 sample was run in either 6% or 8% SDS polyacrylamide gel, then transferred to a PVDF membrane. After
807 transfer, the membrane was blocked in 5% TBSTB (5% BSA in TBST solution), then incubated in primary
808 antibody (see **STable 8-1** for antibody concentration) overnight at 4 °C. The membrane was washed three
809 times with TBST for 5 minutes per wash, then incubated in HRP-conjugated secondary antibody for 1 hour
810 at room temperature. Radiance Plus (Azure Biosystem, cat. S1006) was used to detect peroxidase activity.
811 Molecular masses were determined using an EZ-Run Prestained Rec Protein Ladder (Fisher BioReagents,
812 cat. BP3603-500) and an Accu Prestained Protein I Ladder (Lambda Biotech, cat. G01). Western blot
813 imaging was performed using an Azure Imaging System Model 600. Publication-ready western blot images
814 were prepared in Adobe Photoshop.

815 **Bioinformatic analysis**

816 The longest isoforms of all analyzed proteins were obtained from the NCBI database. Proteins were
817 compared using the NCBI pBLAST tool, and percent identity for FAM161A was extracted. Extended identity
818 ratios were calculated by dividing the sum of house mouse FAM161A percent identities with humans,
819 rabbits, and bovines by the sum of FAM161A percent identities between humans, rabbits, and bovines.

820 **Intensity measurement by photon counting**

821 For intensity measurements of the various proteins by antibody labeling, images were captured using a
822 confocal microscope in counting mode. All images were captured using a constant laser power of 5%. The
823 images were then analyzed for protein intensity using the Leica LAS X program. Briefly, a round region of
824 interest (ROI) 1.5 µm in diameter was drawn to encompass the proximal centriole and distal centriole, from
825 which pixel sum intensity was recorded and exported into a Microsoft Excel spreadsheet for additional
826 calculations.

827 **Colocalization analysis**

828 For colocalization analysis, a group of transfected cells were randomly selected on a slide, and images were
829 captured using a confocal microscope in counting mode. An ROI was drawn to surround every transfected
830 cell. The Pearson correlation coefficient of colocalization (r) was measured using the colocalization
831 measurement tool in the Leica LAS X program.

832 **STORM image quantification**

833 Measurements of proximal and distal centriolar dimensions captured by STORM were performed using
834 Nikon's NIS-Elements imaging software. No STORM images were excluded from quantification. All images
835 were quantified for all parameters as much as possible. To measure proximal and distal centriolar lengths
836 and widths, a line starting at 50% of the first intensity peak through 50% of the last intensity peak was drawn
837 and measured along each length and width.

838 **Transfection**

839 Transfection of U2OS cells was performed for colocalization studies. The cells were transfected using
840 GenJet™ In Vitro DNA Transfection Reagent (SignaGen Laboratories, catalog # SL100489-OS) for U2OS
841 Cells as instructed. Briefly, the cells were divided into 6-well plates 12 hours before transfection. On the
842 following day, at least 1 hour before transfection, the media was replaced with 1 mL of fresh DMEM complete
843 media. Then, in one set of 1.5 mL microcentrifuge tubes, the DNA mixture was made in 50 µL incomplete

844 DMEM media. Note that a total of 1 µg of DNA was added to make the DNA mixture. In all transfection
845 reactions, an equal amount of DNA was added. In another set of microcentrifuge tubes, the reagent mixture
846 was made by adding 3 µL of transfection reagent to 50 µL incomplete DMEM media. The reagent mixture
847 was then added to the DNA mixture, vortexed briefly, and incubated at room temperature for exactly 15
848 minutes. The transfection reaction was then added to the culture, and the plates were shaken well to
849 uniformly distribute the reaction mixture. The transfected cells were then incubated at 37 °C in a 5% CO_2
850 incubator for 48 hours. Finally, the transfected cells were processed for immunostaining and confocal
851 imaging.

852 **Constructs and plasmids**

853 House mouse FAM161A cDNA of type 2 (transcript variant X3, accession number XM_006514830.3) and
854 type 3 (transcript variant 1, accession number NM_001363282.1) was purchased from GenScript (Clone
855 IDs OMu45282 and OMu45285, respectively). FAM161A type 2 was tagged with FLAG, and type 3 was
856 tagged with HA. Both isoforms were cloned into a pcDNA 3.1 mammalian expression vector using an
857 NEBuilder® HiFi DNA Assembly kit (cat # E5520S, New England Biolabs). We obtained human FAM161A
858 cDNA in p3XFLAG-CMV-7 from Dr. Frans P.M. Cremers (Roosing et al., 2014). pGBKT7 and pGADT7
859 plasmids for yeast two-hybrid assays were obtained from Dr. Scott Crawley at the University of Toledo.
860 pIC194-POC1B was reported previously (Cekic, 2017). POC5-GFP was obtained from Dr. Michel Bornens.
861 All cloning was performed using either the NEBuilder® HiFi DNA Assembly Cloning kit or the classical
862 digestion and ligation method. Cloning was confirmed by colony PCR, and the accuracy of cloned DNA
863 sequences was confirmed by sequencing.

864 All interaction mapping was performed using human FAM161A type 2, human POC1B, and human POC5.
865 FAM161A fragments (141–660 and 230–161) were cloned in a p3XFLAG-CMV-7 mammalian expression
866 vector.

867 **Yeast two-hybrid assay**

868 The GAL4-based yeast two-hybrid system was used to identify binary protein-protein interaction and to
869 construct an interaction map. The constructs encoding full-length FAM161A, POC5, POC1B, and their
870 various fragments were fused to either the DNA binding domain (GAL4-BD) in a pGBKT7 plasmid or the
871 DNA activation domain (GAL4-AD) in a pGADT7 plasmid. Protein interaction was studied by transforming
872 different combinations of GAL4-BD and GAL4-AD DNA constructs in the AH109 yeast strain. Yeast was
873 transformed using the Frozen-EZ Yeast Transformation II Kit (#T2001) from Zymo Research.

874 Positive transformation of both plasmids was selected for using double dropout media (DDO) lacking Leu
875 and Trp. The interaction was confirmed by growing yeast in media of varying stringency levels and by using
876 triple (TDO, -Leu, -Trp, -His) and quadruple dropout media (QDO, -Leu,-Trp,-His,-Ade).

877 **FAM161A mRNA amplification and sequencing**

878 mRNA Extraction: Testes and eyes were collected from euthanized house mice and stored in liquid nitrogen
879 until mRNA extraction, which was performed using the Roche mRNA Isolation kit (Cat. No. 11741985001).
880 In summary, ~100 mg of snap-frozen tissue was ground to a homogenous powder in a pre-cooled mortar
881 and added to 1.5 mL lysis buffer pre-chilled to 0 °C. The powder suspension was then homogenized by
882 passing 4 times through a 21-gauge needle and centrifuged at 11,000 × *g* for 30 seconds, after which the
883 supernatant was transferred to a "sample tube." The following steps were then performed on ice (at a
884 temperature between 0 °C and -4 °C): 150 µL re-suspended streptavidin-coated magnetic particles (SMPs)
885 were pipetted into a fresh tube, then immobilized on the side of the tube using a magnetic particle separator
886 (Permagen® Labware, PN: MSR06). SMP storage buffer was then removed, and SMPs were re-suspended
887 in 250 µL lysis buffer. SMPs were again immobilized with the magnetic particle separator, and all lysis buffer
888 was removed. Next, 1.5 µL biotin-labeled oligo$(dT)_{20}$ probe was added to the sample tube and mixed with
889 the sample to form a "hybridization mix." The hybridization mix was then added to the previously prepared
890 SMPs, the SMPs were resuspended, and the mixture was incubated on ice for 5 minutes. Following
891 incubation, SMPs were separated from the mixture with the magnetic particle separator. The SMPs were
892 then resuspended in 250 µL wash buffer and separated from the buffer using the magnetic particle
893 separator, after which all wash buffer was removed and discarded; this series of steps was repeated two

894 more times. SMPs were then re-suspended in 25 µL double-distilled water and incubated for 2 minutes at
895 65 °C on a metal heat block. SMPs were then separated from the eluate with the magnetic particle separator,
896 and the supernatant (~25 µL, containing the mRNA) was transferred to a fresh, RNase-free tube.

897 3' RACE: First-strand cDNA synthesis was performed using the Roche 5'/3' RACE Kit, 2nd Generation (Cat.
898 No. 03353621001). In summary, the following were pipetted into a sterile, 0.2-mL Thermowell® Gold PCR
899 Tube (Corning, Inc.) on ice, mixed, and spun down briefly: 4 µL cDNA Synthesis Buffer, 2 µL
900 Deoxynucleotide Mixture, 1 µL Oligo d(T)-Anchor Primer, 5 µL total RNA from the mRNA Extraction step
901 above, 1 µL Transcriptor Reverse Transcriptase, and 7 µL double-distilled water. The mixture was then
902 incubated in a C1000 Touch™ Thermal Cycler (Bio-Rad) for 60 minutes at 55 °C, then for 5 minutes at 85
903 °C.

904 The cDNA was then directly amplified by PCR. In summary, the following were pipetted into a sterile
905 microcentrifuge tube on ice, mixed, and spun down briefly: 2 µL cDNA product from the previous step, 2.5
906 µL primer name 2FW, 2.5 µL PCR Anchor Primer,1 µL Deoxynucleotide (dNTP) Solution Mix (New England
907 Biolabs, Inc., N0447L), 10 µL Q5® Reaction Buffer (New England BioLabs, Inc., B9027SVIAL), 10 µL Q5®
908 High GC Enhancer (New England BioLabs, Inc., B9028AVIAL), 0.5 µL Q5® High-Fidelity DNA Polymerase
909 (New England BioLabs, Inc., M0491LVIAL), and 21.5 µL double-distilled water. The reaction mix was placed
910 in a C1000 Touch™ Thermal Cycler, and PCR was run with the following conditions: initial denaturation at
911 98 °C for 30 seconds; 35 cycles of denaturation at 98 °C for 10 seconds, annealing at 55 °C for 30 seconds,
912 and extension at 72 °C for 2.5 minutes; final extension at 72 °C for 2 minutes; and indefinite hold at 4 °C.
913 10 µL of the first PCR amplification product was then used for analysis on a 2% ethidium bromide-stained
914 agarose gel (120 minutes at 80V in a Mini-Sub® Cell GT gel chamber connected to a PowerPac™ HC (Bio-
915 Rad) power supply) with a 1kB Plus DNA Ladder (New England BioLabs, Inc., N3200L) as molecular weight
916 marker.

917 For the second PCR amplification, the following were pipetted into a sterile, 0.2-mL Thermowell® Gold PCR
918 Tube on ice, mixed, and spun down briefly: 2 µL first PCR amplification product, 2.5 µL primer name 3FW,
919 2.5 µL primer name 5RV, 5*RV, or 7RV, 1 µL dNTP Solution Mix, 10 µL Q5® Reaction Buffer, 10 µL Q5®
920 High GC Enhancer, 0.5 µL Q5® High-Fidelity DNA Polymerase, and 21.5 µL double-distilled water. The
921 reaction mix was placed in a C1000 Touch™ Thermal Cycler, and PCR was run with the following conditions:
922 initial denaturation at 98° C for 30 seconds; 35 cycles of denaturation at 98°C for 10 seconds, annealing at
923 58° C for 30 seconds, and extension at 68° C for 2.5 minutes; final extension at 72° C for 2 minutes; and
924 indefinite hold at 4° C. All 50 µL of the second PCR amplification product was then used for analysis on a
925 2% ethidium bromide-stained agarose gel (120 minutes at 80V in a Mini-Sub® Cell GT gel chamber
926 connected to a PowerPac™ HC power supply) with a 1kB Plus DNA Ladder as molecular weight marker.
927 DNA bands were visualized and imaged using a DIGI DOC-IT High Performance Ultraviolet Transilluminator
928 (UVP, P/N 97-0105-01), then excised and placed individually in 2-mL centrifuge tubes (G-Biosciences, Cat.
929 #C041-D) for DNA purification.

930 DNA Purification: DNA purification was performed using the QIAquick® Gel Extraction Kit (cat. Nos 28704
931 and 28706) with slight modifications. In summary, 700 µL Buffer QG was added to the tube containing an
932 excised agarose gel slice. The tube was then incubated for at least 10 minutes at 50 °C on a metal heat
933 block and vortexed every 2 to 3 minutes until the gel slice was completely dissolved. Then, 350 µL
934 isopropanol was added to the tube and mixed. Approximately 525 µL of the sample was then applied to a
935 QIAquick® spin column seated in a provided 2 mL collection tube and centrifuged for 1 minute at 15,000
936 RPM. The flow-through was discarded, the QIAquick® column was placed back into the same collection
937 tube, and the loading and spin was repeated with the remaining volume of the sample, followed by placement
938 of the QIAquick® column back into the same collection tube. To wash the sample, 750 µL Buffer PE (with
939 ethanol added) was added to the QIAquick® column and allowed to stand for 5 minutes at room temperature,
940 then centrifuged for 1 minute at 15,000 RPM. The flow-through was discarded, the QIAquick® column was
941 placed back into the same collection tube, and the column was centrifuged for an additional 2 minutes at
942 15,000 RPM to remove residual wash buffer. The column was then placed into a clean, 1.5-mL
943 microcentrifuge tube. To elute DNA, 15 µL sterile water warmed to 65 °C on a metal heat block was added
944 to the center of the QIAquick® membrane and incubated for 5 minutes at room temperature, then centrifuged
945 for 2 minutes at 15,000 RPM. To increase the yield of purified DNA, the previous elution steps were
946 repeated. Purified DNA was then prepared for sequencing.

947 DNA Sequencing: Purified DNA was prepared for sequencing by pipetting the following into a sterile, 0.2-
948 mL Thermowell® Gold PCR Tube (Corning, Inc.): 2 µL purified DNA, 2.5 µL sequencing primer (primer name
949 Seq. 3FW, Seq. 5RV, Seq. 5*RV or Seq. 7RV), 10.5 µL sterile water (see **STable 8-2** for primer information).
950 Sequencing was performed by GENEWIZ (Azenta Life Sciences), and sequencing results were analyzed
951 using Sequencher 5.2.2 (Gene Codes Corporation).

952 **Statistical analysis and reproducibility**

953 Unless otherwise noted, each experiment was independently performed at least three times with similar
954 results. All averages and standard deviations in this study were calculated using Microsoft Excel. All
955 correlations, regressions, and *t*-test analyses were performed using GraphPad Prism 8.0. In each figure or
956 figure legend, the number (n) of cells analyzed and all *P*-values are specified. An unpaired, two-tailed *t*-test
957 was used to perform the statistical analysis in this study. All quantification data are presented as box and
958 whisker and scatter plots. All box and whisker plots are represented as minimum to maximum, showing all
959 data points, medians, and interquartile ranges. Each data point in all scatter plots represents a measurement
960 for an individual cell. *P*-values are indicated as asterisks (*) denoting the significance of comparison:
961 $*P<0.05$, $**P<0.01$, $***P<0.001$, $****P<0.0001$.

962 **Estimation of ω (dN/dS) across centriolar proteins**

963 Codon alignments and phylogenetic tree topologies of FAM161a, FAM161b, CETN1, POC5, POC1b and
964 WDR90 were used for the estimation of ω across the gene. We employed the CODEML null model (M0) of
965 the PAML suite to estimate ω across codon alignments. We estimated ω for FAM161a orthologs from
966 Rodents, Carnivores, Ungulates and Primates using the respective coding DNA sequence (CDS)
967 alignments. We also estimated ω in individual subgroups of Rodents (Muridae, Cricetidae and other
968 myomorpha species).

969 **Identification of sites under positive and negative selection within rodent groups**

970 We used several of the tests for identifying sites under selection available through the HyPhy suite. The
971 Mixed Effects Model of Evolution identifies sites under episodic diversifying / positive selection, whereas
972 FUBAR and FEL identify sites under pervasive positive / negative selection across codon alignments.

973 **Ortholog search**

974 We extracted FAM161A orthologs for rodents, ungulates, carnivores, and primates from the NCBI Ortholog
975 list. The longest mRNA transcript sequence of the longest isoform (isoform X1) was selected for all species
976 analyzed (**STable 8-3**). We used house mouse FAM161A as a query and performed a tBLASTn search
977 against rodent taxa to identify orthologs missing from the NCBI ortholog list (last accessed). We used the
978 AUGUSTUS gene prediction tool to identify the CDS of all FAM161A orthologs to ensure the correct coding
979 frame of the gene. We gathered a total of 115 orthologs from four mammalian groups.

980 **Sequence alignment and phylogenetic reconstructions**

981 The CDS of individual animal groups were aligned using MUSCLE (Edgar, 2004). The CDS was translated
982 into its amino acid sequence before alignment and reverse translated to recover the aligned codon positions.
983 Alignments were manually curated by removing gaps and stop codons. Phylogenetic trees were constructed
984 by employing a Bayesian phylogenetic framework. The model of sequence evolution was determined using
985 the ModelFinder program in IQTree (Kalyaanamoorthy et al., 2017). Phylogenetic reconstruction was
986 performed using MrBayes (Ronquist et al., 2012) with GTR+I+G as the model of sequence evolution. We
987 parallelized four MonteCarlo chain simulation runs to execute the analysis and terminated the analysis when
988 the standard deviation of split frequency reached less than 0.01. The models and tree were sampled every
989 100th generation, and after the simulation was complete, the initial 25% of the sampled trees and their
990 corresponding parameters were discarded as burn-in. Fine tree topography and node support values were
991 estimated for the tree data that was retained after excluding burn-in. The tree was visualized using FigTree
992 (Rambaut).

993 **Selection analysis**

994 We implemented maximum likelihood-based selection models in CodeML binaries within the PAML package
995 (Yang, 2007) to test the nature of selection acting on FAM161A orthologs in different species groups. The
996 ratio of non-synonymous substitutions (nucleotide substitutions that change the protein sequence, denoted
997 dN) to synonymous substitutions (nucleotide substitutions that do not change the protein sequence, denoted
998 dS), known as 'ω' (dN/dS), was estimated across codon positions to identify the signature of selection. We
999 compared the likelihoods of two pairs of models, M7 (null model) vs. M8 (alternate model) and M8a (null
1000 model) vs. M8 (alternate model). M7 and M8a are neutral models, whereas M8 is a positive selection model.
1001 The significance of the difference between the likelihood values of both models was compared using chi^2
1002 distribution. Amino acid sites evolving under the influence of positive selection ($\omega > 1$) were identified using
1003 the Bayes Empirical Bayes (BEB) by M8 selection model. Furthermore, we used MEME to identify the
1004 episodic effect of natural selection and FEL and FUBAR to identify the sites under pervasive effect of
1005 selection.

1006 We further applied branch-site models in PAML to check the lineage-specific effect of positive selection in
1007 the Muridae and Cricetidae branches of rodent phylogeny. We ran M1 and M1a models and compared the
1008 significance of the difference between likelihood values using a chi^2 test.

Data availability

Relevant data supporting the findings of this study are available in this manuscript and in the supporting information file. Source data and associated measurements are provided with this manuscript. Data shown in this manuscript are available from the corresponding author with a reasonable request.

Acknowledgment

We would like to thank the University of Toledo Department of Laboratory Animal Resources (DLAR) and Drs. Heather Conti and Fan Dong at the University of Toledo for rat and house mouse samples. Testis sections were made by Allen Schroering, University of Toledo Medical Center (UTMC), Ohio. FAM161A N-terminus antibody was obtained from Dr. Dror Sharon, Hadassah-Hebrew University Medical Center. POC5 antibody was gifted by Dr. Michel Bornens. Plasmids for yeast two-hybrid analyses were obtained from Dr. Scott Crawley, University of Toledo, Ohio. We thank Dr. Bo Harstine at Select Sires, Inc. for donating bovine (Holstein) spermatozoa straws. We thank Dr. Kristin Kirshenbaum and the NSM Instrumentation Center at the University of Toledo for use of the STORM microscope. We thank Professor Geoff Parker (University of Liverpool) for commenting on the paper.

Funding

This project was supported by Agriculture and Food Research Initiative Competitive Grant no. OHOW-2020-02790 from the USDA National Institute of Food and Agriculture.

Competing Interest

The authors have declared no competing interest.

Contributors

SK	Led the project and extensively edited the paper.
NP	Performed RT PCR studies and extensively edited the paper.
RC	Performed the molecular phylogeny analysis, draft edit
KYA	Assisted with molecular biology.
MN	Assisted with domain analysis.
KT	Performed initial experiments with rabbits, draft edit.
EB	Assisted with western blots
AR	Assisted with STORM
JB	Provided access to *Microtus ochrogaster* sperm and testes.
SHC	Provided access to dog sperm.
HSF	Provided access to *Peromyscus* sperm and testes.
PS	Provided access to human sperm and testes.
JG	RNA-seq analysis.
RNB	Oversaw molecular phylogeny analysis, draft edit.
TAR	Led the project and wrote the first draft.

Supplementary Figures and Legends

SFig 1 – Spermatozoa with one canonical centriole (the proximal centriole) and one atypical centriole (the distal centriole) are present throughout the mammalian tree of life

A) Example of paddle/eyedrop-shaped sperm head with a centrally inserted neck, barrel-shaped proximal centriole (PC, canonical centriole), and funnel-shaped distal centriole (DC, atypical centriole), as in human, and a sickle-shaped sperm head with a laterally attached neck and no centrioles, as in house mice. Based on Knobil and Neill's Physiology of Reproduction (Plant and Zeleznik, 2014). **B**) A systematic survey of previous transmission electron microscopic studies of rodent spermatozoan centrioles.

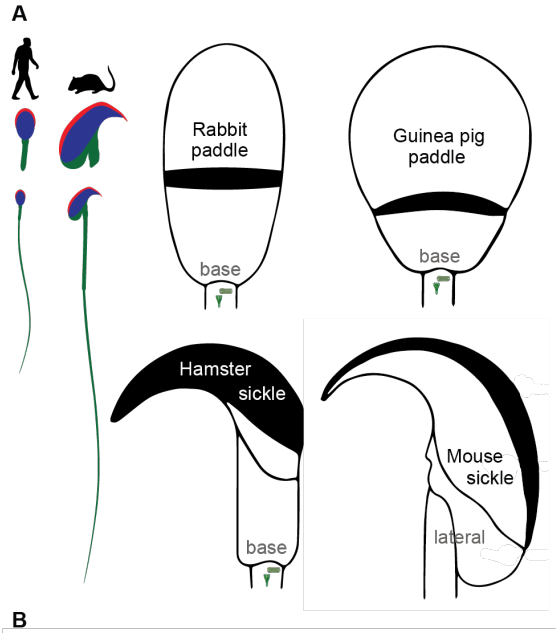

B

Bi) Eutherian: The four main groups of Eutherian mammalian species (color-coded) have one canonical centriole (the PC) in their spermatozoa. Phylogeny based on (Song et al., 2012).

Phylogeny: Boreoeutheria; Euarchontoglires (Superorder) - Order: Primates
- African green monkey (*Cercopithecus aethiops*) (Bedford, 1967)
- *Homo sapiens* (Pedersen, 1969) (Garanina et al., 2019)

Phylogeny: Boreoeutheria; Euarchontoglires (Superorder); Glires Order: Rodentia
- Siberian chipmunk (*Tamias sibiricus*) (Lee and Park, 2011)
- Chinchilla (Healey and Weir, 1970)
- Guinea Pig (Caviidae) (Fawcett, 1965)

Phylogeny: Boreoeutheria; Laurasiatheria (Superorder) - Order: Carnivora
- Cat (Schmehl and Graham, 1989) (Sato and Oura, 1984)

Phylogeny: Boreoeutheria; Laurasiatheria (Superorder) - Order: Chiroptera
- Bat (Bernard and Hodgson, 1988)

Phylogeny: Boreoeutheria; Laurasiatheria (Superorder) - Order: Eulipotyphla
- Lesser white-toothed shrew (*Crocidura suaveolens*) (Soon-Jeong et al., 2006)

Phylogeny: Boreoeutheria; Laurasiatheria (Superorder) - Order: Artiodactyla
- Boar (Nicander and Bane, 1962)
- Bovine (Ounjai et al., 2012)
- Camel (Tingari, 1991)

Phylogeny: Boreoeutheria; Laurasiatheria (Superorder) - Order: Perissodactyla
- Horse (Leung et al., 2021)

Phylogeny: Afrotheria; Order: Proboscidea
- Asiatic elephant (*Elephas maximus*) (Heath et al., 1983)

Phylogeny: Afrotheria Order: Macroscelidea
- Macroscelidea (elephant shrews) (Woodall and FitzGibbon, 1995)

Phylogeny: Xenarthra
- Six-banded armadillo (*Euphractus sexcinctus*) (Sousa et al., 2013)

Bii) Monotreme: The structure of the sperm neck is simpler in Monotreme Mammals than in Eutherian Mammals: While a PC is found near the nucleus, and the mitochondria reach the nucleus, neither striated columns nor a canonical DC are observed (Carrick and Hughes, 1982).

Biii) Marsupial: In Marsupials, the DC is not observed or persists in a modified form (Lloyd et al., 2002; Temple-Smith, 1994). The PC (aka transverse centriole) is observed in some species (Lloyd et al., 2002), having been reported in the mature spermatozoa of *Perameles nasuta*, *Macrotis lagotis*, several dasyurids, the petaurid genus Petaurus, and the peramelid *Isoodon macrourus* ((Sapsford et al., 1969) and (Johnston et al., 1995) in (Lloyd et al., 2002)). A remnant PC is present in *Hypsiprymnodon moschatus* (Lloyd et al., 2002). No PC is detected in *Trichosurus vulpecula* and most macropods ((Harding, 1979) in (Lloyd et al., 2002)).

SFig 1B References:

Bedford, J.M. 1967. Observations on the fine structure of spermatozoa of the bush baby (Galago senegalensis), the African green monkey (Cercopithecus aethiops) and man. *The American journal of anatomy*. 121:443-459.

Bernard, R.T., and A.N. Hodgson. 1988. Fine structure of the neck of epididymal spermatozoa of Schreiber's long-fingered bat (Chiroptera: Mammalia). *Gamete Res*. 21:41-50.

Carrick, F.N., and R.L. Hughes. 1982. Aspects of the Structure and Development of Monotreme Spermatozoa and Their Relevance to the Evolution of Mammalian Sperm Morphology. *Cell and Tissue Research*. 222:127-141.

Fawcett, D.W. 1965. The anatomy of the mammalian spermatozoon with particular reference to the guinea pig. *Z Zellforsch Mikrosk Anat*. 67:279-296.

Garanina, A.S., I.B. Alieva, E.E. Bragina, E. Blanchard, B. Arbeille, F. Guerif, S. Uzbekova, and R.E. Uzbekov. 2019. The Centriolar Adjunct(-)Appearance and Disassembly in Spermiogenesis and the Potential Impact on Fertility. *Cells*. 8:180.

Harding, H.R. 1979. Reproduction in male marsupials. A critique with additional observation on sperm development and structure, Elibrary..

Healey, P., and B.J. Weir. 1970. Changes in the ultrastructure of chinchilla spermatozoa in different diluents. *J Reprod Fertil*. 21:191-193.

Heath, E., R. Jeyendran, and E. Graham. 1983. Ultrastructure of Spermatozoa of the Asiatic Elephnat (Elephas maximus). *Anatomia, Histologia, Embryologia*. 12:245-252.

Johnston, S., L. Daddow, and F. Carrick. 1995. Ultrastructural and light microscopic observations of mature epididymal spermatozoa and sperm maturation of the greater bilby Macrotis lagotis (Metatheria, Mammalia). *Advances in Spermatozoal Phylogeny and Taxonomy*. 166:397-407.

Lee, J.-H., and K.-R. Park. 2011. Fine Structure of Sperm in the Korea Squirrel, Tamias sibiricus. *Applied Microscopy*. 41:99-107.

Leung, M.R., M.C. Roelofs, R.T. Ravi, P. Maitan, H. Henning, M. Zhang, E.G. Bromfield, S.C. Howes, B.M. Gadella, H. Bloomfield-Gadelha, and T. Zeev-Ben-Mordehai. 2021. The multi-scale architecture of mammalian sperm flagella and implications for ciliary motility. *EMBO J*. 40:e107410.

Lloyd, S., F. Carrick, and L. Hall. 2002. Ultrastructure of the mature spermatozoon of the musky rat-kangaroo, Hypsiprymnodon moschatus (Potoroidae: Marsupialia). *Acta Zoologica*. 83:167-174.

Nicander, L., and A. Bane. 1962. Fine structure of boar spermatozoa. *Z Zellforsch Mikrosk Anat*. 57:390-405.

Ounjai, P., K.D. Kim, P.V. Lishko, and K.H. Downing. 2012. Three-dimensional structure of the bovine sperm connecting piece revealed by electron cryotomography. *Biology of reproduction*. 87:73.

Pedersen, H. 1969. Ultrastructure of the ejaculated human sperm. *Z Zellforsch Mikrosk Anat*. 94:542-554.

Sapsford, C., C.A. Rae, and K. Cleland. 1969. Ultrastructual studies on maturing spermatids and on sertoli cells in the bandicoot Perameles nasuts Geoffroy (Marsupialia). *Australian Journal of Zoology*. 17:195-292.

Sato, N., and C. Oura. 1984. The fine structure of the neck region of cat spermatozoa. *Okajimas folia anatomica Japonica*. 61:267-285.

Schmehl, M., and E. Graham. 1989. Ultrastructure of the domestic tom cat (Felisdomestica) and tiger (Pantheratigrisaltaica) spermatozoa. *Theriogenology*. 31:861-874.

Song, S., L. Liu, S.V. Edwards, and S.Y. Wu. 2012. Resolving conflict in eutherian mammal phylogeny using phylogenomics and the multispecies coalescent model. *Proceedings of the National Academy of Sciences of the United States of America*. 109:14942-14947.

Soon-Jeong, J., P. Joo-Cheol, K. Heung-Joong, S.B. Chun, Y. Myung-Hee, L. Do-Seon, and J. Moon-Jin. 2006. Comparative fine structure of the epididymal spermatozoa from three Korean shrews with considerations on their phylogenetic relationships. *Biocell*. 30:279-286.

Sousa, P.C., E.A. Santos, J.A. Bezerra, G.L. Lima, T.S. Castelo, J.D. Fontenele-Neto, and A.R. Silva. 2013. Morphology, morphometry and ultrastructure of captive six-banded armadillo (Euphractus sexcinctus) sperm. *Animal reproduction science*. 140:279-285.

Temple-Smith, P.D. 1994. Comparative structure and function of marsupial spermatozoa. *Reprod Fertil Dev*. 6:421-435.

Tingari, M. 1991. Studies on camel semen. III. Ultrastructure of the spermatozoon. *Animal reproduction science*. 26:333-344.

Woodall, P.F., and C. FitzGibbon. 1995. Ultrastructure of Spermatozoa of the Yellow-rumped Elephant Shrew Rhynchocyon chrysopygus (Mammalia: Macroscelidea) and the Phylogeny of Elephant Shrews. *Acta Zoologica*. 76:19-23.

1110 **STable 2-1 –** Identity Ratio range of sperm centrosomal proteins

1111 This table is a large data set. See supplementary file**.**

1112

1113

1114

1115

1116 **STable 2-2 –** In rodents, natural selective pressure on FAM161A is stronger than that on other rod proteins and is
1117 strongest in Muridae.

1118

Gene	*FAM161A* (Muridae)	*FAM161A* (Cricetidae)	*FAM161A* (Other Myomorpha)	*FAM161A* (Rodents)	*FAM161B* (Rodents)	*POC1b* (Rodents)	*POC5* (Rodents)	*CETN1* (Rodents)	*WDR90* (Rodents)
ω (dN/dS)	0.62960	0.57030	0.48616	0.57592	0.33602	0.19055	0.26702	0.03423	0.26510

1119
1120

STable 2-3 – Codon-wide selection analysis to identify sites under positive selection

Selection analysis identified more positively (Green font) and negatively (red font) selected sites in rodents than in primates, carnivora, and ungulates. The number of codons used in each lineage is indicated in parentheses**.** The number of selected sites and the site numbers along the primary structure are indicated for each method and mammalian order. MEME (Murrell et al., 2012) is a generalization of FEL (Kosakovsky Pond and Frost, 2005). The initial analytical phases of the two approaches are identical; however, FEL assumes that the same dN/dS (ω) ratio applies to all branches, while MEME models variable dN/dS (ω) values across lineages at an individual site.

Selection Analysis	**Ungulates** 722 codons	**Carnivore** 722 codons	**Primates** 716 codons	**Rodents** 714 codons
MEME: Episodic Diversifying Selection (P< 0.05)	**9 Sites**: 46, 47, 49, 60, 62, 67, 84, 312, 440, 505	**7 sites**: (35, 49, 60, 65, 451, 476, 518, 688	**10 Sites**: 44, 53, 136, 186, 268, 302, 348, 633, 634, 695	**53 Sites**: 5, 10, 11, 15, 18, 22, 23, 44, 56, 59, 60, 61, 62, 65, 67, 68, 71, 113, 134, 135, 174, 177, 230, 237, 254, 325,378, 422, 427, 442, 451, 453, 467, 479, 633, 634, 635, 636, 639, 657, 680, 682, 687, 690, 713
FEL: Pervasive Diversifying Selection (P< 0.05)	**0 Sites**	**2 Sites**: (27, 65)	**2 Sites:** 54, 268	**14 Sites:**10, 22, 23, 62, 67, 230, 363, 392, 427, 442, 451, 473, 512, 656
PAML (M8 BEB, No *= PP=90, *PP >95, **PP>95)	**5 Sites:** 13L, 46L, 61A, 61R*, 511A*	**17 Sites:** 5H, 17T, 27V, 35P, 36L*, 65R*, 85G, 172C*, 219Q, 315Y*, 420G, 429C, 450H, 476T*, 498Y*, 589M*, 603Q*	**6 Sites:** 38A, 171V, 213R*, 306R, 391H*, 406C**)	**42 Sites:** 4P, 22 I**, 45A, 46A**, 48M, 52E**, 53Q**, 55K, 56V, 65G*, 67H*, 71G*, 78F, 81T, 129F, 130I, 152L*, 184T*, 192V, 213*, 221A, 230S, 264*, 270R*, 288S, 289C*, 345F, 399S, 403C**, 405R*, 406F, 438W**, 442P*, 448F*, 451C*, 455C*,467S, 473L*, 496R*, 511E*, 512C*, 656F
FEL: Purifying Selection (P< 0.05)	**34 sites:** 3, 50, 51, 54, 55, 56, 107, 135, 146, 159, 166, 232, 235, 277, 291, 294, 295, 298, 310, 323, 330, 331, 359, 361, 371, 390, 463, 465, 523, 526, 530, 567, 583, 603	**38 Sites** 37,38,45,78,91,130,159,163,182,203,204,212,149,252,264,273,280,292,296,328,330,373,398,402,412,436,447,461,469,479,522,526,530,535,555,617,634,714	**37 Sites** 8,12,34,35,58,62,71,76,83,94,153,160,178,198,208,211,239,246,262,273,326,331,369,404,412,444,452,453,486,517,558,564,585,586,637,659,664	**100 Sites:** 2, 8, 9, 51, 86, 90, 93, 97, 98, 101, 103, 105, 111, 121, 138, 140, 143, 155, 156, 158, 165, 170, 185, 194, 198, 205,210,236,240,241,244,245,246,258,274,285,287,292,293,295,300,303,304,305, 306,318,321,323,324,326,327,329,330,331,335,337,338,357,358,371,379,389,425, 464,484,499,514,518,522,523,534,525,541,548,569,570,575,591,595,598,605,606, 610,611,612,615,616,620,622,624,625,626,637,638,654,665,674,679,695,707
FUBAR: Pervasive Purifying Selection (P< 90)	**28 Sites:** 3, 50, 51, 54, 55, 56, 60, 107, 135, 146, 159, 166, 232, 235, 277, 294, 310, 325, 330, 359, 390, 465, 523, 526, 530, 567, 583, 603	**31 Sites:** 37, 38, 45, 78, 91, 130, 159, 182, 203, 212, 253, 264, 273, 292, 296, 328, 330, 398, 412, 447, 461, 469, 479, 522, 526, 530, 535, 555, 617, 634	**19 Sites:** 34, 58, 62, 76, 178, 208, 239, 262, 273, 326, 404, 412, 444, 452, 486, 517, 586, 659, 664	**107 Sites:** 1, 2, 9, 86, 90, 93, 94, 98, 101, 103, 105, 109, 115, 138, 140, 143, 155, 156, 158, 165, 170, 185, 194, 198, 201, 205, 209, 210, 236, 238, 240, 241, 243, 244, 246, 258, 274, 276, 280, 281, 282, 283, 285, 287, 293, 295, 304, 306, 318, 323, 324, 326, 329, 330, 331, 335, 337, 338, 354, 356, 358, 364, 371, 465, 470, 481, 514, 518, 523, 524, 525, 527, 533, 537, 548, 563, 565, 570, 575, 585, 591, 592, 595, 598, 605, 606, 610, 612, 613, 614, 615, 616, 620, 621, 622, 624, 625, 626, 637, 638, 650, 663, 665, 674, 693, 695, 707

1130 **STable 2-4 –** Number of negatively selected (NSS) and positively selected (PSS) sites with P<0.05 using FEL and
1131 FUBAR analysis.
1132

		Muridae	Cricetidae	Other rodents
FEL (P<0.05)	Negatively selected sites (NSS)	4	87	48
	Positively selected sites (PSS)	14	14	15
FUBAR (PP >90)	Negatively selected sites (NSS)	7	14	28
	Positively selected sites (PSS)	0	3	0

1133
1134

1135 **SFig 3-1 – House mice express a Type 3 (555-aa) FAM161A isoform in the testes**

1136 **A**) Various annotated FAM161A isoforms found in house mouse testes, based on transcriptome sequencing performed
1137 by (Green et al., 2018). **B–C**) FAM161A isoform types 1–3 with exons numbered and approximate locations of forward,
1138 reverse (filled, colored triangles), and sequencing primers (open, colored triangles) chosen for PCR with reverse-
1139 transcribed mRNA isolated from either house mouse testis or eye tissue (**B**); and electrophoresis gel with expected
1140 sizes (in base pairs) of bands produced using the indicated primers (**C**). -, no band was expected for that reaction. A
1141 cDNA library was constructed using a 3' RACE kit (Roche). The First PCR was performed using the cDNA library, the
1142 product of which was used to perform the Second PCR. Sequencing was performed on the Second PCR product
1143 following gel extraction. MW, molecular weight. **D**) The NCBI house mouse testis EST database showed that eight
1144 FAM161A transcripts have the unique, C-terminus sequence characteristic of type 3.

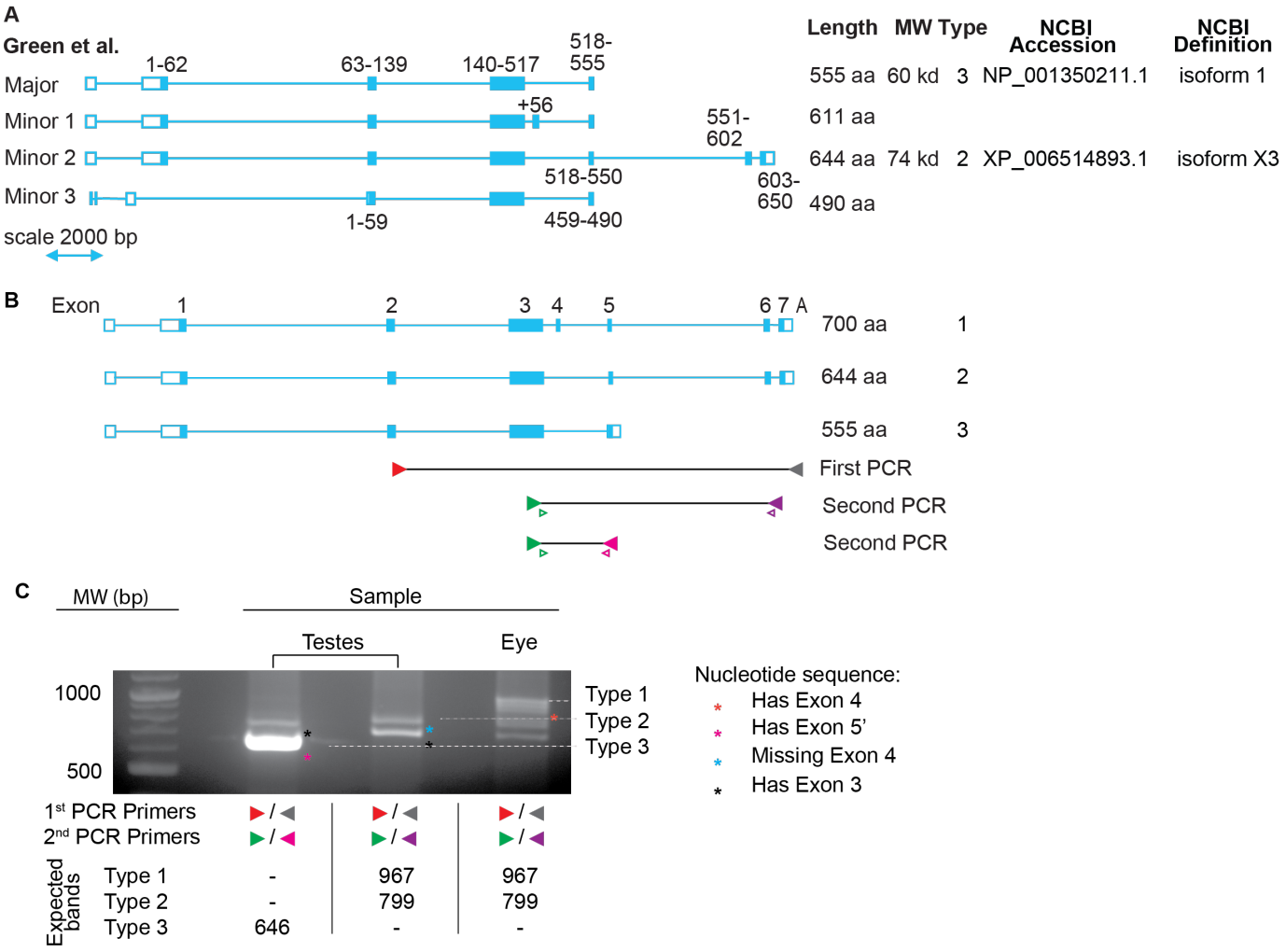

D The NCBI mouse testis EST database shows that eight FAM161A transcripts have the unique, C-terminus sequence characteristic of type 3:

1145 AV283297.2, AI613936.1, AV262776.1, AA492939.1, BB015036.1, AV257583.1, AV283863.1, AA064510.1.
1146

SFig 4-1 – The mechanism of rod protein interaction

A) Expression of human FAM161A (hFAM161A) type 2, human POC1B (hPOC1B), and human POC5 (hPOC5) and their colocalization with tubulin in U2OS cells. **B**) Expression of various fragments of hFAM161A type 2 with full-length hPOC1B and quantification of FAM161A colocalization with hPOC1B. **C**) Expression of various fragments of hFAM161A type 2 with hPOC5 and quantification of FAM161A colocalization with hPOC5. Scale bars are 10 µm. **D**) Yeast two-hybrid analysis to map the hPOC5-interacting domain of hFAM161A. BD, binding domain; AD, activation domain; DDO, double dropout (-Leu, -Trp); TDO, triple dropout (-Leu, -Trp, -His); QDO, quadruple dropout (-Leu, -Trp, -His, -Ade). **E**) Yeast two-hybrid analysis to map the domain mediating the interaction between hPOC1B and hPOC5. **F**) Model depicting the mechanism of interaction between rod proteins. WD, WD40 repeat domains; CBR, centrin binding region; EF-hand, a calcium-binding motif. CC, coiled coil domain.

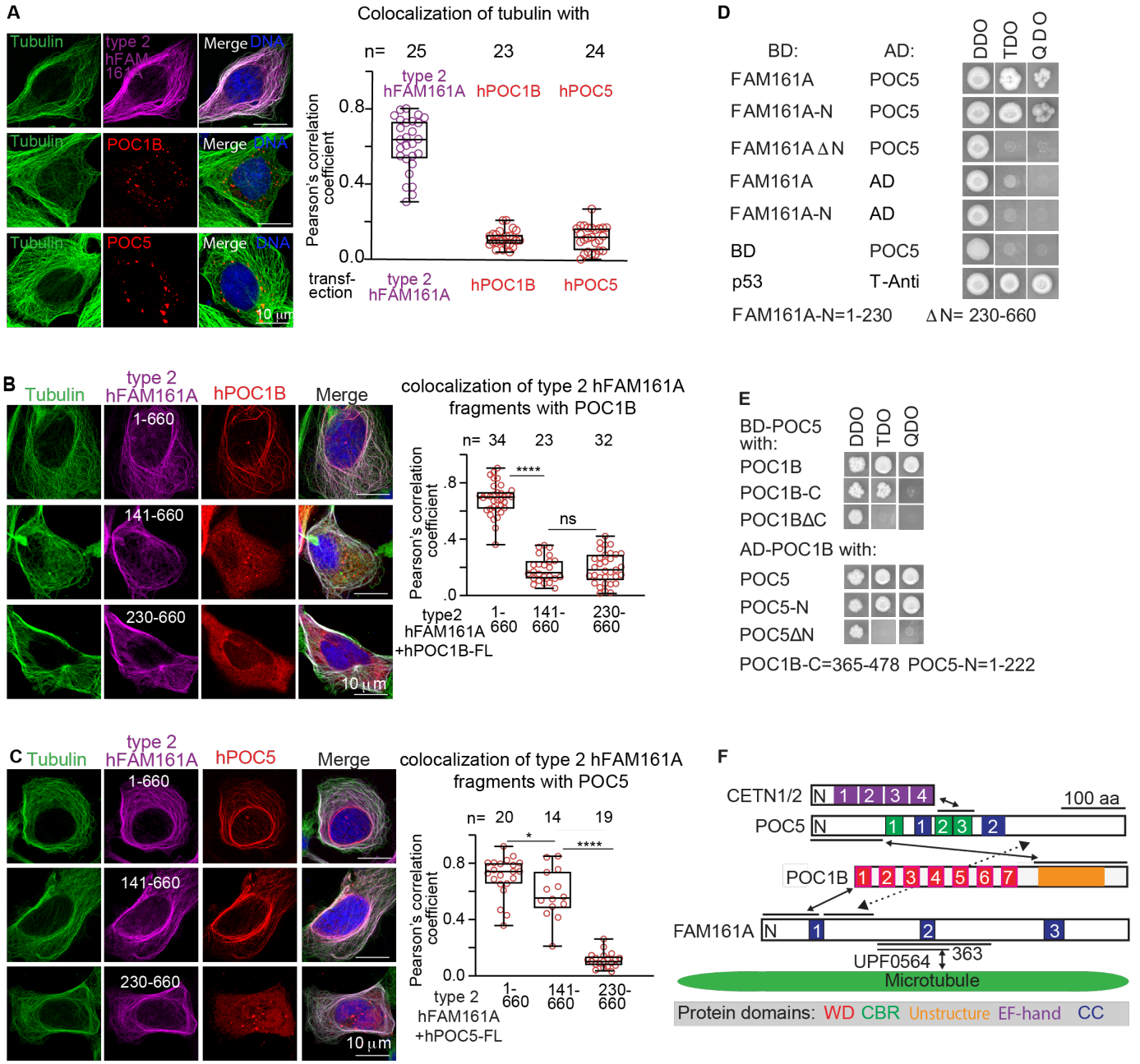

SFig 4-2 – FAM161A sequence alignment

```
Hs1     MATSHRVAKLVASSLQTPVNPITGARVAQYEREDPLKALAAAEAILEDEEEE--KVAQPA 58
Hs2     MATSHRVAKLVASSLQTPVNPITGARVAQYEREDPLKALAAAEAILEDEEEE--KVAQPA 58
Mm1     MASPHQEARLAAASLLLSANPITGARVAQYESEDSLESLVAAGLAAAMEEEEQKKVWQMR 60
Mm2     MASPHQEARLAAASLLLSANPITGARVAQYESEDSLESLVAAGLAAAMEEEEQKKVWQMR 60
Mm3     MASPHQEARLAAASLLLSANPITGARVAQYESEDSLESLVAAGLAAAMEEEEQKKVWQMR 60
        **: *: *:*.*:**   .************ ** *::*.**       :**::** *

Hs1     GASADLNTSFSGVDEHAPISYEDFVNFPDIHHSNEEYFKKVEELKAAHIETMAKLEKMYQ 118
Hs2     GASADLNTSFSGVDEHAPISYEDFVNFPDIHHSNEEYFKKVEELKAAHIETMAKLEKMYQ 118
Mm1     -ASAGCH-NFSGKDE--EVAFESTMNFSDIYHSDEEYFRKLKDLKAVHEETMSKLEKMYQ 116
Mm2     -ASAGCH-NFSGKDE--EVAFESTMNFSDIYHSDEEYFRKLKDLKAVHEETMSKLEKMYQ 116
Mm3     -ASAGCH-NFSGKDE--EVAFESTMNFSDIYHSDEEYFRKLKDLKAVHEETMSKLEKMYQ 116
        .  :    .*** **   :::*. :** **:**:****:*:::***.* ***:*******

Hs1     DKLHLKEVQPVVIREDSLSDSSRSVSEKNSYHPVSLMTSFSEPDLGQSSSLYVSSSEEEL 178
Hs2     DKLHLKEVQPVVIREDSLSDSSRSVSEKNSYHPVSLMTSFSEPDLGQSSSLYVSSSEEEL 178
Mm1     DKLNIKDIQAGFIRDGISDSSSSSASEKSCSHPALSVTSLSEPDLDGSSSLST-TTDEGL 175
Mm2     DKLNIKDIQAGFIRDGISDSSSSSASEKSCSHPALSVTSLSEPDLDGSSSLST-TTDEGL 175
Mm3     DKLNIKDIQAGFIRDGISDSSSSSASEKSCSHPALSVTSLSEPDLDGSSSLST-TTDEGL 175
        ***::*::*  .**:.  ..** *.***.. **.  :**:*****. **** . :::* *

Hs1     PNLEKEYPRKNRMMTYAKELINNMWTDFCVEDYIRCKDTGFHAAEKRRKKRKEWVPTITV 238
Hs2     PNLEKEYPRKNRMMTYAKELINNMWTDFCVEDYIRCKDTGFHAAEKRRKKRKEWVPTITV 238
Mm1     PDLEEKTPGESSAMVHAQELINNMWNDFSVEDYIQYDSDS-RTAKKKRKKAKSLTPKITV 234
Mm2     PDLEEKTPGESSAMVHAQELINNMWNDFSVEDYIQYDSDS-RTAKKKRKKAKSLTPKITV 234
Mm3     PDLEEKTPGESSAMVHAQELINNMWNDFSVEDYIQYDSDS-RTAKKKRKKAKSLTPKITV 234
        *:**:: * :.  *.:*:*******.**.*****: .. . ::*:*:*** *. .*.***

Hs1     PEPFQMMIREQKKKEESMKSKSDIEMVHKALKKQEEDPEYKKKFRANPVPASVFLPLYHD 298
Hs2     PEPFQMMIREQKKKEESMKSKSDIEMVHKALKKQEEDPEYKKKFRANPVPASVFLPLYHD 298
Mm1     PVPFEMTVREQNRREKALSARSDLE--TKLLKRDEDDAECKKKFRANPVPSCVLLPLYED 292
Mm2     PVPFEMTVREQNRREKALSARSDLE--TKLLKRDEDDAECKKKFRANPVPSCVLLPLYED 292
Mm3     PVPFEMTVREQNRREKALSARSDLE--TKLLKRDEDDAECKKKFRANPVPSCVLLPLYED 292
        * **:* :***:::*:::.::**:*   * **::*:* * **********:.*:****.*

Hs1     LVKQKEERRRSLKEKSKEALLASQKPFKFIAREEQKRAAREKQLRDFLKYKKKTNRFKAR 358
Hs2     LVKQKEERRRSLKEKSKEALLASQKPFKFIAREEQKRAAREKQLRDFLKYKKKTNRFKAR 358
Mm1     LVKQSEERRKKARERNRAALLASLKPFKFIAREEQKQAVREKKLRDLFRAKRKTNQFKAK 352
Mm2     LVKQSEERRKKARERNRAALLASLKPFKFIAREEQKQAVREKKLRDLFRAKRKTNQFKAK 352
Mm3     LVKQSEERRKKARERNRAALLASLKPFKFIAREEQKQAVREKKLRDLFRAKRKTNQFKAK 352
        ****.****:. :*:.: ***** ************:*.***:***::: *:***:***:

Hs1     PIPRSTYGSTTNDKLKEEELYRNLRTQLRAQEHLQNSSPLPCRSACGCRNPRCPEQAVKL 418
Hs2     PIPRSTYGSTTNDKLKEEELYRNLRTQLRAQEHLQNSSPLPCRSACGCRNPRCPEQAVKL 418
Mm1     PVPRFIYRPAASDKPKEEELYGDSRMLPKVRDLL-QNSPWPSRSACR--RFRDPRSPAKP 409
Mm2     PVPRFIYRPAASDKPKEEELYGDSRMLPKVRDLL-QNSPWPSRSACR--RFRDPRSPAKP 409
Mm3     PVPRFIYRPAASDKPKEEELYGDSRMLPKVRDLL-QNSPWPSRSACR--RFRDPRSPAKP 409
        *:**  *  ::.** ****** : *   :.:: * :.** *.****   . * *.. .*

Hs1     KCKHKVRCPTPDFEDLPERYQKHLSEHKSPKLLTVCKPFDLHASPHASIKREKILADIEA 478
Hs2     KCKHKVRCPTPDFEDLPERYQKHLSEHKSPKLLTVCKPFDLHASPHASIKREKILADIEA 478
Mm1     RGKHRRRCLRRDG--DLEKWKEPFSEYSFLKCPMLCEECCLHESPCDSDKRQKLLADIRA 467
Mm2     RGKHRRRCLRRDG--DLEKWKEPFSEYSFLKCPMLCEECCLHESPCDSDKRQKLLADIRA 467
Mm3     RGKHRRRCLRRDG--DLEKWKEPFSEYSFLKCPMLCEECCLHESPCDSDKRQKLLADIRA 467
        : **: **   *     *:::: :**:.  *   :*:   ** **  * **:*:****.*

Hs1     DEENLKETRWPYLSPRRKSPVRCAGVNPVPCNCNPPVPTVSSRGREQAVRRSLEEKKMLE 538
Hs2     DEENLKETRWPYLSPRRKSPVRCAGVNPVPCNCNPPVPTVSSRGREQAVR---------- 528
Mm1     DEEILRETRRPGRSPRRKSPGRSSNPKPRPHECSPPMPTASSRGREQAIRKSLEEKKMLE 527
Mm2     DEEILRETRRPGRSPRRKSPGRSSNPKPRPHECSPPMPTASSRGREQAIR---------- 517
Mm3     DEEILRETRRPGRSPRRKSPGRSSNPKPRPHECSPPMPTASSRGREQAIR---------- 517
        *** *:*** *  ******* *.:. :* * :*.**:**.********:*

Hs1     EERNRILTKQKQRMKELQKLLTTRAKAYDSHQSLAQISKSRVKCLRKSEKERMREYQREL 598
Hs2     ----------------------------------------------KSEKERMREYQREI 542
Mm1     EERNRILTKQKQRMKDLQKLLATRVKAYGSHQSLSQIVKARVKELRRSEKARMREYWQEL 587
Mm2     ----------------------------------------------RSEKARMREYWQEL 531
Mm3     ----------------------------------------------RSEKARMREYWQEL 531
                                                      :*** ***** :**

Hs1     EEREEKLKKRPLLFERVAQKNARMAAEKHYSNTLKALGISDEFVSKKGQSGKVLEYFNNQ 658
Hs2     EEREEKLKKRPLLFERVAQKNARMAAEKHYSNTLKALGISDEFVSKKGQSGKVLEYFNNQ 602
Mm1     EEQEEKLQKRPMLFERVTQRNARMAAERCYSNTLKALGLLEEFVSEKGQSGKVSEDFTRQ 647
Mm2     EEQEEKLQKRPMLFERVTQRNARMAAERCYSNTLKALGLLEEFVSEKGQSGKVSEDFTRQ 591
Mm3     EEQEEKLQKRPMLFERVTQVVFIG----------------------------------- 555
        **:****:***:*****:*

Hs1     ETKSVTEDKESFNEEEKIEERENGEENYFIDTNSQDSYKEKDEANEES--EEEKSVEESH 716
Hs2     ETKSVTEDKESFNEEEKIEERENGEENYFIDTNSQDSYKEKDEANEES--EEEKSVEESH 660
Mm1     ELRSCTLEKESSYG----EERENEEESYLTDISSQDSCKGNKEDIKDIKSGEENSGE--- 700
Mm2     ELRSCTLEKESSYG----EERENEEESYLTDISSQDSCKGNKEDIKDIKSGEENSGE--- 644
Mm3     ------------------------------------------------------------ 555
```

POC1B Binding segment

POC5 Binding segment

dimerization domain

UPF0564

Exon 4

Type 3 unique sequence

SFig 4-3 – House mouse FAM161A type 3 inhibits type 2 from recruiting POC1B to the microtubules

A–C) Expression of human POC1B (hPOC1B) with house mouse FAM161A (mFAM161A) type 2 (**A**), mFAM161A type 3 (**B**), and both mFAM161A types 2 & 3 (**C**). Only one FAM161A isoform at a time is shown in panel C; however, the cells were transfected with all three proteins (i.e., hPOC1B and mFAM161A types 2 & 3). Scale bars are 8 um **D**) Quantification of hPOC1B colocalization with tubulin under various transfection conditions. **E**) mFAM161A type 3 and hPOC1B colocalize in extranuclear foci. Shown in inset. ****p<0.0001. n, number of cells. Scale bars are 5 µm.

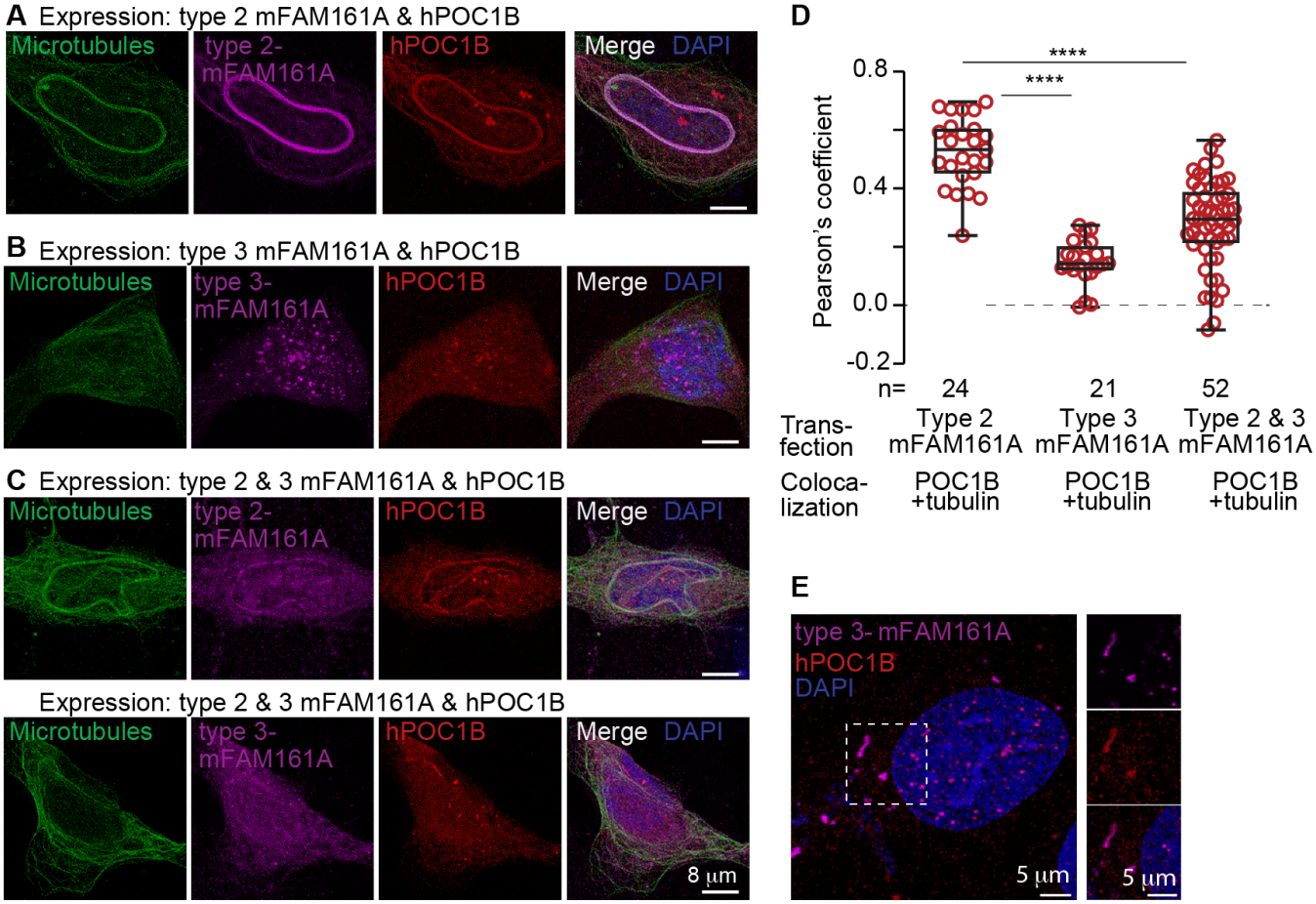

SFig 5 – FAM161A labels the proximal and distal centrioles of dog spermatozoa

Confocal microscopy of the dog distal centriole showed that FAM161A exhibits prominent left- and right-side labeling, suggesting that the distal centriolar rods are far away from each other. PC, proximal centriole; DC, distal centriole; Ax, axoneme. Scale bars are 1 µm.

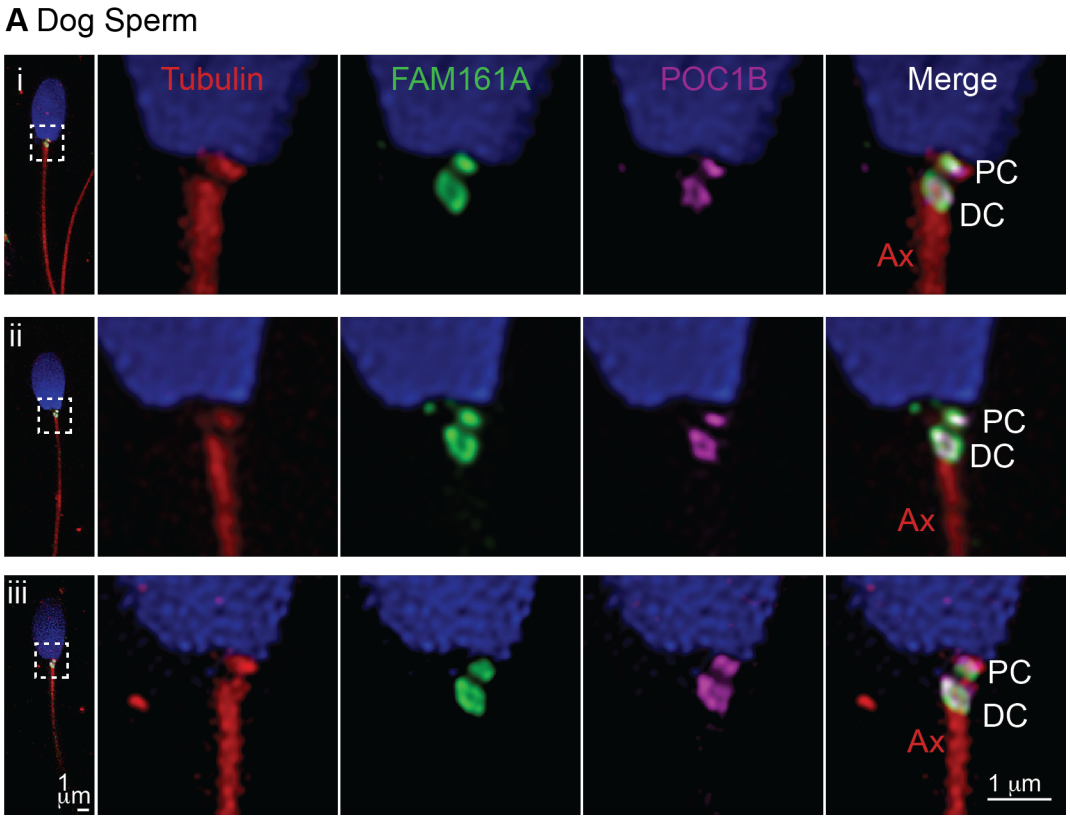

Sfig 6-1 – The bovine distal centriole begins splaying in round spermatids and splits in elongated spermatids

A) 3D-STORM imaging of bovine testes with rod protein staining during spermatogenesis. **B**) Centriolar length in spermatogonia/spermatocytes (Sg), round spermatids (RS), and elongated spermatids (ES). The C1/2 panel includes both C1 and C2. **C**) Proximal and distal centriolar width at their caudal (aka tip) and rostral (aka base) ends in round spermatids. C1/2, centrioles 1 and 2; PC, proximal centriole; DC, distal centriole. **D**) Distal centriolar rod length and width measurements based on POC5 staining in elongated spermatids. All data shown was accumulated over three independent experiments. Data B and C are plotted as box and whisker with interquartile range. Data shown in D is an average ± SD. ****p<0.0001, ***p<0.001, **p<0.01, *p<0.05; ns, not significant.

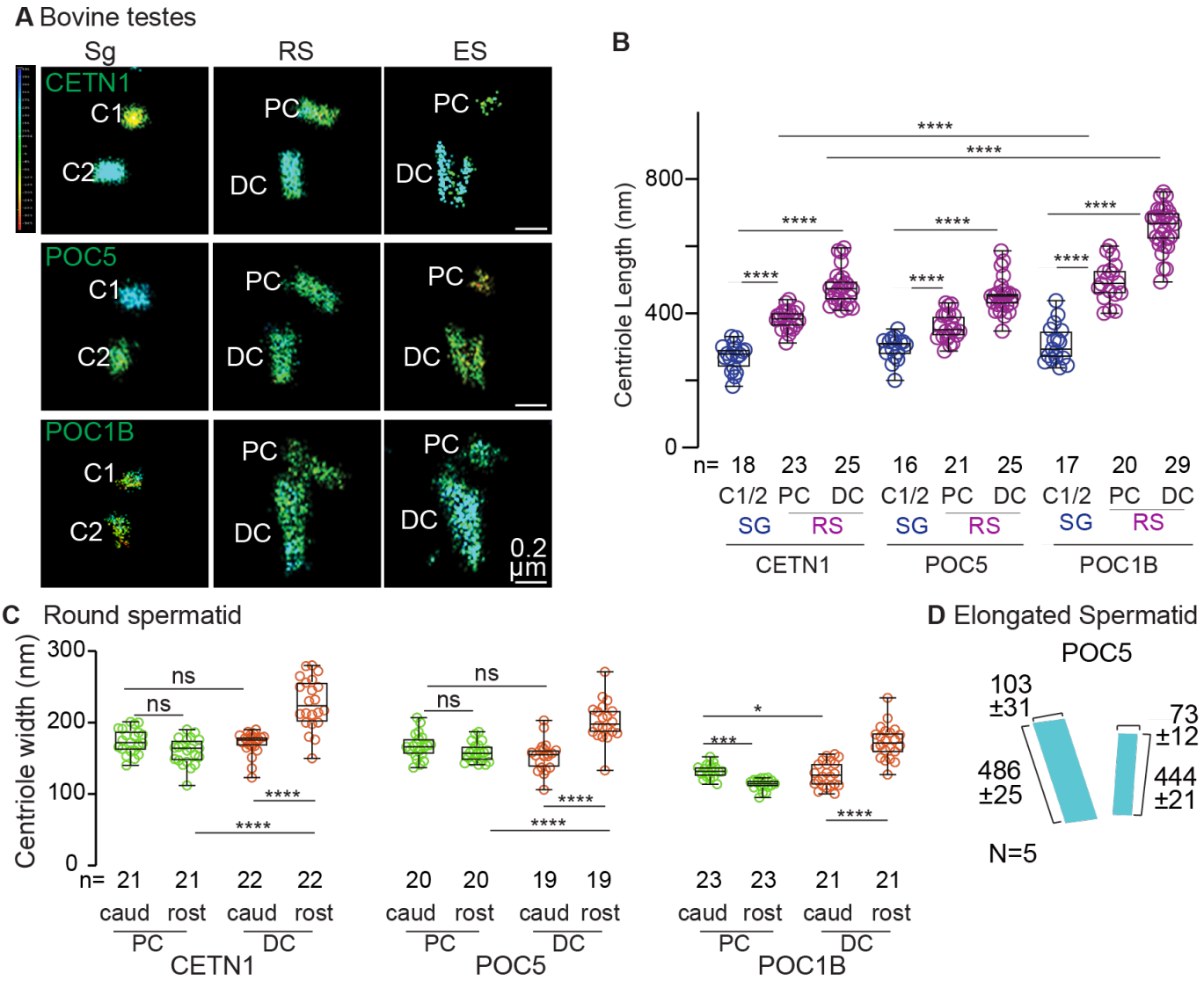

1186 **SFig 6-2 – Centriole remodeling generates species-specific centriolar sizes**

1187 Quantification of centriolar length based on CETN1 labeling in bovine (Bt), rabbit (Oc), and human (Hs) testes at
1188 spermatogonia/spermatocyte (Sg) and round spermatid (RS) cell stages. C1/2, centriole 1/2; PC, proximal centriole;
1189 DC, distal centriole. ****P<0.0001, **P<0.01; ns, not significant.

1190

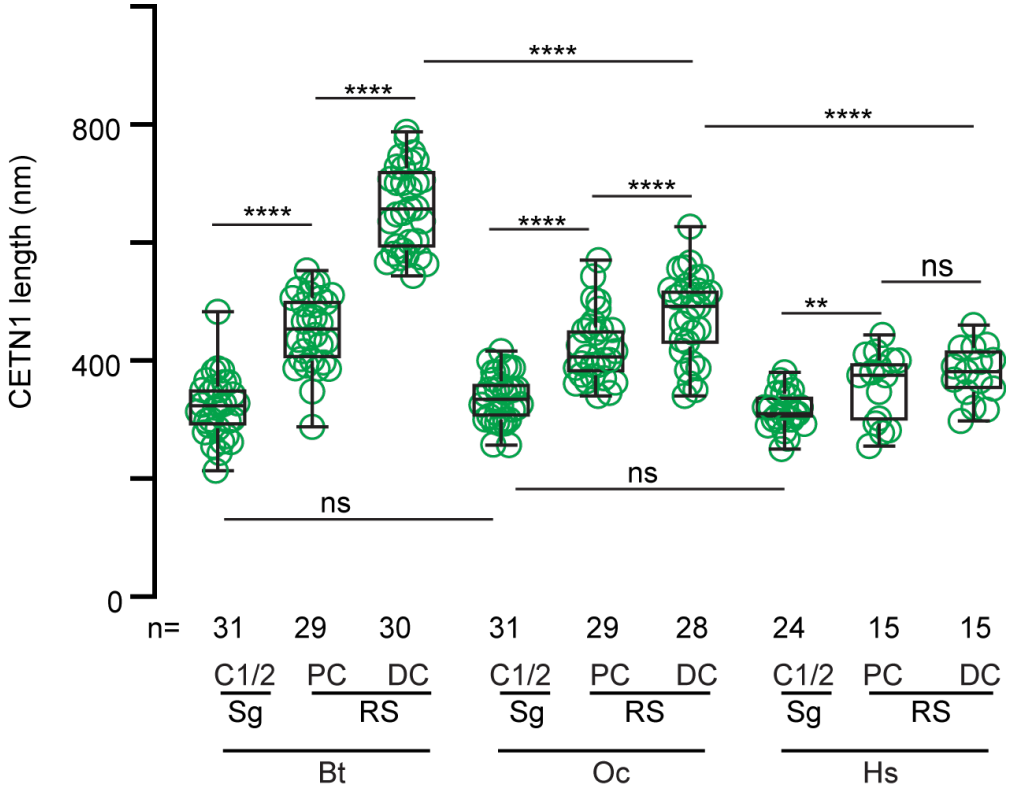

1191
1192

1193 **SFig 7-1 – FAM161A N-terminus Ab labeling in mouse testes**

1194 Immunostaining using FAM161A N-terminus antibody and by POC1B ab1 and ab2 in house mouse round spermatids
1195 (RS), PC, proximal centriole; DC, distal centriole. Scale bars are 1 µm.

1196

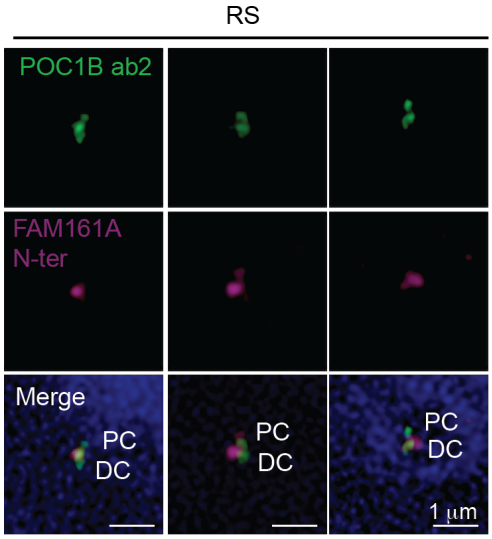

1197
1198

1199 **STable 8-1 – Antibodies used in this study**

1200

Antibody (Production animal)	Company (Catalog number)	Concentration (Application)
POC5 ab1 (Rabbit)	Gifted by Dr. Bernan (PMID #19349582)	1:200 (Confocal) 1:100 (STORM)
POC5 ab2 (Rabbit)	Thermo Fisher Scientific (PA5-24308)	1:200 (Confocal) 1:100 (STORM)
CETN1 (Mouse)	Santa Cruz (2A6)	1:10 (Confocal) 1:5 (STORM)
POC1B ab1 (Rabbit)	Thermo Fisher Scientific (PA5-24495)	1:300 (Confocal)
POC1B ab2 (Mouse)	Thermo Fisher Scientific (H00282809-B01P)	1:300 (Confocal) 1:100 (STORM)
FAM161A ab1 (Rabbit)	Sigma Aldrich (HPA032119)	1:300 (Confocal)
FAM161A ab2 (Rabbit)	Novus Biologicals (NBP1-91508)	1:1000 (Western)
FAM161A N-terminus (Rabbit)	Gifted by Dr. Dror Sharon (Hadassah-Hebrew University Medical Center)	1:200 (Confocal)
Tubulin (Mouse)	DSHB (Developmental Studies Hybridoma Bank) (E7)	1:20 (Supernatant) 1:100 (Concentrate)
Tubulin (Sheep)	Cytoskeleton, Inc. (ATN02)	1:500 (Confocal)
Anti-HA (Rabbit)	Invitrogen (SG77)	1:200 (Confocal) 1:1000 (Western)
Anti-FLAG (Mouse)	Invitrogen (FG4R)	1:400 (Confocal) 1:1000 (Western)
Anti-Rabbit A647 (Donkey)	Jackson ImmunoResearch (711-605-152)	1:300 (Confocal) 1:100 (STORM)
Anti-Mouse A647 (Donkey)	Jackson ImmunoResearch (715-605-150)	1:300 (Confocal) 1:100 (STORM)
Anti-Rabbit A488 (Donkey)	Jackson ImmunoResearch (711-545-152)	1:200 (Confocal)
Anti-Sheep A555 (Donkey)	Thermo Fisher Scientific (A-21436)	1:500 (Confocal)
Anti-Mouse A488 (Donkey)	Jackson ImmunoResearch (715-545-150)	1:200 (Confocal)
Anti-Sheep A488 (Donkey)	Jackson ImmunoResearch (715-545-003)	1:300 (Confocal)

1201

1202 **STable 8-2 – Primers used in this study**

Application	Primer	Sequence
3' RACE	Oligo d(T)-Anchor	5'-GACCACGCGTATCGATGTCGACTTTTTTTTTTTTTTTTV-3' *Mlu* | site *Cla* | site *Sal* | site, V = A, C, or G (what is that)
1st PCR	2FW	5'-CAGGAAACTCAAAGACCTGAAGG-3'
	PCR Anchor	5'-GACCACGCGTATCGATGTCGAC-3'
2nd PCR	3FW	5'-GCCAGCTGCGAGTGACAAGC-3'
	5RV	5'-CTGGAGGAACAAGAGGAAAAACTGC-3'
	5*RV	5'-GCCTCCACCTTTGTGCTCCGTC-3'
	7RV	5'-GAACCACAGCTGACACAAATGG-3'
Sequencing	Seq. 3FW	5'-GCAGACATCAGAGCAGATGAAG-3'
	Seq. 5RV	5'-GGAGTGAAAAGGCCAGGATGAG-3'
	Seq. 5*RV	5'-CCAGCTTTCTGTTTCTCAGTAC-3'
	Seq. 7RV	5'-GGAGAAGAAAGAGAGAATGAGG-3'

1203

1204 **STable 8-3 – Table Species Analyzed**

1205 Table 8-3a. List of rodent sequences analyzed

Organism	Length of amino acid sequence	Accession ID
Mus musculus house mouse	**700**	XM_006514828.5
Rattus norvegicus Norway rat	**653**	XM_017599131.2
Heterocephalus glaber naked mole-rat	**706**	XM_004867228.3
Nannospalax galili Upper Galilee mountains blind mole rat	**709**	XM_017800967.2
Mesocricetus auratus golden hamster	**695**	XM_005070431.4
Dipodomys ordii Ords kangaroo rat	**713**	XM_013022573.1
Castor canadensis American beaver	**701**	XM_020175016.1
Mus caroli Ryukyu mouse	**728**	XM_029483590.1
Mus pahari shrew mouse	**550**	XM_029545237.1
Peromyscus maniculatus bairdii prairie deer mouse	**699**	XM_006974797.2
Jaculus jaculus lesser Egyptian jerboa	**921**	XM_004665507.1
Meriones unguiculatus Mongolian gerbil	**699**	XM_021626659.1
Rattus rattus black rat	**471**	XM_032916924.1
Grammomys surdaster	**260**	XM_028778791.1
Mastomys coucha southern multimammate mouse	**495**	XM_031341979.1
Arvicanthis niloticus African grass rat	**641**	XM_034508367.1
Cricetulus griseus Chinese hamster	**703**	XM_003502153.5
Peromyscus leucopus white-footed mouse	**782**	XM_028876357.2
Onychomys torridus southern grasshopper mouse	**696**	XM_036201671.1
Arvicola amphibius Eurasian water vole	**704**	XM_038339639.1
Microtus oregoni creeping vole	**705**	XM_041669288.1
Microtus ochrogaster prairie vole	**706**	XM_026788902.1
Cavia porcellus domestic guinea pig	**686**	XM_013150060.2
Octodon degus degu	**702**	XM_023720875.1
Fukomys damarensis Damara mole-rat	**693**	XM_033762286.1
Marmota marmota marmota Alpine marmot	**551**	XM_015479628.1
Ictidomys tridecemlineatus thirteen-lined ground squirrel	**705**	XM_005322047.4
Urocitellus parryii Arctic ground squirrel	**705**	XM_026387235.1
Marmota flaviventris yellow-bellied marmot	**705**	XM_027934553.1

1206 Table 8-3b. List of carnivore sequences analyzed

Organism	Length of amino acid sequence	Accession ID
Canis lupus familiaris dog	716	XM_005626140.4
Mustela putorius furo domestic ferret	729	XM_004742028.2
Panthera tigris altaica Amur tiger	665	XM_007075417.1
Enhydra lutris kenyoni	720	XM_022504396.1
Acinonyx jubatus cheetah	715	XM_027072376.1
Lynx canadensis Canada lynx	715	XM_030310672.1
Puma yagouaroundi jaguarundi	715	XM_040463327.1
Puma concolor puma	714	XM_025932404.1
Felis catus domestic cat	715	XM_003984033.5
Panthera pardus leopard	715	XM_019431779.1
Canis lupus dingo dingo	716	XM_025468782.2
Ursus arctos horribilis	719	XM_026485066.1
Lontra canadensis Northern American river otter	721	XM_032873831.1
Mustela erminea ermine	729	XM_032353647.1
Odobenus rosmarus divergens Pacific walrus	719	XM_004397721.1
Hyaena hyaena striped hyena	705	XM_039240346.1
Suricata suricatta meerkat	706	XM_029937442.1
Vulpes lagopus Arctic fox		XM_041757534.1
Vulpes vulpes red fox	776	XM_025992735.1
Ursus maritimus polar bear	719	XM_040623440.1
Ailuropoda melanoleuca giant panda	720	XM_034659197.1
Eumetopias jubatus Steller sea lion	718	XM_028089669.1
Zalophus californianus California sea lion	718	XM_027624320.1
Neomonachus schauinslandi Hawaiian monk seal	721	XM_021699187.1
Halichoerus grypus gray seal	722	XM_036121192.1
Leptonychotes weddellii Weddell seal	722	XM_006733195.2
Mirounga leonina Southern elephant seal	720	XM_035001465.1
Phoca vitulina harbor seal	722	XM_032410896.1

1207
1208

1209
1210 Table 8-3c. List of ungulated sequences analyzed.

Organism	Length of amino acid sequence	Accession ID
Bos taurus cattle	721	XM_005212825.4
Odocoileus virginianus texanus	716	XM_020891631.1
Bison bison bison	721	XM_010863278.1
Bos indicus x Bos taurus hybrid cattle	721	XM_027555592.1
Bos mutus wild yak	717	XM_005889728.2
Bos indicus zebu cattle	710	XM_019969488.1
Bubalus bubalis water buffalo	721	XM_006049386.2
Oryx dammah scimitar-horned oryx	810	XM_040224006.1
Capra hircus goat	722	XM_013967738.2
Ovis aries sheep	722	XM_027966713.2
Sus scrofa pig	720	XM_003354802.4
Vicugna pacos alpaca	723	XM_015237028.2
Camelus ferus Wild Bactrian camel	723	XM_014564859.2
Camelus bactrianus Bactrian camel	552	XM_010951902.1
Camelus dromedarius Arabian camel	722	XM_010989773.2
Neophocaena asiaeorientalis asiaeorientalis Yangtze finless porpoise	713	XM_024753025.1
Balaenoptera acutorostrata scammoni	717	XM_007189708.1
Lipotes vexillifer Yangtze River dolphin	713	XM_007464134.1
Lagenorhynchus obliquidens Pacific white-sided dolphin	717	XM_027131791.1
Globicephala melas long-finned pilot whale	717	XM_030877335.1
Orcinus orca killer whale	717	XM_004280649.2
Tursiops truncatus common bottlenose dolphin	717	XM_019943077.2
Phocoena sinus vaquita	713	XM_032653378.1
Monodon monoceros narwhal	717	XM_029232453.1
Delphinapterus leucas beluga whale	717	XM_022597296.2
Physeter catodon sperm whale	727	XM_024133601.2
Balaenoptera musculus Blue whale	**727**	XM_036873937.1

1211
1212

1213
1214 Table 8-3d. List of primates sequences analyzed

Organism	Length of amino acid sequence	Accession ID
Homo sapiens human	716	NM_001201543.2
Pan troglodytes chimpanzee	716	XM_515502.6
Macaca mulatta Rhesus monkey	716	XM_028831643.1
Macaca fascicularis crab-eating macaque	716	XM_005575777.2
Callithrix jacchus white-tufted-ear marmoset	715	XM_003734729.4
Colobus angolensis palliatus	562	XM_011941831.1
Chlorocebus sabaeus green monkey	716	XM_007970494.2
Cercocebus atys sooty mangabey	714	XM_012039548.1
Macaca nemestrina pig-tailed macaque	716	XM_011713355.2
Papio anubis olive baboon	716	XM_003908708.5
Theropithecus gelada gelada	716	XM_025354341.1
Mandrillus leucophaeus drill	716	XM_011987312.1
Trachypithecus francoisi Francoiss langur	711	XM_033239161.1
Rhinopithecus bieti black snub-nosed monkey	711	XM_017889712.1
Rhinopithecus roxellana golden snub-nosed monkey	711	XM_010384442.2
Piliocolobus tephrosceles Ugandan red Colobus	711	XM_023228337.1
Gorilla gorilla western gorilla	716	XM_004029293.3
Pan paniscus pygmy chimpanzee	716	XM_003830874.3
Pongo abelii Sumatran orangutan	716	NM_001374141.1
Nomascus leucogenys northern white-cheeked gibbon	716	XM_003262434.4
Hylobates moloch silvery gibbon	716	XM_032177370.1
Saimiri boliviensis Bolivian squirrel monkey	715	XM_039464018.1
Sapajus apella tufted capuchin	715	XM_032292015.1
Cebus imitator Panamanian white-faced capuchin	715	XM_017522196.2
Aotus nancymaae Mas night monkey	715	XM_012477168.2
Carlito syrichta Philippine tarsier	715	XM_008054794.2
Propithecus coquereli Coquerels sifaka	714	XM_012639195.1
Microcebus murinus gray mouse lemur	708	XM_012764864.2
Otolemur garnettii small-eared galago	712	XM_003787945.1

1215

1216 ## References

1217 Adebayo, A.O., A.K. Akinloye, A.O. Ihunwo, V.O. Taiwo, and B.O. Oke. 2019. Ultrastructural Studies of
1218 Acrosomal Formation in the Testis of Male Greater Cane Rat (Thryonomys swinderianus). *J Microsc*
1219 *Ultrastruct*. 7:14-18.

1220 Alves-Cruzeiro, J.M., R. Nogales-Cadenas, and A.D. Pascual-Montano. 2014. CentrosomeDB: a new
1221 generation of the centrosomal proteins database for Human and Drosophila melanogaster. *Nucleic*
1222 *Acids Res*. 42:D430-436.

1223 Amaral, A., J. Castillo, J.M. Estanyol, J.L. Ballesca, J. Ramalho-Santos, and R. Oliva. 2013. Human sperm
1224 tail proteome suggests new endogenous metabolic pathways. *Mol Cell Proteomics*. 12:330-342.

1225 Amargant, F., A. Pujol, A. Ferrer-Vaquer, M. Durban, M. Martinez, R. Vassena, and I. Vernos. 2021. The
1226 human sperm basal body is a complex centrosome important for embryo preimplantation
1227 development. *Mol Hum Reprod*. 27.

1228 Arroyo, M.A.M., F.F.S. Silva, P.R.S. Santos, A.R. Silva, M.F. Oliveira, and A.C.A. Neto. 2017. Ultrastructure
1229 of spermatogenesis and spermatozoa in agoutis during sexual development. *Reprod Fertil Dev*.
1230 29:383-393.

1231 Avidor-Reiss, T. 2018. Rapid Evolution of Sperm Produces Diverse Centriole Structures that Reveal the
1232 Most Rudimentary Structure Needed for Function. *Cells*. 7:67.

1233 Avidor-Reiss, T., L. Achinger, and R. Uzbekov. 2022. The Centriole's Role in Miscarriages. *Front Cell Dev*
1234 *Biol*. 10:864692.

1235 Avidor-Reiss, T., and E.L. Fishman. 2019. It takes two (centrioles) to tango. *Reproduction*. 157:R33-R51.

1236 Avidor-Reiss, T., A. Ha, and M.L. Basiri. 2017. Transition Zone Migration: A Mechanism for Cytoplasmic
1237 Ciliogenesis and Postaxonemal Centriole Elongation. *Cold Spring Harbor perspectives in biology*. 9.

1238 Azimzadeh, J. 2021. Evolution of the centrosome, from the periphery to the center. *Curr Opin Struct Biol*.
1239 66:96-103.

1240 Azimzadeh, J., P. Hergert, A. Delouvee, U. Euteneuer, E. Formstecher, A. Khodjakov, and M. Bornens.
1241 2009. hPOC5 is a centrin-binding protein required for assembly of full-length centrioles. *The Journal*
1242 *of cell biology*. 185:101-114.

1243 Baker, M.A., N. Naumovski, L. Hetherington, A. Weinberg, T. Velkov, and R.J. Aitken. 2013. Head and
1244 flagella subcompartmental proteomic analysis of human spermatozoa. *Proteomics*. 13:61-74.

1245 Baker, M.A., G. Reeves, L. Hetherington, J. Muller, I. Baur, and R.J. Aitken. 2007. Identification of gene
1246 products present in Triton X-100 soluble and insoluble fractions of human spermatozoa lysates using
1247 LC-MS/MS analysis. *Proteomics Clin Appl*. 1:524-532.

1248 Bandah-Rozenfeld, D., L. Mizrahi-Meissonnier, C. Farhy, A. Obolensky, I. Chowers, J. Pe'er, S. Merin, T.
1249 Ben-Yosef, R. Ashery-Padan, E. Banin, and D. Sharon. 2010. Homozygosity Mapping Reveals Null
1250 Mutations in FAM161A as a Cause of Autosomal-Recessive Retinitis Pigmentosa. *American Journal*
1251 *of Human Genetics*. 87:382-391.

1252 Bangs, F.K., N. Schrode, A.K. Hadjantonakis, and K.V. Anderson. 2015. Lineage specificity of primary cilia
1253 in the mouse embryo. *Nature cell biology*. 17:113-122.

1254 Bazzi, H., and K.V. Anderson. 2014. Centrioles in the mouse: cilia and beyond. *Cell Cycle*. 13:2809.

1255 Birkhead, T., A. Møller, and W. Sutherland. 1993. Why do females make it so difficult for males to fertilize
1256 their eggs? *Journal of Theoretical Biology*. 161:51-60.

1257 Birkhead, T.R., and F.M. Hunter. 1990. Mechanisms of sperm competition. *Trends Ecol Evol*. 5:48-52.

1258 Breed, W.G., C.M. Leigh, K.P. Aplin, A.A. Shahin, and N.L. Avenant. 2014. Morphological diversity and
1259 evolution of the spermatozoon in the mouse-related clade of rodents. *J Morphol*. 275:540-547.

1260 Breslow, D.K., and A.J. Holland. 2019. Mechanism and Regulation of Centriole and Cilium Biogenesis. *Annu*
1261 *Rev Biochem*. 88:691-724.

1262 Calarco, P.G. 2000. Centrosome precursors in the acentriolar mouse oocyte. *Microsc Res Tech*. 49:428-
1263 434.

1264 Cavazza, T., Y. Takeda, A.Z. Politi, M. Aushev, P. Aldag, C. Baker, M. Choudhary, J. Bucevicius, G.
1265 Lukinavicius, K. Elder, M. Blayney, A. Lucas-Hahn, H. Niemann, M. Herbert, and M. Schuh. 2021.
1266 Parental genome unification is highly error-prone in mammalian embryos. *Cell*. 184:2860-2877
1267 e2822.

1268 Chakraborty, J. 1979. Neck region of gerbil spermatozoa. *Gamete Research*. 2:25-34.

1269 Clark, N.L., J.E. Aagaard, and W.J. Swanson. 2006. Evolution of reproductive proteins from animals and
1270 plants. *Reproduction*. 131:11-22.

1271 Clift, D., and M. Schuh. 2015. A three-step MTOC fragmentation mechanism facilitates bipolar spindle
1272 assembly in mouse oocytes. *Nat Commun*. 6:7217.

1273 Coelho, P.A., L. Bury, B. Sharif, M.G. Riparbelli, J. Fu, G. Callaini, D.M. Glover, and M. Zernicka-Goetz.
1274 2013. Spindle formation in the mouse embryo requires Plk4 in the absence of centrioles. *Dev Cell*.
1275 27:586-597.

1276 Courtois, A., M. Schuh, J. Ellenberg, and T. Hiiragi. 2012. The transition from meiotic to mitotic spindle
1277 assembly is gradual during early mammalian development. *The Journal of cell biology*. 198:357-370.

1278 David, A., F. Liu, A. Tibelius, J. Vulprecht, D. Wald, U. Rothermel, R. Ohana, A. Seitel, J. Metzger, R. Ashery-
1279 Padan, H.P. Meinzer, H.J. Grone, S. Izraeli, and A. Kramer. 2014. Lack of centrioles and primary
1280 cilia in STIL(-/-) mouse embryos. *Cell Cycle*. 13:2859-2868.

1281 Downs, L.M., and C.S. Mellersh. 2014. An Intronic SINE insertion in FAM161A that causes exon-skipping is
1282 associated with progressive retinal atrophy in Tibetan Spaniels and Tibetan Terriers. *PLoS One*.
1283 9:e93990.

1284 Edgar, R.C. 2004. MUSCLE: multiple sequence alignment with high accuracy and high throughput. *Nucleic*
1285 *Acids Res*. 32:1792-1797.

1286 Fawcett, D.W. 1975. The mammalian spermatozoon. *Dev Biol*. 44:394-436.

1287 Ferreira, A., and H. Dolder. 2003. Sperm ultrastructure and spermatogenesis in the lizard, Tropidurus
1288 itambere. *Biocell*. 27:353-362.

1289 Finseth, F.R., Y. Dong, A. Saunders, and L. Fishman. 2015. Duplication and Adaptive Evolution of a Key
1290 Centromeric Protein in Mimulus, a Genus with Female Meiotic Drive. *Mol Biol Evol*. 32:2694-2706.

1291 Fisher, H.S., E. Jacobs-Palmer, J.M. Lassance, and H.E. Hoekstra. 2016. The genetic basis and fitness
1292 consequences of sperm midpiece size in deer mice. *Nat Commun*. 7:13652.

1293 Fishman, E.L., K. Jo, A. Ha, R. Royfman, A. Zinn, M. Krishnamurthy, and T. Avidor-Reiss. 2017. Atypical
1294 centrioles are present in Tribolium sperm. *Open biology*. 7:160334.

1295 Fishman, E.L., K. Jo, Q.P.H. Nguyen, D. Kong, R. Royfman, A.R. Cekic, S. Khanal, A.L. Miller, C. Simerly,
1296 G. Schatten, J. Loncarek, V. Mennella, and T. Avidor-Reiss. 2018. A novel atypical sperm centriole
1297 is functional during human fertilization. *Nat Commun*. 9:2210.

1298 Fishman, E.L., K. Turner, A. Jaiswal, S. Khanal, B. Ott, P. Dusza, and T. Avidor-Reiss. 2021. The Typical
1299 and Atypical Centrioles and Their Potential Roles in the Sperm and Embryo. Springer International
1300 Publishing, Cham. 85-120.

1301 Franklin, L.E., C. Barros, and E.N. Fussell. 1970. The acrosomal region and the acrosome reaction in sperm
1302 of the golden hamster. *Biology of reproduction*. 3:180-200.

1303 Garanina, A.S., I.B. Alieva, E.E. Bragina, E. Blanchard, B. Arbeille, F. Guerif, S. Uzbekova, and R.E.
1304 Uzbekov. 2019. The Centriolar Adjunct(-)Appearance and Disassembly in Spermiogenesis and the
1305 Potential Impact on Fertility. *Cells*. 8:180.

1306 Garcia Lorenzana, M., R. Lopez Wilchis, and G. Vazquez Nin. 1998. Basic aspects of the fine structure of
1307 Peromyscus winkelmamzi spermatozoa (Rodentia: Cricetidae). *Biblioteca*. 4.

1308 Gomendio, M., and E.R. Roldan. 1991. Sperm competition influences sperm size in mammals. *Proc Biol*
1309 *Sci*. 243:181-185.

1310 Gozashti, L., R. Corbett-Detig, and S.W. Roy. 2021. Evolutionary rates of testes-expressed genes differ
1311 between monogamous and promiscuous Peromyscus species. *bioRxiv*:2021.2004.2021.440792.

1312 Green, C.D., Q. Ma, G.L. Manske, A.N. Shami, X. Zheng, S. Marini, L. Moritz, C. Sultan, S.J. Gurczynski,
1313 B.B. Moore, M.D. Tallquist, J.Z. Li, and S.S. Hammoud. 2018. A Comprehensive Roadmap of Murine
1314 Spermatogenesis Defined by Single-Cell RNA-Seq. *Dev Cell*. 46:651-667 e610.

1315 Greenan, G.A., B. Keszthelyi, R.D. Vale, and D.A. Agard. 2018. Insights into centriole geometry revealed
1316 by cryotomography of doublet and triplet centrioles. *eLife*. 7:e36851.

1317 Gueth-Hallonet, C., C. Antony, J. Aghion, A. Santa-Maria, I. Lajoie-Mazenc, M. Wright, and B. Maro. 1993.
1318 gamma-Tubulin is present in acentriolar MTOCs during early mouse development. *Journal of cell*
1319 *science*. 105 (Pt 1):157-166.

1320 Hamasaki, M., M. Wakimoto, T. Maehara, and H. Matsuo. 1994. Three-dimensional structures of the neck
1321 region of the hamster spermatozoa in the caudal epididymis. *Arch Histol Cytol*. 57:59-65.

1322 Hao, S.L., and Y.P. Zhang. 2018. Ultrastructure of the spermatozoon of the Chinese water snake, Myrrophis
1323 (Enhydris) chinensis (Reptilia: Homalopsidae). *European Zoological Journal*. 85:349-361.

1324 Healey, P., and B.J. Weir. 1970. Changes in the ultrastructure of chinchilla spermatozoa in different diluents.
1325 *J Reprod Fertil*. 21:191-193.

1326 Henikoff, S., K. Ahmad, and H.S. Malik. 2001. The centromere paradox: stable inheritance with rapidly
1327 evolving DNA. *Science*. 293:1098-1102.

1328 Henikoff, S., J. Thakur, S. Kasinathan, and P.B. Talbert. 2017. Remarkable evolutionary plasticity of
1329 centromeric chromatin. *In* Cold Spring Harbor symposia on quantitative biology. Vol. 82. Cold Spring
1330 Harbor Laboratory Press. 71-82.

1331 Hess, R.A., R.J. Thurston, and D.H. Gist. 1991. Ultrastructure of the turtle spermatozoon. *Anat Rec*.
1332 229:473-481.

1333 Hook, K.A., L.M. Wilke, and H.S. Fisher. 2021. Apical Sperm Hook Morphology Is Linked to Sperm
1334 Swimming Performance and Sperm Aggregation in Peromyscus Mice. *Cells*. 10:2279.

1335 Howe, K., and G. FitzHarris. 2013. A non-canonical mode of microtubule organization operates throughout
1336 pre-implantation development in mouse. *Cell Cycle*. 12:1616-1624.

1337 Hruban, Z., J. Martan, and I. Aschenbrenner. 1971. Polarized cylindrical body in the epididymis of the flying
1338 squirrel. *Journal of Morphology*. 135:87-97.

1339 Humphries, S., J.P. Evans, and L.W. Simmons. 2008. Sperm competition: linking form to function. *BMC*
1340 *Evol Biol*. 8:319.

1341 Jamieson, B.G. 1991. Fish evolution and systematics: evidence from spermatozoa: with a survey of
1342 lophophorate, echinoderm and protochordate sperm and an account of gamete cryopreservation.
1343 Cambridge University Press.

1344 Jamieson, B.G.M. 2007. Avian spermatozoa: Structure and phylogeny. *In* Reproductive Biology and
1345 Phylogeny of Birds: Part A. Vol. 6A. B.G.M. Jamieson, editor. Science Publishers, Inc. 349-561.

1346 Jin, Y.X., X.S. Cui, X.F. Yu, S.H. Lee, Q.L. Wang, W.W. Gao, Y.N. Xu, S.C. Sun, I.K. Kong, and N.H. Kim.
1347 2012. Cat fertilization by mouse sperm injection. *Zygote*. 20:371-378.

1348 Joly, D., A. Korol, and E. Nevo. 2004. Sperm size evolution in Drosophila: inter- and intraspecific analysis.
1349 *Genetica*. 120:233-244.

1350 Junker, A.D., L.G. Woodhams, A.W.J. Soh, E.T. O'Toole, P.V. Bayly, and C.G. Pearson. 2022. Basal bodies
1351 bend in response to ciliary forces. *Mol Biol Cell*. 33:ar146.

1352 Kahrl, A.F., R.R. Snook, and J.L. Fitzpatrick. 2021. Fertilization mode drives sperm length evolution across
1353 the animal tree of life. *Nat Ecol Evol*. 5:1153-1164.

1354 Kai, Y., H. Kawano, and N. Yamashita. 2021. First mitotic spindle formation is led by sperm centrosome-
1355 dependent MTOCs in humans. *Reproduction*. 161:V19-V22.

1356 Kalyaanamoorthy, S., B.Q. Minh, T.K.F. Wong, A. von Haeseler, and L.S. Jermiin. 2017. ModelFinder: fast
1357 model selection for accurate phylogenetic estimates. *Nature methods*. 14:587-589.

1358 Khanal, S., M.R. Leung, A. Royfman, E.L. Fishman, B. Saltzman, H. Bloomfield-Gadelha, T. Zeev-Ben-
1359 Mordehai, and T. Avidor-Reiss. 2021. A dynamic basal complex modulates mammalian sperm
1360 movement. *Nat Commun*. 12:3808.

1361 Khire, A., K.H. Jo, D. Kong, T. Akhshi, S. Blachon, A.R. Cekic, S. Hynek, A. Ha, J. Loncarek, V. Mennella,
1362 and T. Avidor-Reiss. 2016. Centriole Remodeling during Spermiogenesis in Drosophila. *Curr Biol*.
1363 26:3183-3189.

1364 Kosakovsky Pond, S.L., and S.D. Frost. 2005. Not so different after all: a comparison of methods for
1365 detecting amino acid sites under selection. *Molecular biology and evolution*. 22:1208-1222.

1366 Kuretake, S., Y. Kimura, K. Hoshi, and R. Yanagimachi. 1996. Fertilization and development of mouse
1367 oocytes injected with isolated sperm heads. *Biology of reproduction*. 55:789-795.

1368 Langmann, T., S.A. Di Gioia, I. Rau, H. Stohr, N.S. Maksimovic, J.C. Corbo, A.B. Renner, E. Zrenner, G.
1369 Kumaramanickavel, M. Karlstetter, Y. Arsenijevic, B.H. Weber, A. Gal, and C. Rivolta. 2010.
1370 Nonsense mutations in FAM161A cause RP28-associated recessive retinitis pigmentosa. *Am J Hum*
1371 *Genet*. 87:376-381.

1372 Le Guennec, M., N. Klena, D. Gambarotto, M.H. Laporte, A.M. Tassin, H. van den Hoek, P.S. Erdmann, M.
1373 Schaffer, L. Kovacik, S. Borgers, K.N. Goldie, H. Stahlberg, M. Bornens, J. Azimzadeh, B.D. Engel,
1374 V. Hamel, and P. Guichard. 2020. A helical inner scaffold provides a structural basis for centriole
1375 cohesion. *Sci Adv*. 6:eaaz4137.

1376 Lee, J.-H., and T. Mori. 2006. Ultrastructural observations on the sperm of two Apodemus species,
1377 Apodemus agrarius coreae and Apodemus speciosus peninsulae, in Korea.

1378 Lee, J.-H., and K.-R. Park. 2011. Fine Structure of Sperm in the Korea Squirrel, Tamias sibiricus. *Applied*
1379 *Microscopy*. 41:99-107.

1380 Lemaitre, J.F., J.M. Gaillard, and S.A. Ramm. 2020. The hidden ageing costs of sperm competition. *Ecol*
1381 *Lett*. 23:1573-1588.

1382 Leung, M.R., M.C. Roelofs, R.T. Ravi, P. Maitan, H. Henning, M. Zhang, E.G. Bromfield, S.C. Howes, B.M.
1383 Gadella, H. Bloomfield-Gadelha, and T. Zeev-Ben-Mordehai. 2021. The multi-scale architecture of
1384 mammalian sperm flagella and implications for ciliary motility. *EMBO J*. 40:e107410.

1385 Li, Y.Z., N. Li, W.S. Liu, Y.W. Sha, R.F. Wu, Y.L. Tang, X.S. Zhu, X.L. Wei, X.Y. Zhang, Y.F. Wang, Z.X. Lu,
1386 and F.X. Zhang. 2022. Biallelic mutations in spermatogenesis and centriole-associated 1 like
1387 (SPATC1L) cause acephalic spermatozoa syndrome and male infertility. *Asian journal of andrology*.
1388 24:67-72.

1389 Luke, L., M. Tourmente, and E.R. Roldan. 2016. Sexual Selection of Protamine 1 in Mammals. *Mol Biol*
1390 *Evol*. 33:174-184.

1391 Lüpold, S., R.A. de Boer, J.P. Evans, J.L. Tomkins, and J.L. Fitzpatrick. 2020. How sperm competition
1392 shapes the evolution of testes and sperm: a meta-analysis. *Philosophical Transactions of the Royal*
1393 *Society B*. 375:20200064.

1394 Lüpold, S., and S. Pitnick. 2018. Sperm form and function: what do we know about the role of sexual
1395 selection? *Reproduction*. 155:R229-R243.

1396 Manandhar, G., H. Schatten, and P. Sutovsky. 2005. Centrosome reduction during gametogenesis and its
1397 significance. *Biology of reproduction*. 72:2-13.

1398 Manandhar, G., C. Simerly, J.L. Salisbury, and G. Schatten. 1999. Centriole and centrin degeneration during
1399 mouse spermiogenesis. *Cell Motil Cytoskeleton*. 43:137-144.

1400 Manandhar, G., C. Simerly, and G. Schatten. 2000. Highly degenerated distal centrioles in rhesus and
1401 human spermatozoa. *Hum Reprod*. 15:256-263.

1402 Manandhar, G., P. Sutovsky, H.C. Joshi, T. Stearns, and G. Schatten. 1998. Centrosome reduction during
1403 mouse spermiogenesis. *Dev Biol*. 203:424-434.

1404 Mokos, J., I. Scheuring, A. Liker, R.P. Freckleton, and T. Székely. 2021. Degree of anisogamy is unrelated
1405 to the intensity of sexual selection. *Scientific reports*. 11:1-11.

1406 Murrell, B., J.O. Wertheim, S. Moola, T. Weighill, K. Scheffler, and S.L. Kosakovsky Pond. 2012. Detecting
1407 individual sites subject to episodic diversifying selection. *PLoS Genet*. 8:e1002764.

1408 Palacios Martinez, S., J. Greaney, and J. Zenker. 2022. Beyond the centrosome: The mystery of microtubule
1409 organising centres across mammalian preimplantation embryos. *Curr Opin Cell Biol*. 77:102114.

1410 Parker, G.A. 1970. Sperm Competition and Its Evolutionary Consequences in the Insects. *Biological*
1411 *Reviews*. 45:525-567.

1412 Parker, G.A. 2014. The sexual cascade and the rise of pre-ejaculatory (Darwinian) sexual selection, sex
1413 roles, and sexual conflict. *Cold Spring Harbor perspectives in biology*. 6:a017509.

1414 Plant, T.M., and A.J. Zeleznik. 2014. Knobil and Neill's physiology of reproduction. Academic Press.

1415 Pomp, O., H.Y.G. Lim, R.M. Skory, A.A. Moverley, P. Tetlak, S. Bissiere, and N. Plachta. 2022. A monoastral
1416 mitotic spindle determines lineage fate and position in the mouse embryo. *Nature cell biology*.
1417 24:155-167.

1418 Rambaut, A. University of Edinburgh, Institute of Evolutionary Biology; Edinburgh, UK: 2012. FigTree V. 1.4.
1419 Molecular Evolution, Phylogenetics and Epidemiology.

1420 Roldan, E.R., M. Gomendio, and A.D. Vitullo. 1992. The evolution of eutherian spermatozoa and underlying
1421 selective forces: female selection and sperm competition. *Biol Rev Camb Philos Soc*. 67:551-593.

1422 Roldan, E.R.S. 2019. Sperm competition and the evolution of sperm form and function in mammals. *Reprod*
1423 *Domest Anim*. 54 Suppl 4:14-21.

1424 Ronquist, F., M. Teslenko, P. van der Mark, D.L. Ayres, A. Darling, S. Hohna, B. Larget, L. Liu, M.A. Suchard,
1425 and J.P. Huelsenbeck. 2012. MrBayes 3.2: efficient Bayesian phylogenetic inference and model
1426 choice across a large model space. *Syst Biol*. 61:539-542.

1427 Roosing, S., I.J. Lamers, E. de Vrieze, L.I. van den Born, S. Lambertus, H.H. Arts, P.B.S. Group, T.A. Peters,
1428 C.B. Hoyng, H. Kremer, L. Hetterschijt, S.J. Letteboer, E. van Wijk, R. Roepman, A.I. den Hollander,
1429 and F.P. Cremers. 2014. Disruption of the basal body protein POC1B results in autosomal-recessive
1430 cone-rod dystrophy. *Am J Hum Genet*. 95:131-142.

1431 Ross, B.D., L. Rosin, A.W. Thomae, M.A. Hiatt, D. Vermaak, A.F. de la Cruz, A. Imhof, B.G. Mellone, and
1432 H.S. Malik. 2013. Stepwise evolution of essential centromere function in a Drosophila neogene.
1433 *Science*. 340:1211-1214.

1434 Rowley, A.G., T.S. Daly-Engel, and J.L. Fitzpatrick. 2019. Testes size increases with sperm competition risk
1435 and intensity in bony fish and sharks. *Behavioral Ecology*. 30:364-371.

1436 Schatten, G., C. Simerly, and H. Schatten. 1985. Microtubule configurations during fertilization, mitosis, and
1437 early development in the mouse and the requirement for egg microtubule-mediated motility during
1438 mammalian fertilization. *Proc Natl Acad Sci U S A*. 82:4152-4156.

1439 Schatten, H., G. Schatten, D. Mazia, R. Balczon, and C. Simerly. 1986. Behavior of centrosomes during
1440 fertilization and cell division in mouse oocytes and in sea urchin eggs. *Proc Natl Acad Sci U S A*.
1441 83:105-109.

1442 Schill, D.J., G.W. LaBar, E.R.J.M. Mamer, and K.A. Meyer. 2010. Sex Ratio, Fecundity, and Models
1443 Predicting Length at Sexual Maturity of Redband Trout in Idaho Desert Streams. *North American*
1444 *Journal of Fisheries Management*. 30:1352-1363.

1445 Shin, T.-Y., Y. Noguchi, Y. Yamamoto, K. MOCHIDA, and A. OGURA. 1998. Microtubule organization in
1446 hamster oocytes after fertilization with mature spermatozoa and round spermatids. *Journal of*
1447 *Reproduction and Development*. 44:185-189.

1448 Simerly, C.R., N.B. Hecht, E. Goldberg, and G. Schatten. 1993. Tracing the incorporation of the sperm tail
1449 in the mouse zygote and early embryo using an anti-testicular alpha-tubulin antibody. *Dev Biol*.
1450 158:536-548.

1451 Steib, E., M.H. Laporte, D. Gambarotto, N. Olieric, C. Zheng, S. Borgers, V. Olieric, M. Le Guennec, F. Koll,
1452 A.M. Tassin, M.O. Steinmetz, P. Guichard, and V. Hamel. 2020. WDR90 is a centriolar microtubule
1453 wall protein important for centriole architecture integrity. *eLife*. 9:e57205.

1454 Steppan, S., R. Adkins, and J. Anderson. 2004. Phylogeny and divergence-date estimates of rapid radiations
1455 in muroid rodents based on multiple nuclear genes. *Syst Biol*. 53:533-553.

1456 Steppan, S.J., and J.J. Schenk. 2017. Muroid rodent phylogenetics: 900-species tree reveals increasing
1457 diversification rates. *PLoS One*. 12:e0183070.

1458 Sutovsky, P., and G. Schatten. 2000. Paternal contributions to the mammalian zygote: fertilization after
1459 sperm-egg fusion. *Int Rev Cytol*. 195:1-65.

1460 Swanson, W.J., and V.D. Vacquier. 2002. The rapid evolution of reproductive proteins. *Nature reviews.*
1461 *Genetics*. 3:137-144.

1462 Tapia Contreras, C., and S. Hoyer-Fender. 2021. The Transformation of the Centrosome into the Basal
1463 Body: Similarities and Dissimilarities between Somatic and Male Germ Cells and Their Relevance
1464 for Male Fertility. *Cells*. 10.

1465 Temple-Smith, P., A. Ravichandran, and F. Horta. 2018. Sperm: comparative vertebrate. *Encyclopedia of*
1466 *Reproduction*. 2:210-220.

1467 Thybert, D., M. Roller, F.C.P. Navarro, I. Fiddes, I. Streeter, C. Feig, D. Martin-Galvez, M. Kolmogorov, V.
1468 Janousek, W. Akanni, B. Aken, S. Aldridge, V. Chakrapani, W. Chow, L. Clarke, C. Cummins, A.
1469 Doran, M. Dunn, L. Goodstadt, K. Howe, M. Howell, A.A. Josselin, R.C. Karn, C.M. Laukaitis, L.
1470 Jingtao, F. Martin, M. Muffato, S. Nachtweide, M.A. Quail, C. Sisu, M. Stanke, K. Stefflova, C. Van
1471 Oosterhout, F. Veyrunes, B. Ward, F. Yang, G. Yazdanifar, A. Zadissa, D.J. Adams, A. Brazma, M.
1472 Gerstein, B. Paten, S. Pham, T.M. Keane, D.T. Odom, and P. Flicek. 2018. Repeat associated
1473 mechanisms of genome evolution and function revealed by the Mus caroli and Mus pahari genomes.
1474 *Genome Res*. 28:448-459.

1475 Toll-Riera, M., S. Laurie, and M.M. Alba. 2011. Lineage-specific variation in intensity of natural selection in
1476 mammals. *Mol Biol Evol*. 28:383-398.

1477 Tung, C.K., and S.S. Suarez. 2021. Co-Adaptation of Physical Attributes of the Mammalian Female
1478 Reproductive Tract and Sperm to Facilitate Fertilization. *Cells*. 10:1297.

1479 Turner, K., N. Solanki, H.O. Salouha, and T. Avidor-Reiss. 2022. Atypical Centriolar Composition Correlates
1480 with Internal Fertilization in Fish. *Cells*. 11:758.

1481 Uzbekov, R., G. Singina, E. Shedova, C. Banliat, T. Avidor-Reiss, and S. Uzbekova. 2023. Centrosome
1482 formation in the bovine early embryo. *bioRxiv*:2022.2011.2029.517493.

1483 Van Der Horst, G., L. Maree, S.H. Kotze, and M.J. O'Riain. 2011. Sperm structure and motility in the eusocial
1484 naked mole-rat, Heterocephalus glaber: a case of degenerative orthogenesis in the absence of
1485 sperm competition? *BMC Evol Biol*. 11:351.

1486 Varea Sanchez, M., M. Bastir, and E.R. Roldan. 2013. Geometric morphometrics of rodent sperm head
1487 shape. *PLoS One*. 8:e80607.

1488 Wang, G., Y. Guo, T. Zhou, X. Shi, J. Yu, Y. Yang, Y. Wu, J. Wang, M. Liu, X. Chen, W. Tu, Y. Zeng, M.
1489 Jiang, S. Li, P. Zhang, Q. Zhou, B. Zheng, C. Yu, Z. Zhou, X. Guo, and J. Sha. 2013. In-depth
1490 proteomic analysis of the human sperm reveals complex protein compositions. *Journal of*
1491 *proteomics*. 79:114-122.

1492 Winey, M., and E. O'Toole. 2014. Centriole structure. *Philosophical transactions of the Royal Society of*
1493 *London. Series B, Biological sciences*. 369:20130457.

1494 Woolley, D.M., D.A. Carter, and G.N. Tilly. 2008. Compliance in the neck structures of the guinea pig
1495 spermatozoon, as indicated by rapid freezing and electron microscopy. *J Anat*. 213:336-341.

1496 Woolley, D.M., and D.W. Fawcett. 1973. The degeneration and disappearance of the centrioles during the
1497 development of the rat spermatozoon. *Anat Rec*. 177:289-301.

1498 Wu, B., H. Gao, C. Liu, and W. Li. 2020. The coupling apparatus of the sperm head and taildagger. *Biology*
1499 *of reproduction*. 102:988-998.

1500 Xu, B., Z. Hao, K.N. Jha, Z. Zhang, C. Urekar, L. Digilio, S. Pulido, J.F. Strauss, 3rd, C.J. Flickinger, and
1501 J.C. Herr. 2008. TSKS concentrates in spermatid centrioles during flagellogenesis. *Dev Biol*.
1502 319:201-210.

1503 Yabe, T., X. Ge, and F. Pelegri. 2007. The zebrafish maternal-effect gene cellular atoll encodes the centriolar
1504 component sas-6 and defects in its paternal function promote whole genome duplication. *Dev Biol*.
1505 312:44-60.

1506 Yamauchi, Y., R. Yanagimachi, and T. Horiuchi. 2002. Full-term development of golden hamster oocytes
1507 following intracytoplasmic sperm head injection. *Biology of reproduction*. 67:534-539.

1508 Yan, W., K. Morozumi, J. Zhang, S. Ro, C. Park, and R. Yanagimachi. 2008. Birth of mice after
1509 intracytoplasmic injection of single purified sperm nuclei and detection of messenger RNAs and
1510 MicroRNAs in the sperm nuclei. *Biology of reproduction*. 78:896-902.

1511 Yanagimachi, R., Y. Kamiguchi, S. Sugawara, and K. Mikamo. 1983. Gametes and fertilization in the
1512 Chinese hamster. *Gamete research*. 8:97-117.

1513 Yang, Z. 2007. PAML 4: phylogenetic analysis by maximum likelihood. *Mol Biol Evol*. 24:1586-1591.

1514 Zach, F., F. Grassmann, T. Langmann, N. Sorusch, U. Wolfrum, and H. Stohr. 2012. The retinitis pigmentosa
1515 28 protein FAM161A is a novel ciliary protein involved in intermolecular protein interaction and
1516 microtubule association. *Hum Mol Genet*. 21:4573-4586.

1517 Zach, F., and H. Stohr. 2014. FAM161A, a novel centrosomal-ciliary protein implicated in autosomal
1518 recessive retinitis pigmentosa. *Adv Exp Med Biol*. 801:185-190.

1519 Zamboni, L., and M. Stefanini. 1971. The fine structure of the neck of mammalian spermatozoa. *Anat Rec*.
1520 169:155-172.

1521 Zenker, J., M.D. White, R.M. Templin, R.G. Parton, O. Thorn-Seshold, S. Bissiere, and N. Plachta. 2017. A
1522 microtubule-organizing center directing intracellular transport in the early mouse embryo. *Science*.
1523 357:925-928.

1524